Development of an Unsteady Aeroelastic Solver for the Analysis of Modern Turbomachinery Designs

Timothy James Leger
Wright State University

Development of an Unsteady Aeroelastic Solver for the Analysis of Modern Turbomachinery Designs

A dissertation submitted in partial fulfillment of the

requirements for the degree of

Doctor of Philosophy

By

Timothy James Leger

M.S. Wright State University, 2000

2010

Wright State University

WRIGHT STATE UNIVERSITY

SCHOOL OF GRADUATE STUDIES

August 18, 2010

I HEREBY RECOMMEND THAT THE DISSERTATION PREPARED UNDER MY SUPERVISION BY Timothy James Leger ENTITLED Development of an Unsteady Aeroelastic Solver for the Analysis of Modern Turbomachinery Designs BE ACCEPTED IN PARTIAL FULFILLMENT OF THE REQUIREMENTS FOR THE DEGREE OF Doctor of Philosophy.

Mitch Wolff, Ph.D.
Dissertation Director

Ramana V. Grandhi, Ph.D.
Director, Ph.D. in Engineering Program

Andrew T. Hsu, Ph.D.
Dean, Graduate Studies

Committee on
Final Examination

Mitch Wolff, Ph.D.

Scott Thomas, Ph.D.

Joseph Shang, Ph.D.

Gary Lamont, Ph.D.

David A. Johnston, Ph.D.

ABSTRACT

Leger, Timothy James, Ph.D., Department of Mechanical and Material Engineering, Wright State University, 2010. Development of an Unsteady Aeroelastic Solver for the Analysis of Modern Turbomachinery Designs

Developers of aircraft gas turbine engines continually strive for greater efficiency and higher thrust-to-weight ratio designs. To meet these goals, advanced designs generally feature thin, low aspect airfoils, which offer increased performance but are highly susceptible to flow-induced vibrations. As a result, High Cycle Fatigue (HCF) has become a universal problem throughout the gas turbine industry and unsteady aeroelastic computational models are needed to predict and prevent these problems in modern turbomachinery designs. This research presents the development of a 3D unsteady aeroelastic solver for turbomachinery applications. To accomplish this, a well established turbomachinery Computational Fluid Dynamics (CFD) code called Corsair is loosely coupled to the commercial Computational Structural Solver (CSD) Ansys® through the use of a Fluid Structure Interaction (FSI) module.

Significant modifications are made to Corsair to handle the integration of the FSI module and improve overall performance. To properly account for fluid grid deformations dictated by the FSI module, temporal based coordinate transformation metrics are incorporated into Corsair. Wall functions with user specified surface roughness are also added to reduce fluid grid density requirements near solid surfaces. To increase overall performance and ease of future modifications to the source code, Corsair is rewritten in Fortran 90 with an emphasis on reducing memory usage and improving source code readability and structure. As part of this effort, the shared memory data structure of Corsair is replaced with a distributed model. Domain decomposition of individual grids in the radial direction is also incorporated into Corsair for additional parallelization, along with a utility to automate this process in an optimal manner based on user input. This additional parallelization helps offset the inability to use the fine grain mp-threads parallelization in the original code on non-distributed memory architectures such as the PC Beowulf cluster used for this research. Conversion routines and utilities are created to handle differences in grid formats between Corsair and the FSI module.

The resulting aeroelastic solver is tested using two simplified configurations. First, the well understood case of a flexible cylinder in cross flow is studied with the natural frequency of the cylinder set to the shedding frequency of the Von Karman streets. The cylinder is self excited and thus demonstrates the correct exchange of energy between the fluid and structural models. The second test case is based on the fourth standard configuration and demonstrates the ability of the solver to predict the dominant vibrational modes of an aeroelastic turbomachinery blade. For this case, a single blade from the fourth standard configuration is subjected to a step function from zero loading to the converged flow solution loading in order to excite the structural modes of the blade. These modes are then compared to those obtained from an in vacuo Ansys® analysis with good agreement between the two.

Table of Contents

List of Figures

List of Tables

List of Symbols

Symbol	*Description*
A	area
$\tilde{A},\tilde{B},\tilde{C}$	flux jacobians
c	speed of sound
c_p	constant pressure specific heat
c_v	constant volume specific heat
chmp	number of Chimera grid points
C	Courant number
C_f	skin friction coefficient
C_{kleb}	Klebanoff constant
e	energy
E	efficiency, Young's modulus
E,F,G	flux vectors
f	force, frequency (Hz)
flops	floating point operations
F	force
G	serial runtime multiplier
GB	gigabyte
h	enthalpy
i,j,k,n	grid and time indices
in	inch
I	identity matrix, mass moment of inertia
J	Jacobian of coordinate transformation
k	thermal conductivity
k_s	sand roughness height
KB	kilobytes
$\overline{K}$	parallel efficiency constant
l	mixing length
lbf	pounds-force
L	characteristic length
LHS	left hand side
m	mass
MB	megabyte
n	normal vector
N	shape function
NMF	nodal memory footprint
ovlp	grid overlap
P	pressure, number of processors
P^+	nondimensional boundary layer pressure gradient
Pr	Prandtl number
q	heat flux
Q	solution vector
r	radius from hub, surface vector
R	gas constant, Riemann invariant

Re	Reynolds number
RHS	right hand side
s, sec	seconds
S	entropy, control volume surface, speedup
St	Strouhal number
STCF4	fourth standard configuration
t	time
T	temperature
T_O	parallel overhead time
$\mathcal{T}$	eigen vectors
u,v,w	velocities in the x, y, z directions
u^+	normalized boundary layer velocity
U	wheel speed
U,V,W	contravariant velocities
V	volume
W	work
$\widehat{W}$	isoefficiency
x,y,z	spatial coordinates
yz	arc length from at fixed radius
y^+	normalized boundary layer height
α	pitch, Clauser constant
β	compressibility factor, yaw
β_n	weighted natural frequency
γ	ratio of specific heats
ρ	density
ξ,η,ζ	curvilinear coordinate directions
μ	dynamic viscisity
λ	second coefficient of viscosity, eigenvalue
τ	shear stress, curvilinear time coordinate
$\emptyset$	numerical flux coefficients
Θ	order of magnitude
φ	flow variables at shape function
Λ	eigenvalue matrix
ε	error
σ	stress tensor
σ_n	mode shape
κ	Von Karman constant
ω	frequency (rad/s), vorticity
δ	normal distance, displacement
$\hat{\delta}$	admissible virtual displacement
Γ	wetted surface
Ω_S^e	wetted structural element

Subscripts

comm	communication
F	fluid
IM,JM,KM	grid index limits
LD	long diagonal
P	parallel
S	serial, structure
t	total
TH	tetrakis hexahedron
v	viscid
wall	value at the wall
xcalc	calculation of solution
∞	inlet free-stream

Superscripts

‘	pseudo term
+	normalized
~	physical flux
^	numerical flux
—	total
*	non-dimensional term
$\overline{}^{*}$, $\overline{}^{**}$	intermediate ADI solutions
F	fluid
S	structure

ACKNOWLEDGEMENTS

I would like to express my sincere appreciation to my adviser, Dr. Mitch Wolff, for introducing me to the field of turbomachinery and for the encouragement he has given me throughout my graduate studies. I feel fortunate and privileged to have worked with such a dedicated and talented professor. I extend my utmost gratitude and respect to him.

A great deal of thanks also goes to Dr. David Johnston for his insight and help with this research, especially with regards to the Fluid Structure Interaction module. I would also like to gratefully acknowledge Dr. Joseph Shang, Dr. Gary Lamont, and Dr. Scott Thomas for serving on my dissertation committee and providing excellent classroom instruction.

I am fortunate to have interacted with many bright, talented, and motivated individuals at Wright State. Special thanks go to Greg Wilt, Sean Mortara, Jonathan Blair, Dr. Jim Menart, Dr. Ken Cornelius, Dr. George Huang, Dr. Haibo Dong, and all my instructors, you helped me more than you will ever know.

Finally, I would like to thank my parents, Jim and Verna, for their unwavering support through times when it looked like I might never graduate. They have been the greatest influence in my life and I owe all my success to them. Their moral and financial support throughout my life has given me the ability to be where I am today. I dedicate this dissertation to them.

1. INTRODUCTION

Developers of aircraft gas turbine engines continually strive for greater efficiency and higher thrust-to-weight ratio designs. To meet this goal, the trend in gas turbine designs has been to reduce size and weight of engines by decreasing the number of compressor stages, the number of blades per row, and the axial spacing between vane/blade rows [1]. However, these reductions result in significantly increased aerodynamic loading of the blades and unsteady interaction between blade rows. In addition, advanced compressor designs generally feature thin, low aspect airfoils, which offer increased performance but are highly susceptible to flow-induced vibrations [2]. As a result, High Cycle Fatigue (HCF) has become a universal problem throughout the gas turbine industry. In response to these HCF problems, a considerable portion of recent research in compressor and turbine design has involved the investigation of unsteady aeroelastic phenomena, namely flutter and forced response [3].

Flutter is defined as an unstable and self-excited vibration of a body in an airstream and results from a continuous interaction between the aerodynamics and the structural mechanics, both of which tend to be nonlinear in modern turbomachinery designs [4]. In turbomachinery blade rows, the mass ratio (structure to fluid) tends to be high resulting in a single-mode phenomenon. This is because the aerodynamic forces, which remain much smaller than the inertial and stiffness forces, do not usually cause modal coupling. However, this also means that the aeroelastic mode can be significantly different from the structural mode in both frequency and modal shape. Flutter is a particularly difficult problem in turbomachinery since there are many additional features with consequences that are currently not fully understood. These include flow distortions due to up and down stream blade-rows and the loss of spatial periodicity of vibration due to aerodynamic effects and blade-to-blade differences (commonly known as structural and aerodynamic mistuning) [5].

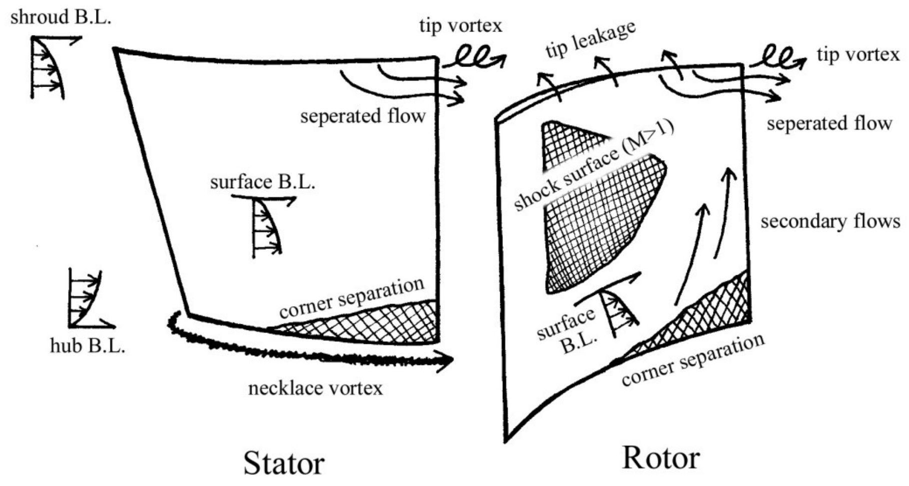

Figure 1-1. Sources of unsteady flow in rotating turbomachinery

When rotating blades pass through flow defects created by the interaction of upstream and downstream blade rows, the ensuing large unsteady aerodynamic forces can cause excessive vibration levels. This interaction between blade rows is known as forced response [4] and becomes a major problem when the excitation frequency coincides with a natural frequency of the blade. Of particular interest to designers is the prediction of vibration amplitude under unsteady aerodynamic loading which can be due to wake passing from upstream blade-rows (wake-rotor interaction), the potential field of upstream and downstream blade rows (potential-rotor interaction), or to fluctuating back pressures [6]. Because of the numerous unknown factors such as structural damping, nonlinear damping in the blade roots, and the forcing itself, forced response analyses usually aim at ranking potential designs rather than predicting actual vibration levels.

Current designers typically address HCF and unsteady aeroelastic phenomena using a Computational Fluid Dynamics (CFD) analysis of a single blade row with the unsteady forcing applied through specified inflow/outflow boundary conditions or the predicted blade motion itself [4]. The resulting blade row unsteady loading is utilized with a Computational Structural Dynamics (CSD) model to determine the unsteady stresses and the predicted blade fatigue life. While these two steps may be iterated upon several times, they are usually performed by different groups with an associated loss in accuracy and efficiency. In addition, the CFD models used are generally inviscid and time-linearized, resulting in a model that is invalid at off design operating conditions where serious unsteady aeroelastic problems generally exist in modern turbomachinery designs [7]. This situation coupled with the inadequate modeling of blade row interaction, is believed to be the cause for a number of unexpected HCF failures [8,9]. Thus, a computational model which precisely accounts for Fluid Structure Interaction (FSI), inviscid-viscid interaction, and multi-blade row interaction is needed by designers to predict HCF and unsteady aeroelastic phenomena of current and future turbomachinery designs.

1.1 Research Objectives

The goal of this research is to develop an aeroelastic solver for the design of advanced turbomachinery. However, this lofty goal implies several objectives which need to be met in order to achieve such a design tool. First, in order to obtain usable results, the fluid solver must be capable of handling the deforming fluid grids which arise from the deformation of the blade. This entails implementing coordinate transformation metrics (both spatial and temporal) that do not violate the conservation of both surfaces and volumes under deformation.

Another important objective, in order for this tool to be utilized in the time limited design environment, is the reduction of solution runtime. This objective is limited to three main areas in this research for which it can be effectively achieved. The first is to incorporate a wall function into the chosen flow solver, Corsair [10], to reduce the grid density required near surfaces for the calculation of shear stresses. By reducing the grid density near surfaces, the total number of grid points in the computational domain and thus the simulation runtime is significantly reduced. A second area of focus is to incorporate additional parallelization via domain decomposition of individual fluid grids in the radial direction. By dividing the computational domain into pieces and solving these on separate cores/nodes simultaneously, the simulation runtime is again reduced. Lastly, a third area involves optimization of the flow solver code itself. While labor and time intensive, the rewriting/restructuring of older codes (such as Corsair) is often rewarded with impressive performance improvements, mainly due to the correction of unobserved bugs/flaws which arise over time via modification of the original source code.

The final objective for the development of any computational tool is thorough testing and results. For this research effort, testing against the well understood flexible cylinder in cross flow is utilized. In addition, the resulting aeroelastic solver is used to predict the major vibrational modes of a turbine blade from the fourth standard configuration.

1.2 Literature Review

A key development in the early understanding of aeroelasticity was made by Lane who introduced the concept of the interblade phase angle [11]. In this concept, the individual blades in a cascade are assumed to vibrate with the same amplitude but the maximum is reached with a constant phase lag, i.e. the interblade phase angle. Armed with this assumption, the structure and the fluid are decoupled so that a free vibration problem (taking no account of the aerodynamic loads) can first be solved. The predicted mode-shapes are then utilized with arbitrary amplitudes to produce prescribed blade motion. The unsteady fluid problem is then solved with this prescribed blade motion and the resulting unsteady aerodynamic forces on the blade calculated. These unsteady aerodynamic forces are then used to measure the stability of the system. This is often referred to as the classical method and became popular early in computational aerelastic research for two main reasons [12]. First, assumptions had to be made in order to solve the complicated differential equations of motions with the limited computing power available. Second, there has been a tendency to use existing aerodynamic and structural codes separately with a minimum of changes to either one in order to accommodate the other.

Although several methods have been developed to measure the stability from the unsteady aerodynamic forces, the most popular by far has been the aeroelastic eigensolution method [13]. This method is based on expressing the resulting unsteady aerodynamic forces in the frequency domain, either directly if analytical theories are used or by Fourier analysis if the forces are calculated in the time domain. The resulting aeroelastic equations of motion are very similar to the structural equations, with the aerodynamic contributions being added to the mass and/or stiffness matrices. The stability of the system is then assessed by determining the amount of damping required for each aeroelastic mode. The main advantage of this method lies in its simplified representation of the structural dynamics, which allows parametric studies to be conducted with a minimum of computational effort. Various cascades have been studied using this technique over the last 30 years, with various simplifications and improvements to the flow solvers used [14,15,16,17,18].

Integrated aeroelastic methods do not uncouple the fluid motion from that of the structure, but instead treat the problem of aeroelasticity in one continuous medium. The need for such an approach arises from the nonlinear response of the fluid flow to the motion of solid boundaries, especially in the transonic regime where flutter often occurs. Hence, the resulting mathematical formulation must allow the fluid to modify the structural motion and vice-versa, as such phenomena occur in nature. It then becomes possible to include nonlinear effects for both the fluid and the structure and take into account various interactions that can take place between them. The most striking difference between the classical method and the integrated method is that the former can only predict the onset of flutter as a sudden change from a stable to an unstable region while the latter is capable of predicting limit-cycle behavior. The engineering value of such prediction methods is evident since there is enough experimental evidence to suggest that flutter occurs in pockets of the limit cycle with varying amplitude levels [4].

This observation has a crucial implication on flutter analyses. The prediction of flutter onset may not be as important as predicting the actual vibration amplitude, since limit cycles can be tolerated if their amplitude is small.

Early integrated aeroelastic models typically incorporated an inviscid 2D Euler solver with an extremely simplified linear structural model consisting of springs, masses, and dampeners [14,19,20,21,22]. While the airfoil was allowed to move in response to aerodynamic forces and moments, the airfoil shape was kept rigid. In addition, many of these early models were restricted to a two-degrees-of-freedom structural model (pitch and plunge). These models have been extensively used in past research to determine the so-called flutter bucket or the reduced speed at which flutter occurs. However, due the extremely simplified structural models used, these early efforts are also commonly referred to as a classical method [4].

While studies using both these classical methods have provided important first steps in the prediction of unsteady aeroelastic phenomena, they lack the nonlinear response of the structure and thus the complete flow physics resulting from FSI [7]. Thus, recent efforts in the area of aeroelastic CFD research has involved the coupling of fluid and structural solvers, where both solvers are capable of handling full nonlinear effects, such as those that occur in transonic turbomachinery. Different strategies can be used to obtain a solution of the coupled fluid structure system. The first possibility is to use a strong coupling, sometimes referred to as a fully integrated method, where the structural and fluid dynamics equations are solved together at each time step using the same integrator. This is done by discretizing the two domains into one Arbitrary Lagrangian-Eulerian (ALE) space, the result of which is that the motion of the grid becomes an integral part of the equations of motion and does not have to be handled separately [23].

Bendiksen [24] applied a direct version of this method to both wing and turbomachinery blade flutter. His method used an explicit temporal discretization which is integrated using a five-stage Runge-Kutta scheme, with upwind differencing used for the spatial discretization of the arbitrary Lagrangian-Eulerian formulation. The structural equations are formulated on a local node level which enables them to be discretized using the same five-stage Runge-Kutta integrator. This model is claimed to calculate the energy transfer between the structure and fluid more accurately than similar schemes. For the flutter analysis, a typical isolated wing section was modeled, with the section allowed to have camber bending. This chord wise flexibility was modeled using plate-type finite elements of unit width. Results from this case were compared to those from classical methods showing excellent agreement. In addition, the results suggest that camber bending plays an important role in transonic flutter, possibly due to the mixed subsonic-supersonic flow field being sensitive to the airfoil boundary condition in the supersonic region of the flow. Calculations were also made on a cascade with solid titanium blades. This case demonstrated that camber bending can reach significant amplitudes during transonic flutter of thin compressor blades.

Masud [25] developed a space-time finite element formulation of the Navier-Stokes equations that was stabilized using the Galerkin/least-squares approach. The variational equation was based on the time discontinuous Galerkin method and was written in terms of physical entropy variables over the moving and deforming space time slabs. This formulation thus becomes analogous to the ALE formulation discussed previously including viscous effects. To demonstrate the versatility of this method, numerical simulations of a projectile moving in a stationary flow field were presented.

Gottfried and Fleeter [23,26] extended ALE3D, a 3D finite element Euler solver, to model the unsteady aerodynamics of stator-rotor interaction in turbomachinery. Simulations of a transonic compressor at Purdue University with the code, renamed TAM-ALE3D, showed good prediction of both subsonic and transonic steady state conditions. However, the simulation over-predicted the unsteady IGV lift magnitude by 100% for the subsonic case. In the transonic case, the simulated IGV lift lacked the higher harmonic content of the experimental data. The discrepancies between experimental and simulated results were attributed to scaling of the geometry and the lack of viscous effects.

Sadeghi and Liu [27] investigated the effects of frequency mistuning on cascade flutter using a similar ALE formulation. The unsteady structural and Euler equations were simultaneously integrated in time. A second order accurate implicit finite-volume scheme was used to solve both the flow equations and structural model. Using this model, simulations were performed for a turbine cascade with flutter in the bending mode and with alternate mistuning of the structural eigen frequency. An important finding of this study was that the fluid-structure interaction tended to decrease the effective amount of mistuning. Along similar lines, it was discovered that a minimum amount of mistuning was required to stabilize the cascade. Similar behavior was demonstrated for a compressor cascade.

While closely-coupled methods show promise, the approach requires an enormous amount of computational power along with almost a complete rewrite of the solver.

Additionally, the matrix system for the coupled problem is in general ill-conditioned as a result of the difference in stiffness of the fluid and the solid. A more reasonable approach is to use a loosely coupled method. In this method, the fluid and solid variables are updated alternatively by independent CFD and CSD codes which exchange boundary information at each time step in a time accurate manner. The most attractive feature of this approach is that the CFD and CSD solvers are largely independent of one another. This allows efficient re-use of codes that have been developed over several years and have been extensively tested. In addition, different fluid and structural models can be interchanged according to the requirements of a particular application. For example, CFD solvers for modeling transonic flow are very different from those used for the hypersonic regime. Likewise, different CSD models exist for types of structures, ranging from metal matrices to composites and even nanostructures [28].

Srivastava et al. [29] developed an efficient three-dimensional hybrid scheme by loosely coupling an ADI Euler solver with the commercial CSD package NASTRAN to analyze two advanced propeller designs. Their scheme treated the spanwise direction semi-explicitly and the other two directions implicitly. They noted that accuracy when compared to a fully implicit scheme was not affected, while providing advantages of reduced computational requirements in both memory and time. The calculated power coefficients for the advanced designs at various operating conditions showed good correlation with experimental data and varied up to 40% from CFD simulations run without aeroelastic deformation. Spanwise distribution of elemental power coefficients and steady pressure coefficient differences were in good agreement with experimental data. However, their study also uncovered that adjustments to the setting angle by rigid-body rotation did not simulate the correct blade shape. A follow up study by Yamamoto et al. [30] of the effect of structural flexibility on the performance of these propeller designs showed that structural deformation due to centrifugal and steady aerodynamic loading were important for improved correlation to experimental data. In addition, it was noted that structural deformation from unsteady aerodynamic forces played a key role in the performance of the designs.

Sayma et al. [31] developed a model for forced response prediction in turbomachinery blades. Their three-dimensional multi-passage, multi-blade-row calculations coupled both the fluid and the structure through an exchange of boundary conditions at every time step. The structure was represented by a linear modal model obtained from a standard FEA formulation, while the flow analysis was performed using a three-dimensional time-accurate viscous model using unstructured grids. Variables were interpolated at the sliding boundaries between the rotor and the stator in a conservative manner in order to allow a free movement of discontinuities. This model was used to study an intermediate pressure turbine in order to rank the magnitude of the fluid forcing resulting from two types of nozzle guide vanes. A sector of one stator and five rotor blades was analyzed for both types of nozzle guide vanes and the results obtained showed good agreement with available experimental data.

Vahdati et al. [32] used the same model to predict both the blade passing and low engine order forced response of a low pressure turbine. The predicted force response vibration amplitudes for a 24 nodal diameter resonance were found to be in good agreement with measured data but one of the main uncertainties was identified as the determination of the inherent mechanical damping. In addition, use of a whole-annulus

2-row model showed that non-uniform spacing of the stator blades gave rise to low engine order excitation. Breard et al. [33] also used this same model to perform a flutter analysis of a complete civil aero-engine fan assembly for three different configurations: no intake, symmetric intake, and non-symmetric flight intake. The blade's dynamic behavior was found to be different for each of these configurations, demonstrating the influence of intake ducts on flutter stability.

Servera et al. [34] investigated the use of a loose coupling between a CSD model for the analysis of helicopter rotor blades called HOST, and an Euler solver for computing the trim of flexible rotors in steady forward flight called WAVES. This coupling was used to analyze two advanced helicopter rotor designs and showed that a simultaneous coupling of the lift, pitching moment, and drag parameters is required in order to obtain a converged solution independent of simplified aerodynamic models. In addition, the coupled model showed significant improvements on the pitching moment and torsion predictions.

Carstens et al. [35] compared results from a loosely-coupled algorithm of a low pressure compressor at design conditions to those from a classical analysis using LIN3D. to those from a classical analysis using LIN3D of a low pressure compressor at design conditions The structural model consisted of an FEA model time-integrated using the Newmark algorithm, while the unsteady aerodynamics were computed using a Navier-Stokes code. An automatic grid generator was used to dynamically deform the mesh and couple the two codes together. This model was then used to analyze an assembly of highly loaded compressor blades in transonic flow. They found that the loosely-coupled algorithm yielded lower aerodynamic damping over the full range of interblade phase angles, unlike the classical LIN3D analysis. A striking result of the coupled algorithm was the negative damping for an interblade phase angle of 0, which might cause self-excited vibrations if no structural damping were present to keep the system stable.

1.3 Technical Approach

An aeroelastic computational model is built from an existing, well-developed ideal-gas, compressible, turbomachinery flow solver called Corsair. To account for the deformations from unsteady aerodynamic loadings, Corsair is loosely coupled to the commercial CSD code Ansys® through the use of a general FSI module [36]. This general FSI module handles the calling and setup of the CSD model, conversion of surface fluid stresses to structural forces, time stepping of the CSD model, and morphing of the fluid grid to match deformations predicted by the CSD model. By using this general FSI module, the resulting CFD – CSD coupling remains flexible and can take advantage of utilizing different CSD models.

To accomplish the CFD – CSD coupling, significant modifications to Corsair were required. Improved methods for numerical evaluation of the coordinate transformation metrics to handle grid deformations introduced by the FSI module are studied. The optimal methods for the spatial and temporal metrics from this study are then used in Corsair for the remaining research. A wall function with user specified surface roughness is also implemented into Corsair, allowing a significant reduction in grid density requirements for accurate prediction of shear stresses along solid surfaces. Following the implementation and verification of the wall function, an investigation is performed comparing the wall function against the finite difference approach used in the current release of Corsair to gauge performance differences and accuracy. To reduce simulation runtimes on non-SMP super-computers such as PC Beowulf clusters[37], the common data model used in Corsair is converted to a distributed data model resulting in a much smaller per nodal memory footprint. This change lead to a complete rewriting and restructuring of the source code, the result of which is called Thunder. To increase parallelization, radial decomposition of individual grids is also implemented into solver. A utility to optimize the decomposition of each grid is created, requiring only the number of pieces each grid is to be broken into to be specified by the user. Comparisons are then made between the original version of Corsair and the improved model called Thunder to demonstrate parallel scalability, performance, and reduction in nodal memory requirements.

To test the FSI model, two simplified configurations are utilized. First, the well understood case of a flexible cylinder in cross flow is studied with the natural frequency of the cylinder set to the shedding frequency of the Von Karman Streets. The cylinder is self excited, demonstrating the exchange of energy between the fluid and structural models. The second test case is based on the fourth standard configuration and demonstrates the ability of the FSI model to predict the dominant vibrational modes of an aeroelastic turbomachinery blade. For this case, a single blade from the fourth standard configuration is subjected to a step function from zero loading to the converged flow solution loading in order to excite the structural modes of the blade. These modes are then compared to those obtained from an in vacuo analysis using Ansys®.

2. CFD MODEL – CORSAIR

Before any of the required modifications to the flow solver chosen for this research could be made, especially to the structure of the code itself, a somewhat detailed understanding of the solution methods employed in Corsair was first required. Since no other publications or sources for Corsair exist with the needed level of detail, the source code itself was painstakingly analyzed and documented. This chapter is the result of that effort and provides a detailed look at the solution method employed by Corsair, including grid generation, numerical formulation, and boundary conditions.

The unsteady aeroelastic solver developed in this research is based on a well established turbomachinery CFD code called Corsair [10], distributed by the NASA Marshal Space Flight Center. Corsair is a three-dimensional Reynolds Averaged Navier Stokes (RANS) flow solver for axial turbomachinery geometries. It uses an overset structured grid topography consisting of O-grids around blades and H-grids for passages. In addition, a clearance grid composed of an O-grid with a collapsed centerline, can be used in the outer tip of an O-grid to include tip clearance flows in simulations.

2.1 Grid Generation

The first step in using any CFD model is to generate a set of grids over which the solution will be solved. Corgrid is a three-dimensional structured zonal-grid generator specifically designed for use with Corsair. A set of overlaid O- and H-grids are generated for each blade being modeled at constant radial span-wise locations. Algebraically generated H-grids are used in the regions upstream of the leading edge, downstream of the trailing edge, and in the inter-blade region. O-grids, which are body fitted to the surface of the blade airfoil, are used to properly resolve the viscous flow in the blade passages and are generated using an elliptic equation solver. As with most grid generation packages, grids can be clustered around areas of high curvature and near the hub, shroud, and blade surfaces. For blades with a tip clearance, a second O-grid is generated using a collapsed center-line to fill in the gap.

Construction of the algebraically generated H-grids begins with the calculation of the airfoil mean camber line. The mean camber line is extended upstream of the airfoil leading edge and downstream of the airfoil trailing edge using decay functions to control the incremental changes in the axial and circumferential spacing. Half the blade pitch is added to and subtracted from every computational grid point along the extended camber line to form the first and last grid lines in the blade-to-blade direction. Computational grid lines are then added at equal spatial increments between the first and last grid lines in the blade-to-blade direction. In addition, grid lines can be clustered in both the axial and circumferential directions upstream of the airfoil leading edge and downstream of the airfoil trailing edge.

Generation of the O-grids begins with the specification of four points on the H-grid which define a box that delineates the outer boundary of the O-grid. This outer boundary is smoothed to eliminate discontinuities in the slope of the grid lines at the corners of the box. The inner boundary of the O-grid is simply the surface of the airfoil.

An elliptical solution procedure is then used to produce a nearly orthogonal grid [38]. The elliptic equations are:

$$\alpha x_{\xi\xi} - 2\beta x_{\xi\eta} + \gamma x_{\eta\eta} = -J^2\left(Px_\xi + Qx_\eta\right) \tag{2-1}$$

$$\alpha y_{\xi\xi} - 2\beta y_{\xi\eta} + \gamma y_{\eta\eta} = -J^2\left(Py_\xi + Qy_\eta\right) \tag{2-2}$$

where

$$\alpha = x_\xi^2 + y_\eta^2 \tag{2-3}$$

$$\beta = x_\xi x_\eta + y_\xi y_\eta \tag{2-4}$$

$$\gamma = x_\xi^2 + y_\xi^2 \tag{2-5}$$

Here, x, y, and z are the Cartesian coordinates and subscripts ξ, η, and ζ are the curvilinear (or body fitted) coordinates in the axial, radial, and circumferential directions respectively and represent derivatives in those directions, J is the Jacobian matrix of curvilinear coordinate transformation, P and Q are forcing functions used to control the computational point clustering and orthogonality near solid walls. Equations 2-1 and 2-2 are solved using a successive line over-relaxation technique.

To define the overlap region between the O- and H-grids, a second set of four points on the H-grid are specified which form a box inside the outer boundary of the O-grid and define the inner boundary of the H-grid. The points inside the inner boundary of the H-grid are treated as i-blanked points, i.e. the equations of motion are not solved at these points. However, in the overlap region between the two boxes, the equations of motion are solved on both the O- and H-grids. Increasing the amount of overlap between the O- and H-grids enhances the stability and accuracy of the flow solution, but also increases the computational time by increasing the number of redundant grid points in the calculation. A typical overlaid O-H grid is illustrated in Figure 2-1.

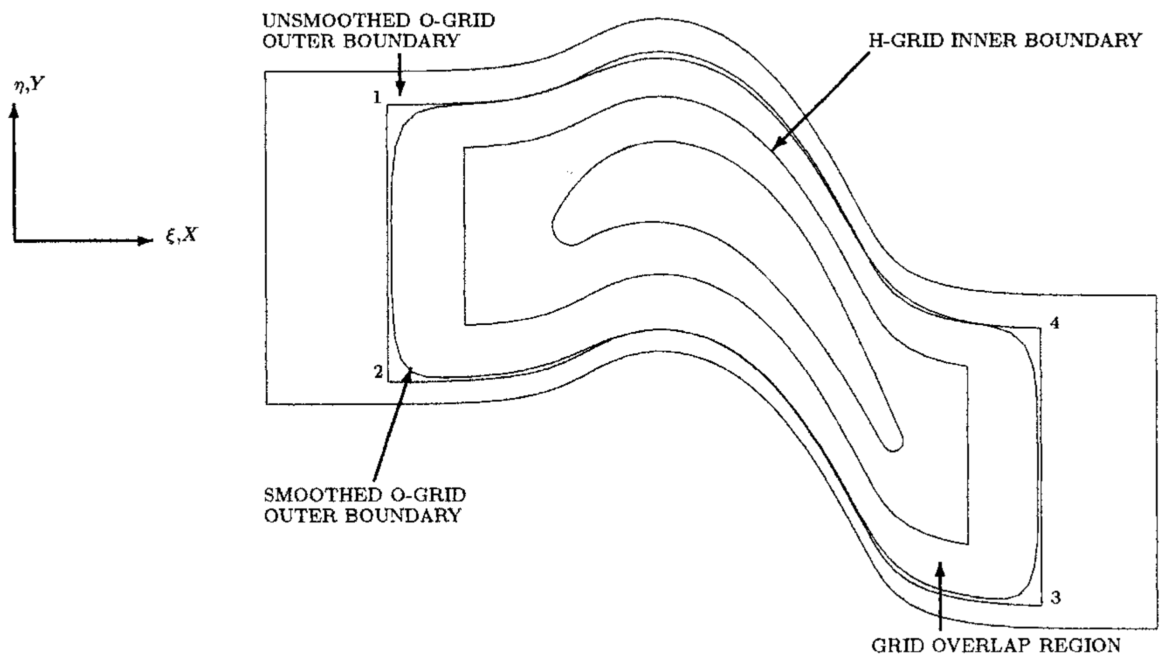

η,Y
ξ,X
UNSMOOTHED O-GRID OUTER BOUNDARY
H-GRID INNER BOUNDARY
1
2
3
4
SMOOTHED O-GRID OUTER BOUNDARY
GRID OVERLAP REGION

Figure 2-1. Overlaid O-H grid topography

2.1 Numerical Model

Corsair is a three-dimensional, implicit, multi blade row flow solver designed for time accurate simulations of turbomachinery [39]. It utilizes a dual-time-step to solve the full, unsteady, Navier-Stokes equations in a time accurate manner by means of a linearized, approximately factored, upwind finite-difference scheme. The resulting solution is third order spatial and second order temporal accurate. The integration scheme begins with the three-dimensional unsteady Navier-Stokes equations in strong-conservation dual-time-step form:

$$Q_t + Q_{t'} + E_x + F_y + G_z = E_x^v + F_y^v + G_z^v \tag{2-6}$$

where *t* represents the physical time step and *t*' represents the pseudo-time step for subiterations.

The vector of conservative variables *Q*, the inviscid flux vectors *E F G*, and the viscid flux vectors E^v F^v G^v, are given by:

$$Q = \begin{pmatrix} \rho \\ \rho u \\ \rho v \\ \rho w \\ e_t \end{pmatrix} \quad E = \begin{pmatrix} \rho u \\ p + \rho u^2 \\ \rho uv \\ \rho uw \\ (e_t + p)u \end{pmatrix} \quad F = \begin{pmatrix} \rho v \\ \rho uv \\ P + \rho v^2 \\ \rho uw \\ (e_t + p)v \end{pmatrix} \quad G = \begin{pmatrix} \rho w \\ \rho uw \\ \rho vw \\ P + \rho w^2 \\ (e_t + p)w \end{pmatrix}$$

$$E^v = \begin{pmatrix} 0 \\ \tau_{xx} \\ \tau_{xy} \\ \tau_{xz} \\ \beta_x \end{pmatrix} \quad F^v = \begin{pmatrix} 0 \\ \tau_{yx} \\ \tau_{yy} \\ \tau_{yz} \\ \beta_y \end{pmatrix} \quad G^v = \begin{pmatrix} 0 \\ \tau_{zx} \\ \tau_{zy} \\ \tau_{zz} \\ \beta_z \end{pmatrix} \tag{2-7}$$

and the stress tensor is defined by:

$$\begin{aligned}
\tau_{xx} &= 2\mu u_x + \lambda(u_x + v_y + w_z) & \tau_{xy} &= \mu(u_y + v_x) & \tau_{yx} &= \tau_{xy} \\
\tau_{yy} &= 2\mu v_y + \lambda(u_x + v_y + w_z) & \tau_{xz} &= \mu(u_z + w_x) & \tau_{zx} &= \tau_{xz} \\
\tau_{zz} &= 2\mu w_z + \lambda(u_x + v_y + w_z) & \tau_{yz} &= \mu(v_z + w_y) & \tau_{zy} &= \tau_{yz}
\end{aligned}$$

$$\begin{aligned}
\beta_x &= u\tau_{xx} + v\tau_{xy} + w\tau_{xz} + q_x \\
\beta_y &= u\tau_{yx} + v\tau_{yy} + w\tau_{yz} + q_y \\
\beta_z &= u\tau_{zx} + v\tau_{zy} + w\tau_{zz} + q_z
\end{aligned} \tag{2-8}$$

$$q_x = kT_x \qquad q_y = kT_y \qquad q_z = kT_z$$

with Stokes hypothesis and the perfect gas law completing the equations of motion:

$$\lambda = -\tfrac{2}{3}\mu$$

$$e_t = \rho e + \frac{\rho\left(u^2 + v^2 + w^2\right)}{2} \qquad e = \frac{P}{\rho(\gamma - 1)} \qquad T = \frac{P}{\rho R} \qquad h = \frac{e + P}{\rho} \tag{2-9}$$

$$\gamma = \frac{c_p}{c_v} \qquad R = c_p - c_v$$

By defining the Prandtl number as

$$\Pr = \frac{\mu c_p}{k} \tag{2-10}$$

the heat flux terms in the conservation of energy equation are rewritten as

$$q_x = \gamma\mu \Pr^{-1} e_x \qquad q_y = \gamma\mu \Pr^{-1} e_y \qquad q_z = \gamma\mu \Pr^{-1} e_z \tag{2-11}$$

In Corsair, the equations of motion are non-dimensionalized so that certain parameters, such as the Reynolds number, can be varied independently. The non-dimensional variables used are as follows:

$$x^* = \frac{x}{L} \qquad t^* = \frac{t}{\left(L\sqrt{\gamma}/c\right)} \qquad v^* = \frac{v}{\left(\sqrt{P_\infty/\rho_\infty}\right)} \qquad \mu^* = \frac{\mu}{\mu_\infty}$$

$$U^* = \frac{U}{\left(c/\sqrt{\gamma}\right)} \qquad P^* = \frac{P}{P_\infty} \qquad \rho^* = \frac{\rho}{\rho_\infty} \qquad T^* = T \tag{2-12}$$

where *x* is a distance, *L* is the mid-span length in the first blade row, *t* is time, *v* is a velocity component, *c* is the free stream speed of sound, *γ* is the ratio of specific heats, *μ* is the viscosity, *U* is the wheel velocity, *P* is the static pressure, *ρ* is the density, *T* is temperature (in degrees Rankine), and the subscript ∞ refers to free stream conditions. Applying this to Equation 2.6, the equations of motion are rewritten as:

$$Q_{t^*} + Q_{(t')^*} + E_{x^*} + F_{y^*} + G_{z^*} = \mathrm{Re}^{-1}\left(E^v_{x^*} + F^v_{y^*} + G^v_{z^*}\right) \tag{2-13}$$

where the non-dimensionalized Reynolds number is given by:

$$\mathrm{Re} = \frac{\rho_\infty L c}{\mu_\infty \sqrt{\gamma}} \tag{2-14}$$

For the analysis of arbitrary geometries it is useful to generalize the equations of motion by expressing them in terms of body-fitted, curvilinear coordinates. The following independent variable transformation introduces body-fitted coordinates which allow accurate implementation of surface boundary conditions, since the geometric surface lies along a boundary of the computational domain:

$$\tau = t \quad \xi = \xi(x, y, z, t) \quad \eta = \eta(x, y, z, t) \quad \varsigma = \varsigma(x, y, z, t) \tag{2-15}$$

Applying these to Equation 2-13, the equations of motion now take the following form:

$$\tilde{Q}_\tau + \tilde{Q}_{\tau'} + \tilde{E}_\xi + \tilde{F}_\eta + \tilde{G}_\varsigma = \mathrm{Re}^{-1}\left(E^v_\xi + F^v_\eta + G^v_\varsigma\right) \tag{2-16}$$

where

$$\begin{aligned}
\tilde{Q} &= Q/J \\
\tilde{E}(Q,\xi) &= \left(\xi_{t^*} Q + \xi_{x^*} E + \xi_{y^*} F + \xi_{z^*} G\right)/J \\
\tilde{F}(Q,\eta) &= \left(\eta_{t^*} Q + \eta_{x^*} E + \eta_{y^*} F + \eta_{z^*} G\right)/J \\
\tilde{G}(Q,\varsigma) &= \left(\varsigma_{t^*} Q + \varsigma_{x^*} E + \varsigma_{y^*} F + \varsigma_{z^*} G\right)/J \\
\tilde{E}^v(\xi) &= \left(\xi_{x^*} E^v + \xi_{y^*} F^v + \xi_{z^*} G^v\right)/J \\
\tilde{F}^v(\eta) &= \left(\eta_{x^*} E^v + \eta_{y^*} F^v + \eta_{z^*} G^v\right)/J \\
\tilde{G}^v(\varsigma) &= \left(\varsigma_{x^*} E^v + \varsigma_{y^*} F^v + \varsigma_{z^*} G^v\right)/J
\end{aligned} \tag{2-17}$$

and the metrics of transformation are:

$$
\begin{aligned}
\xi_x &= J\left(y_\eta z_\varsigma - y_\varsigma z_\eta\right) & \xi_y &= J\left(x_\varsigma z_\eta - x_\eta z_\varsigma\right) & \xi_z &= J\left(x_\eta y_\varsigma - x_\varsigma y_\eta\right)\\
\eta_x &= J\left(y_\varsigma z_\xi - y_\xi z_\varsigma\right) & \eta_y &= J\left(x_\xi z_\varsigma - x_\varsigma z_\xi\right) & \eta_z &= J\left(x_\varsigma y_\xi - x_\xi y_\varsigma\right)\\
\varsigma_x &= J\left(y_\xi z_\eta - y_\eta z_\xi\right) & \varsigma_y &= J\left(x_\eta z_\xi - x_\xi z_\eta\right) & \varsigma_z &= J\left(x_\xi y_\eta - x_\eta y_\xi\right)
\end{aligned}
$$

$$
\begin{aligned}
\xi_t &= J\left[x_\tau\left(y_\varsigma z_\eta - y_\eta z_\varsigma\right) + y_\tau\left(x_\eta z_\varsigma - x_\varsigma z_\eta\right) + z_\tau\left(x_\varsigma y_\eta - x_\eta y_\varsigma\right)\right]\\
\eta_t &= J\left[x_\tau\left(y_\xi z_\varsigma - y_\varsigma z_\xi\right) + y_\tau\left(x_\varsigma z_\xi - x_\xi z_\varsigma\right) + z_\tau\left(x_\xi y_\varsigma - x_\varsigma y_\xi\right)\right]\\
\varsigma_t &= J\left[x_\tau\left(y_\eta z_\xi - y_\xi z_\eta\right) + y_\tau\left(x_\xi z_\eta - x_\eta z_\xi\right) + z_\tau\left(x_\eta y_\xi - x_\xi y_\eta\right)\right]
\end{aligned}
\qquad (2\text{-}18)
$$

$$
J^{-1} = x_\xi\left(y_\eta z_\varsigma - y_\varsigma z_\eta\right) - x_\eta\left(y_\xi z_\varsigma - y_\varsigma z_\xi\right) + x_\varsigma\left(y_\xi z_\eta - y_\eta z_\xi\right)
$$

Application of a second order central approximation for physical time and a first order backward approximation for pseudo time to Equation 2-16 gives the general implicit formulation used in Corsair to solve the equations of motion:

$$
\begin{aligned}
&\tfrac{1}{\Delta\tau}\left(\tfrac{3}{2}\tilde{Q}^{n+1,k} - 2\tilde{Q}^{n} + \tfrac{1}{2}\tilde{Q}^{n-1}\right) + \tfrac{1}{\Delta\tau'}\left(\tilde{Q}^{n+1,k+1} - \tilde{Q}^{n+1,k}\right) + \tilde{E}_\xi^{n+1} + \tilde{F}_\eta^{n+1} + \tilde{G}_\varsigma^{n+1}\\
&= \mathrm{Re}^{-1}\left[\left(\tilde{E}_\xi^{v}\right)^{n+1} + \left(\tilde{F}_\eta^{v}\right)^{n+1} + \left(\tilde{G}_\varsigma^{v}\right)^{n+1}\right]
\end{aligned}
\qquad (2\text{-}19)
$$

In Equation 2-19, *n* denotes a physical time step and *k* denotes a pseudo time step. While a second order accurate difference is required for the physical time in order for the method to be time accurate, a first order difference is sufficient for pseudo time steps, since the solution is iterated in pseudo time to convergence at each physical time step.

Note that Equation 2-19 is non-linear. To solve the equations of motion in an efficient computational manner, linearization in the form of a Taylor series expansion with use of the pseudo time step, τ', is utilized:

$$
\begin{aligned}
\tilde{E}_{\xi}^{n+1} &\approx \partial_{\xi}\hat{E}^{n} + \partial_{\xi}\left(\frac{\partial \tilde{E}}{\partial \tilde{Q}}\right)\Delta\tilde{Q} \approx \partial_{\xi}\hat{E}^{n} + \partial_{\xi}\tilde{A}^{n}\tilde{Q}_{\tau'} \\
\tilde{F}_{\eta}^{n+1} &\approx \partial_{\eta}\hat{F}^{n} + \partial_{\eta}\left(\frac{\partial \tilde{F}}{\partial \tilde{Q}}\right)\Delta\tilde{Q} \approx \partial_{\eta}\hat{F}^{n} + \partial_{\eta}\tilde{B}^{n}\tilde{Q}_{\tau'} \\
\tilde{G}_{\varsigma}^{n+1} &\approx \partial_{\varsigma}\hat{G}^{n} + \partial_{\varsigma}\left(\frac{\partial \tilde{G}}{\partial \tilde{Q}}\right)\Delta\tilde{Q} \approx \partial_{\varsigma}\hat{G}^{n} + \partial_{\varsigma}\tilde{C}^{n}\tilde{Q}_{\tau'} \\
\left(\tilde{E}^{v}\right)_{\xi}^{n+1} &\approx \partial_{\xi}\left(\hat{E}^{v}\right)^{n} + \partial_{\xi}\left(\frac{\partial \tilde{E}^{v}}{\partial \tilde{Q}}\right)\Delta\tilde{Q} \approx \partial_{\xi}\left(\hat{E}^{v}\right)^{n} + \partial_{\xi}\left(\tilde{A}^{v}\right)^{n}\tilde{Q}_{\tau'} \\
\left(\tilde{F}^{v}\right)_{\eta}^{n+1} &\approx \partial_{\eta}\left(\hat{F}^{v}\right)^{n} + \partial_{\eta}\left(\frac{\partial \tilde{F}^{v}}{\partial \tilde{Q}}\right)\Delta\tilde{Q} \approx \partial_{\eta}\left(\hat{F}^{v}\right)^{n} + \partial_{\eta}\left(\tilde{B}^{v}\right)^{n}\tilde{Q}_{\tau'} \\
\left(\tilde{G}^{v}\right)_{\varsigma}^{n+1} &\approx \partial_{\varsigma}\left(\hat{G}^{v}\right)^{n} + \partial_{\varsigma}\left(\frac{\partial \tilde{G}^{v}}{\partial \tilde{Q}}\right)\Delta\tilde{Q} \approx \partial_{\varsigma}\left(\hat{G}^{v}\right)^{n} + \partial_{\varsigma}\left(\tilde{C}^{v}\right)^{n}\tilde{Q}_{\tau'}
\end{aligned}
\tag{2-20}
$$

where as before, a first order backward difference is used for the pseudo time step:

$$
\tilde{Q}_{\tau'} = \tfrac{1}{\Delta\tau'}\left(\tilde{Q}^{n+1,k+1} - \tilde{Q}^{n+1,k}\right) \tag{2-21}
$$

In Equation 2-20, the quantities $\tilde{A}, \tilde{B}, \tilde{C}, \tilde{A}^{v}, \tilde{B}^{v},$ and $\tilde{C}^{v}$ are referred as flux jacobians, while the quantities $\hat{E}, \hat{F}, \hat{G}, \hat{E}^{v}, \hat{F}^{v},$ and $\hat{G}^{v}$, are referred to as numerical fluxes and are consistent with the physical fluxes $\tilde{E}, \tilde{F}, \tilde{G}, \tilde{E}^{v}, \tilde{F}^{v},$ and $\tilde{G}^{v}$. Since the solution is iterated to convergence at each physical time step, error introduced by the linearization process is eliminated. However, the resulting formulation does require the storage of the solution at three previous time steps, two at a previously converged physical time step and one at the previous pseudo time step. Substituting Equations 2-20 into Equation 2-19 and rearranging terms results in:

$$\begin{aligned}&\left[I+\partial_\xi \tilde{A}^n-\mathrm{Re}^{-1}\partial_\xi\left(\tilde{A}^v\right)^n+\partial_\eta \tilde{B}^n-\mathrm{Re}^{-1}\partial_\eta\left(\tilde{B}^v\right)^n+\partial_\varsigma \tilde{C}^n-\mathrm{Re}^{-1}\partial_\varsigma\left(\tilde{C}^v\right)\right]\\&\left(\tilde{Q}^{n+1,k+1}-\tilde{Q}^{n+1,k}\right)=-\Big\{\tfrac{\Delta\tau'}{\Delta\tau}\left(\tfrac{3}{2}\tilde{Q}^{n+1,k}-2\tilde{Q}^n+\tfrac{1}{2}\tilde{Q}^{n-1}\right)\\&+\partial_\xi\hat{E}^n+\partial_\eta\hat{F}^n+\partial_\varsigma\hat{G}^n-\mathrm{Re}^{-1}\left[\partial_\xi\left(\hat{E}^v_\xi\right)^n+\partial_\eta\left(\hat{F}^v_\eta\right)^n+\partial_\varsigma\left(\hat{G}^v_\varsigma\right)^n\right]\Big\}\end{aligned} \qquad (2\text{-}22)$$

The implicit formulation of a 3-D equation, such as those in Equation 2-22, would normally result in a system of equation with a hepta-diagonal coefficient matrix. The solution of such a system, even with re-ordering techniques, is very time consuming and computationally expensive. To overcome this difficulty, Approximate Factorization (AF) along with the Alternating Direction Implicit (ADI) algorithm is used in Corsair. The AF reduces the hepta-diagonal coefficient matrix system to three tri-diagonal systems which are then sequentially solved using the ADI algorithm. The resulting solution method requires considerably less computational expense and is unconditionally stable. Since AF is applied to the LHS of Equation 2-22, the use of pseudo time steps to converge the solution at each physical time step reduces error caused by both the linearization and AF techniques together. In practice, three pseudo iterations are sufficient to reduce these errors down to machine zero. Different factorizations can be used in the AF technique, resulting in various orders of accuracy and computational expense. The most important rule of AF is to keep the factorization error (generation of extra terms) below the order of truncation for the desired solution while preserving existing terms. In Corsair, a fairly straight forward AF is used:

$$\begin{aligned}&\left[I+\partial_\xi\tilde{A}^n-\mathrm{Re}^{-1}\partial_\xi\left(\tilde{A}^v\right)^n\right]\left[I+\partial_\eta\tilde{B}^n-\mathrm{Re}^{-1}\partial_\eta\left(\tilde{B}^v\right)^n\right]\left[I+\partial_\varsigma\tilde{C}^n-\mathrm{Re}^{-1}\partial_\varsigma\left(\tilde{C}^v\right)^n\right]\\&\left(\tilde{Q}^{n+1,k+1}-\tilde{Q}^{n+1,k}\right)=-\left\{\tfrac{\Delta\tau'}{\Delta\tau}\left(\tfrac{3}{2}\tilde{Q}^{n+1,k}-2\tilde{Q}^n+\tfrac{1}{2}\tilde{Q}^{n-1}\right)\right.\\&\left.+\partial_\xi\hat{E}^n+\partial_\eta\hat{F}^n+\partial_\varsigma\hat{G}^n-\mathrm{Re}^{-1}\left[\partial_\xi\left(\hat{E}^v_\xi\right)^n+\partial_\eta\left(\hat{F}^v_\eta\right)^n+\partial_\varsigma\left(\hat{G}^v_\varsigma\right)^n\right]\right\}\end{aligned}\tag{2-23}$$

In Equation 2-23, all the fluxes are evaluated explicitly using the solution vector at the current pseudo time step, $\tilde{Q}^{n+1,k}$. For the inviscid numerical fluxes on the RHS, Roe's approximate Reiman solver scheme is utilized. This method accelerates the solution by taking advantage of the characteristics (propagation direction of information) of the equations of motion. In Corsair, Roe's scheme is given by:

$$\begin{aligned}\partial_\xi\hat{E}_{i,j,k}=\tfrac{1}{\Delta\xi}\Big[&\overline{E}_{i+1,j,k}-\overline{E}_{i,j,k}-\left(\Delta E^+_{i+1,j,k}-\Delta E^+_{i,j,k}\right)\\&+\phi_1\Delta E^+_{i+1,j,k}-\phi_2\Delta E^+_{i,j,k}-\phi_3\Delta E^+_{i-1,j,k}\\&+\phi_1\Delta E^-_{i,j,k}-\phi_2\Delta E^-_{i+1,j,k}-\phi_3\Delta E^-_{i+2,j,k}\Big]\end{aligned}\tag{2-24}$$

for the interior points and by:

$$\begin{aligned}\partial_\xi\hat{E}_{i,j,k}=\tfrac{1}{\Delta\xi}\Big\{&\overline{E}_{i+1,j,k}-\overline{E}_{i,j,k}-\left(\Delta E^+_{i+1,j,k}-\Delta E^+_{i,j,k}\right)\\&+0.1125\left[9-\max\left(\phi_0,5\right)\right]\left[\Delta E^+_{i+1}-\Delta E^+_i-\Delta E^-_{i+1}+\Delta E^-_i\right]\Big\}\end{aligned}\tag{2-25}$$

for the second and imax-1 points. Note that Equation 2-25 is a modified second order accurate formulation of Roe's scheme. In Equations 2-24 and 2-25, the + and – indicate contributions from downstream and upstream traveling characteristic waves respectively, where $\overline{E}$ represents the total flux given by:

$$\overline{E} = \begin{bmatrix} \rho\left(\xi_t + u\xi_x + v\xi_y + w\xi_z\right) \\ \rho u\left(\xi_t + u\xi_x + v\xi_y + w\xi_z\right) + \xi_x P \\ \rho v\left(\xi_t + u\xi_x + v\xi_y + w\xi_z\right) + \xi_y P \\ \rho w\left(\xi_t + u\xi_x + v\xi_y + w\xi_z\right) + \xi_z P \\ \left(\xi_t + u\xi_x + v\xi_y + w\xi_z\right)\left(e + P\right) - \xi_t P \end{bmatrix} \tag{2-26}$$

Additionally, the order of accuracy for the inviscid fluxes is controlled by ϕ_1, ϕ_2, and ϕ_3 according to Table 2-1. During the initial few blade passes of a new solution, the 1st order scheme is utilized to help progress the solution past start-up transients, thus saving the computational expense of resolving transients and accelerating the solution.

Scheme	ϕ_0	ϕ_1	ϕ_2	ϕ_3
1st order accurate upwind	9	0	0	0
2nd order accurate central	1	½	½	0
2nd order accurate upwind	-1	0	-½	½
Fromm's	0	1/4	0	1/4
3rd order accurate upwind	1/3	1/3	1/6	1/6

Table 2-1. List of difference schemes for inviscid numerical fluxes

The characteristic fluxes $\Delta E^{\pm}$ in Equations 2-24 and 2-25 are calculated according to:

$$\Delta E^{+} = \mathrm{X}_{\xi}\Lambda^{+}\mathrm{X}_{\xi}^{-1}\nabla\overline{Q}_{ROE} \qquad \Delta E^{-} = \left(\overline{E}_i - \overline{E}_{i-1}\right) - \Delta E^{+} \tag{2-27}$$

Where

$$\mathrm{X}_{\xi}=\begin{bmatrix} 2\bar{\xi}_x & 2\bar{\xi}_y & 2\bar{\xi}_z & \frac{1}{\bar{c}} & \frac{1}{\bar{c}} \\ 2\bar{u}\bar{\xi}_x & 2\bar{u}\bar{\xi}_y-2\bar{\xi}_z & 2\bar{u}\bar{\xi}_z+2\bar{\xi}_y & \frac{\bar{u}}{\bar{c}}+\bar{\xi}_x & \frac{\bar{u}}{\bar{c}}-\bar{\xi}_x \\ 2\bar{v}\bar{\xi}_x+2\bar{\xi}_z & 2\bar{v}\bar{\xi}_y & 2\bar{v}\bar{\xi}_z-2\bar{\xi}_x & \frac{\bar{v}}{\bar{c}}+\bar{\xi}_y & \frac{\bar{v}}{\bar{c}}-\bar{\xi}_y \\ 2\bar{w}\bar{\xi}_x-2\bar{\xi}_y & 2\bar{w}\bar{\xi}_y+2\bar{\xi}_x & 2\bar{w}\bar{\xi}_z & \frac{\bar{w}}{\bar{c}}+\bar{\xi}_z & \frac{\bar{w}}{\bar{c}}-\bar{\xi}_z \\ \begin{matrix}2\left(\bar{v}\bar{\xi}_z-\bar{w}\bar{\xi}_y\right)\\+\bar{U}\bar{\xi}\end{matrix} & \begin{matrix}2\left(\bar{w}\bar{\xi}_x-\bar{u}\bar{\xi}_z\right)\\+\bar{U}\bar{\xi}_y\end{matrix} & \begin{matrix}2\left(\bar{u}\bar{\xi}_y-\bar{v}\bar{\xi}_x\right)\\+\bar{U}\bar{\xi}_z\end{matrix} & \begin{matrix}\frac{\bar{U}}{2\bar{c}}+\frac{\bar{c}}{\gamma-1}\\+\bar{u}\bar{\xi}_x+\bar{v}\bar{\xi}_y+\bar{w}\bar{\xi}_z\end{matrix} & \begin{matrix}\frac{\bar{U}}{2\bar{c}}+\frac{\bar{c}}{\gamma-1}\\-\bar{u}\bar{\xi}_x-\bar{v}\bar{\xi}_y-\bar{w}\bar{\xi}_z\end{matrix} \end{bmatrix} \tag{2-28}$$

$$\mathrm{X}_{\xi}^{-1}=\begin{bmatrix} \bar{\xi}_x & 0 & \bar{\xi}_z\sqrt{\rho_{i-1}(\rho_i)} & -\bar{\xi}_y\sqrt{\rho_{i-1}(\rho_i)} & -\bar{\xi}_x\frac{1}{\bar{c}} \\ \bar{\xi}_y & -\bar{\xi}_z\sqrt{\rho_{i-1}(\rho_i)} & 0 & \bar{\xi}_x\sqrt{\rho_{i-1}(\rho_i)} & -\bar{\xi}_y\frac{1}{\bar{c}} \\ \bar{\xi}_z & \bar{\xi}_y\sqrt{\rho_{i-1}(\rho_i)} & -\bar{\xi}_x\sqrt{\rho_{i-1}(\rho_i)} & 0 & -\bar{\xi}_z\frac{1}{\bar{c}} \\ 0 & \bar{\xi}_x\sqrt{\rho_{i-1}(\rho_i)} & \bar{\xi}_y\sqrt{\rho_{i-1}(\rho_i)} & \bar{\xi}_z\sqrt{\rho_{i-1}(\rho_i)} & \frac{1}{\bar{c}} \\ 0 & -\bar{\xi}_x\sqrt{\rho_{i-1}(\rho_i)} & -\bar{\xi}_y\sqrt{\rho_{i-1}(\rho_i)} & -\bar{\xi}_z\sqrt{\rho_{i-1}(\rho_i)} & \frac{1}{\bar{c}} \end{bmatrix} \tag{2-29}$$

$$\nabla Q_{ROE}=\begin{bmatrix} \rho_i-\rho_{i-1} \\ u_i-u_{i-1} \\ v_i-v_{i-1} \\ w_i-w_{i-1} \\ P_i-P_{i-1} \end{bmatrix} \tag{2-30}$$

$$\bar{\xi}_x=\frac{\xi_x}{\sqrt{\xi_x^2+\xi_y^2+\xi_z^2}} \qquad \bar{\xi}_y=\frac{\xi_y}{\sqrt{\xi_x^2+\xi_y^2+\xi_z^2}} \qquad \bar{\xi}_z=\frac{\xi_z}{\sqrt{\xi_x^2+\xi_y^2+\xi_z^2}}$$

$$\bar{u}=\frac{u_{i-1}\sqrt{\rho_{i-1}}+u_i\sqrt{\rho_i}}{\sqrt{\rho_{i-1}}+\sqrt{\rho_i}} \qquad \bar{v}=\frac{v_{i-1}\sqrt{\rho_{i-1}}+v_i\sqrt{\rho_i}}{\sqrt{\rho_{i-1}}+\sqrt{\rho_i}} \qquad \bar{w}=\frac{w_{i-1}\sqrt{\rho_{i-1}}+w_i\sqrt{\rho_i}}{\sqrt{\rho_{i-1}}+\sqrt{\rho_i}}$$

$$\bar{h}=\frac{h_{i-1}\sqrt{\rho_{i-1}}+h_i\sqrt{\rho_i}}{\sqrt{\rho_{i-1}}+\sqrt{\rho_i}} \qquad \bar{U}=\bar{u}^2+\bar{v}^2+\bar{w}^2 \qquad \bar{c}=\sqrt{(\gamma-1)\left(\bar{h}-\tfrac{1}{2}\bar{U}\right)}$$

and the positive eigenvalue matrix is defined as:

$$\Lambda^{+} = \begin{bmatrix} \lambda_1 & 0 & 0 & 0 & 0 \\ 0 & \lambda_2 & 0 & 0 & 0 \\ 0 & 0 & \lambda_3 & 0 & 0 \\ 0 & 0 & 0 & \lambda_4 & 0 \\ 0 & 0 & 0 & 0 & \lambda_5 \end{bmatrix} \qquad \begin{aligned} \lambda_1 &= \lambda_2 = \lambda_3 = \xi_t + \overline{u}\,\xi_x + \overline{v}\,\xi_y + \overline{w}\,\xi_z \\ \lambda_4 &= \lambda_1 + \overline{c}\sqrt{\xi_x^2 + \xi_y^2 + \xi_z^2} \\ \lambda_5 &= \lambda_1 - \overline{c}\sqrt{\xi_x^2 + \xi_y^2 + \xi_z^2} \end{aligned} \tag{2-31}$$

Since Roe's scheme may encounter difficulties in stability and convergence near sonic lines and expansion waves, the following correction for the eigenvalues is used in Corsair:

$$\begin{aligned} &\varepsilon = \tfrac{1}{2}\overline{c}\sqrt{\xi_x^2 + \xi_y^2 + \xi_z^2} \\ &\text{if } |\lambda_i| \ge \varepsilon \quad \rightarrow \quad \lambda_i = \tfrac{1}{2}\lambda_i \\ &\text{if } |\lambda_i| < \varepsilon \quad \rightarrow \quad \lambda_i = 2\left[\lambda_i + \tfrac{1}{2}\left(\frac{\varepsilon + |\lambda_i|^2}{\varepsilon}\right)\right] \end{aligned} \tag{2-32}$$

Additionally, flux limiter can be added to Roe's scheme in corsair to increase accuracy and reduce oscillations near large gradients. To do this, Equation 2-24 is rewritten as:

$$\begin{aligned} \partial_{\xi}\hat{E}_{i,j,k} = \overline{E}_{i+1,j,k} - \overline{E}_{i,j,k} &- \left(\Delta E^{+}_{i+1,j,k} - \Delta E^{+}_{i,j,k}\right) \\ &+ \phi_1\left(\Delta E_4^{+} - \Delta E_2^{+}\right) + \phi_3\left(\Delta E_3^{+} - \Delta E_1^{+}\right) \\ &+ \phi_1\left(\Delta E_4^{-} - \Delta E_2^{-}\right) + \phi_3\left(\Delta E_3^{-} - \Delta E_1^{-}\right) \end{aligned} \tag{2-33}$$

where

$$\begin{aligned} \Delta E_1^{+} &= \min\text{mod}\left(\Delta E_{i-1}^{+}, \beta\Delta E_i^{+}\right) & \Delta E_1^{-} &= \min\text{mod}\left(\Delta E_{i+2}^{-}, \beta\Delta E_{i+1}^{-}\right) \\ \Delta E_2^{+} &= \min\text{mod}\left(\Delta E_i^{+}, \beta\Delta E_{i-1}^{+}\right) & \Delta E_2^{-} &= \min\text{mod}\left(\Delta E_{i+1}^{-}, \beta\Delta E_{i+2}^{-}\right) \\ \Delta E_3^{+} &= \min\text{mod}\left(\Delta E_i^{+}, \beta\Delta E_{i+1}^{+}\right) & \Delta E_3^{-} &= \min\text{mod}\left(\Delta E_{i+1}^{-}, \beta\Delta E_i^{-}\right) \\ \Delta E_4^{+} &= \min\text{mod}\left(\Delta E_{i+1}^{+}, \beta\Delta E_i^{+}\right) & \Delta E_4^{-} &= \min\text{mod}\left(\Delta E_i^{-}, \beta\Delta E_{i+1}^{-}\right) \end{aligned} \tag{2-34}$$

and the compression factor β and the minmod function are defined as:

$$\beta = \frac{3-\phi_0}{1-\phi_0}$$

$$\min \operatorname{mod}(a,b) = \left(\frac{a}{|a|}\right) \max\left[0, \min\left(|a|, b\frac{a}{|a|}\right)\right] \tag{2-35}$$

The terms $\partial_\eta \hat{F}_\eta$ and $\partial_\varsigma \hat{G}_\varsigma$ are obtained from Equations 2-24 through 2-35 by simply replacing *ξ, i, j, k* with *η, j,i,k* or *ς, k, i, j* respectively.

The viscid numerical flux terms in Equation 2-23 are calculated using a simple central difference scheme:

$$\partial_\xi \hat{E}^v_{i,j,k} = \tfrac{1}{\Delta\xi}\left[\overline{E}^v_{i+1,j,k} - \overline{E}^v_{i,j,k}\right] \tag{2-36}$$

where

$$\overline{E}^v = \begin{bmatrix} 0 \\ \xi_x\tau_{xx} + \xi_y\tau_{xy} + \xi_z\tau_{xz} \\ \xi_x\tau_{xy} + \xi_y\tau_{yy} + \xi_z\tau_{yz} \\ \xi_x\tau_{xz} + \xi_y\tau_{yz} + \xi_z\tau_{zz} \\ \xi_x\beta_x + \xi_y\beta_y + \xi_z\beta_z \end{bmatrix} \tag{2-37}$$

and

$$
\begin{aligned}
\tau_{xx} &= \mu\left[2u_x - \tfrac{2}{3}\left(u_x + v_y + w_z\right)\right] & \tau_{xy} &= \mu\left(u_y + v_x\right)\\
\tau_{yy} &= \mu\left[2v_y - \tfrac{2}{3}\left(u_x + v_y + w_z\right)\right] & \tau_{xz} &= \mu\left(u_z + w_x\right)\\
\tau_{zz} &= \mu\left[2w_z - \tfrac{2}{3}\left(u_x + v_y + w_z\right)\right] & \tau_{yz} &= \mu\left(v_z + w_y\right)
\end{aligned}
$$

$$
\begin{aligned}
\beta_x &= \overline{u}\,\tau_{xx} + \overline{v}\,\tau_{xy} + \overline{w}\,\tau_{xz} + \gamma\mu\,\mathrm{Pr}^{-1} e_x\\
\beta_y &= \overline{u}\,\tau_{xy} + \overline{v}\,\tau_{yy} + \overline{w}\,\tau_{yz} + \gamma\mu\,\mathrm{Pr}^{-1} e_y\\
\beta_z &= \overline{u}\,\tau_{xz} + \overline{v}\,\tau_{yz} + \overline{w}\,\tau_{zz} + \gamma\mu\,\mathrm{Pr}^{-1} e_z
\end{aligned}
$$

$$
\begin{aligned}
u_\xi &= \left(u_i - u_{i-1}\right) & u_x &= u_\xi \xi_x & u_y &= u_\xi \xi_y & u_z &= u_\xi \xi_z\\
v_\xi &= \left(v_i - v_{i-1}\right) & v_x &= v_\xi \xi_x & v_y &= v_\xi \xi_y & v_z &= v_\xi \xi_z\\
w_\xi &= \left(w_i - w_{i-1}\right) & w_x &= w_\xi \xi_x & w_y &= w_\xi \xi_y & w_z &= w_\xi \xi_z\\
e_\xi &= \left(e_i - e_{i-1}\right) & e_x &= e_\xi \xi_x & e_y &= e_\xi \xi_y & e_z &= e_\xi \xi_z
\end{aligned}
\tag{2-38}
$$

$$
\overline{u} = \tfrac{1}{2}\left(u_{i-1} + u_i\right) \qquad \overline{v} = \tfrac{1}{2}\left(v_{i-1} + v_i\right) \qquad \overline{w} = \tfrac{1}{2}\left(w_{i-1} + w_i\right)
$$

$$
e_i = \frac{\left(e_t\right)_i}{\rho_i} - \tfrac{1}{2}\left(u_i^2 + v_i^2 + w_i^2\right)
$$

As with the inviscid numerical flux terms, the terms $\partial_\eta \hat{F}_\eta^v$ and $\partial_\varsigma \hat{G}_\varsigma^v$ are obtained from Equations 2-36 through 2-38 by simply replacing *ξ, i, j, k* with *η, j,i,k* or *ς, k, i, j* respectively.

Ideally, fastest convergence is obtained when the same method of differencing is used on both the RHS and LHS of Equation 2-23. While this is possible for low-order schemes since the block tridiagonal structure of the equations can be maintained, higher order schemes require larger difference stencils and would preclude the use of a block tridiagonal solver if used on the LHS. Hence Steger-Warming flux vector splitting is used on the LHS to evaluate the inviscid flux jacobians as defined by:

$$
\partial_\xi \tilde{A}_{i,j,k} = \tfrac{1}{\Delta\xi}\left[\left(\tilde{A}_{i,j,k}^{+} - \tilde{A}_{i-1,j,k}^{+}\right) + \left(\tilde{A}_{i+1,j,k}^{-} - \tilde{A}_{i,j,k}^{-}\right)\right]
\tag{2-39}
$$

The + and – superscripts in Equation 2-39 indicate contributions from downstream and upstream traveling characteristic waves (also referred to as fluxes) respectively and are given by:

$$\widetilde{A}^{\pm} = T_{\xi}\Lambda_{\xi}^{\pm}T_{\xi}^{-1} \tag{2-40}$$

In Equation 2-40, T_{ξ} and T_{ξ}^{-1} are the left and right eigenvectors respectively and are defined as:

$$T_{\xi} = \begin{bmatrix} \xi_x & \xi_y & \xi_z & T_1 & T_1 \\ u\xi_x & u\xi_y - \rho\xi_z & u\xi_z + \rho\xi_y & T_1(u + c\xi_x) & T_1(u - c\xi_x) \\ v\xi_x + \rho\xi_z & v\xi_y & v\xi_z - \rho\xi_x & T_1(v + c\xi_y) & T_1(v - c\xi_y) \\ w\xi_x + \rho\xi_y & w\xi_y + \rho\xi_x & w\xi_z & T_1(w + c\xi_z) & T_1(w - c\xi_z) \\ T_2\xi_x + \rho T_3 & T_2\xi_y + \rho T_4 & T_2\xi_z + \rho T_5 & T_1\left(T_2 + \dfrac{1}{T_6} + cT_7\right) & T_1\left(T_2 + \dfrac{1}{T_6} - cT_7\right) \end{bmatrix} \tag{2-41}$$

$$T_{\xi}^{-1} = \begin{bmatrix} \xi_x\left(1 - \frac{T_8}{c^2}\right) - \dfrac{T_3}{\rho} & \xi_x uT_6 & \xi_x vT_6 + \dfrac{\xi_z}{\rho} & \xi_x wT_6 - \dfrac{\xi_y}{\rho} & -\xi_x T_6 \\ \xi_y\left(1 - \frac{T_8}{c^2}\right) - \dfrac{T_4}{\rho} & \xi_y uT_6 - \dfrac{\xi_z}{\rho} & \xi_y vT_6 & \xi_y wT_6 + \dfrac{\xi_x}{\rho} & -\xi_y T_6 \\ \xi_z\left(1 - \frac{T_8}{c^2}\right) - \dfrac{T_5}{\rho} & \xi_z uT_6 + \dfrac{\xi_y}{\rho} & \xi_z vT_6 - \dfrac{\xi_x}{\rho} & \xi_z wT_6 & -\xi_z T_6 \\ T_9(T_8 - cT_7) & T_9c(\xi_x - ucT_6) & T_9c(\xi_y - vcT_6) & T_9c(\xi_z - wcT_6) & T_9(\gamma - 1) \\ T_9(T_8 + cT_7) & -T_9c(\xi_x + ucT_6) & -T_9c(\xi_y - vcT_6) & -T_9c(\xi_z - wcT_6) & T_9(\gamma - 1) \end{bmatrix} \tag{2-42}$$

where

$$T_1 = \frac{\rho}{c\sqrt{2}} \qquad T_2 = \frac{1}{2}\left(u^2 + v^2 + w^2\right)$$

$$T_3 = v\xi_z - w\xi_y \qquad T_4 = w\xi_x - u\xi_z \qquad T_5 = u\xi_y - v\xi_x \tag{2-43}$$

$$T_6 = \frac{\gamma - 1}{c^2} \qquad T_7 = \xi_x u + \xi_y v + \xi_z w \qquad T_8 = T_2(\gamma - 1) \qquad T_9 = \frac{1}{\rho c\sqrt{2}}$$

and $\Lambda_\xi^\pm$ is the Jacobian matrix of the corresponding eigenvalues:

$$\Lambda_\xi^\pm = \begin{bmatrix} \lambda_1^\pm & & & & \\ & \lambda_2^\pm & & & \\ & & \lambda_3^\pm & & \\ & & & \lambda_4^\pm & \\ & & & & \lambda_5^\pm \end{bmatrix} \tag{2-44}$$

where the eigenvalues are:

$$\lambda_{1,2,3} = \xi_t + \xi_x u + \xi_y v + \xi_z w$$

$$\lambda_4 = \lambda_1 + c\sqrt{\xi_x^2 + \xi_y^2 + \xi_z^2} \tag{2-45}$$

$$\lambda_5 = \lambda_1 - c\sqrt{\xi_x^2 + \xi_y^2 + \xi_z^2}$$

To obtain the downstream (+) and upstream (-) traveling characteristic fluxes from the eigenvalues given in Equation 2-45, the following formulation for splitting the fluxes is used in order to handle sonic lines, where the eigenvalues switch signs:

$$\lambda^\pm = \frac{\lambda \pm \sqrt{\lambda^2 + \varepsilon^2}}{2} \qquad \varepsilon = \frac{c\sqrt{\xi_x^2 + \xi_y^2 + \xi_z^2}}{2} \tag{2-46}$$

The other two inviscid flux jacobians, $\partial_\eta \tilde{B}$ and $\partial_\varsigma \tilde{C}$, are calculated by simply replacing *ξ, i, j, k* in Equations 2-39 through 2-46 with *η, j,i,k* or *ς, k, i, j* respectively.

For the viscid jacobian fluxes on the LHS, a simple second order central difference is applied:

$$\partial_{\xi}\tilde{A}_{i,j,k} = \tfrac{1}{\Delta\xi}\left(\overline{A}^{v}_{i+1,j,k} - 2\overline{A}^{v}_{i,j,k} + \overline{A}^{v}_{i-1,j,k}\right) \tag{2-47}$$

where the individual viscid terms are represented with a Taylor series linearization:

$$\overline{A}^{v} = \tfrac{1}{\Delta\xi}\begin{bmatrix} 0 & 0 & 0 & 0 & 0 \\ L_{21} & \dfrac{\alpha_1}{\rho} & \dfrac{\alpha_2}{\rho} & \dfrac{\alpha_3}{\rho} & 0 \\ L_{31} & \dfrac{\alpha_2}{\rho} & \dfrac{\alpha_4}{\rho} & \dfrac{\alpha_5}{\rho} & 0 \\ L_{41} & \dfrac{\alpha_3}{\rho} & \dfrac{\alpha_5}{\rho} & \dfrac{\alpha_6}{\rho} & 0 \\ L_{51} & L_{52} & L_{53} & L_{54} & \dfrac{\alpha_7}{\rho} \end{bmatrix} \tag{2-48}$$

and

$$\alpha_1 = \mu\left(\frac{4}{3}\xi_x^2 + \xi_y^2 + \xi_z^2\right) \qquad \alpha_2 = \frac{1}{3}\mu\xi_x\xi_y \qquad \alpha_3 = \frac{1}{3}\mu\xi_x\xi_z$$

$$\alpha_4 = \mu\left(\xi_x^2 + \frac{4}{3}\xi_y^2 + \xi_z^2\right) \qquad \alpha_5 = \frac{1}{3}\mu\xi_y\xi_z \qquad \alpha_6 = \mu\left(\xi_x^2 + \xi_y^2 + \frac{4}{3}\xi_z^2\right)$$

$$\alpha_7 = \gamma\mu \Pr^{-1}\left(\xi_x^2 + \xi_y^2 + \xi_z^2\right)$$

$$L_{21} = -\alpha_1\left(\frac{u}{\rho}\right) - \alpha_2\left(\frac{v}{\rho}\right) - \alpha_3\left(\frac{w}{\rho}\right) \qquad L_{52} = L_{21} - \alpha_7\left(\frac{u}{\rho}\right) \tag{2-49}$$

$$L_{31} = -\alpha_2\left(\frac{u}{\rho}\right) - \alpha_4\left(\frac{v}{\rho}\right) - \alpha_5\left(\frac{w}{\rho}\right) \qquad L_{53} = L_{31} - \alpha_7\left(\frac{v}{\rho}\right)$$

$$L_{41} = -\alpha_3\left(\frac{u}{\rho}\right) - \alpha_5\left(\frac{v}{\rho}\right) - \alpha_6\left(\frac{w}{\rho}\right) \qquad L_{54} = L_{41} - \alpha_7\left(\frac{w}{\rho}\right)$$

$$L_{51} = -2\left[\alpha_2\left(\frac{uv}{\rho}\right) + \alpha_3\left(\frac{uw}{\rho}\right) + \alpha_5\left(\frac{vw}{\rho}\right)\right] - \alpha_1\left(\frac{u^2}{\rho}\right) - \alpha_4\left(\frac{v^2}{\rho}\right) - \alpha_6\left(\frac{w^2}{\rho}\right)$$
$$+ \alpha_7\left(\frac{u^2 + v^2 + w^2 + e}{\rho}\right)$$

As with the inviscid flux jacobians, $\tilde{B}^v$ and $\tilde{C}^v$ are obtained by replacing *ξ, i, j, k* in Equations 2-47 through 2-49 by *η, j,i,k* or *ς, k, i, j* respectively.

Returning to Equation 2-23, the AF form of the Navier-Stokes equations is solved in a three stage ADI algorithm. The first of these stages is solved in the *ξ* direction (*ξ* sweep) for an intermediate solution $\Delta\overline{Q}^*$:

$$\left\{ I + \tfrac{1}{\Delta\xi}\begin{bmatrix} \tilde{A}^+_{i,j,k} - \tilde{A}^+_{i-1,j,k} + \tilde{A}^-_{i+1,j,k} - \tilde{A}^-_{i,j,k} \\ -\mathrm{Re}^{-1}\left(\overline{A}^v_{i+1,j,k} - 2\overline{A}^v_{i,j,k} + \overline{A}^v_{i-1,j,k}\right) \end{bmatrix} \right\} \Delta\overline{Q}^* = RHS_{i,j,k} \tag{2-50}$$

where

$$RHS_{i,j,k} = -\left\{ \tfrac{\Delta\tau'}{\Delta\tau}\left(\tfrac{3}{2}\tilde{Q}^{n+1,k} - 2\tilde{Q}^{n} + \tfrac{1}{2}\tilde{Q}^{n-1}\right) \right. \\ \left. + \partial_\xi \hat{E}^n + \partial_\eta \hat{F}^n + \partial_\varsigma \hat{G}^n - \mathrm{Re}^{-1}\left[\partial_\xi\left(\hat{E}^v_\xi\right)^n + \partial_\eta\left(\hat{F}^v_\eta\right)^n + \partial_\varsigma\left(\hat{G}^v_\varsigma\right)^n\right]\right\} \tag{2-51}$$

The second stage is solved in the η direction (η sweep) for a second intermediate solution $\Delta\overline{Q}^{**}$:

$$\left\{ I + \tfrac{1}{\Delta\eta}\begin{bmatrix} \tilde{B}^+_{i,j,k} - \tilde{B}^+_{i,j-1,k} + \tilde{B}^-_{i,j+1,k} - \tilde{B}^-_{i,j,k} \\ -\mathrm{Re}^{-1}\left(\overline{B}^v_{i,j+1,k} - 2\overline{B}^v_{i,j,k} + \overline{B}^v_{i,j-1,k}\right)\end{bmatrix}\right\}\Delta\overline{Q}^{**} = \Delta\overline{Q}^{*} \tag{2-52}$$

Finally, the third stage is solved in the ς direction (ς sweep):

$$\left\{ I + \tfrac{1}{\Delta\varsigma}\begin{bmatrix} \tilde{C}^+_{i,j,k} - \tilde{C}^+_{i,j,k-1} + \tilde{C}^-_{i,j,k+1} - \tilde{C}^-_{i,j,k} \\ -\mathrm{Re}^{-1}\left(\overline{C}^v_{i,j,k+1} - 2\overline{C}^v_{i,j,k} + \overline{C}^v_{i,j,k-1}\right)\end{bmatrix}\right\}\Delta\tilde{Q} = \Delta\overline{Q}^{**} \tag{2-53}$$

where the desired solution $\tilde{Q}^{n+1,k+1}$ is obtained via:

$$\Delta\tilde{Q} = \left(\tilde{Q}^{n+1,k+1} - \tilde{Q}^{n+1,k}\right) \quad \Rightarrow \quad \tilde{Q}^{n+1,k+1} = \tilde{Q}^{n+1,k} + \Delta\tilde{Q} \tag{2-54}$$

Equations 2-50 through 2-53 form a block tridiagonal coefficient matrix system, which is symmetric positive definite. To obtain this form, Equations 2-50 through 2-53 are first rearranged in terms of the grid index:

$$\left[-\tfrac{1}{\Delta\xi}\left(\tilde{A}^+_{i-1,j,k} + \mathrm{Re}^{-1}\,\overline{A}^v_{i-1,j,k}\right)\right]\Delta\overline{Q}^*_{i-1,j,k} + \left[I + \tfrac{1}{\Delta\xi}\left(\tilde{A}^+_{i,j,k} - \tilde{A}^-_{i,j,k} + 2\mathrm{Re}^{-1}\,\overline{A}^v_{i,j,k}\right)\right]\Delta\overline{Q}^*_{i,j,k} \\ + \left[\tfrac{1}{\Delta\xi}\left(\tilde{A}^-_{i+1,j,k} - \mathrm{Re}^{-1}\,\overline{A}^v_{i+1,j,k}\right)\right]\Delta\overline{Q}^*_{i+1,j,k} = RHS_{i,j,k} \tag{2-55}$$

$$\left[-\tfrac{1}{\Delta\eta}\left(\tilde{B}^+_{i,j-1,k} + \mathrm{Re}^{-1}\,\overline{B}^v_{i,j-1,k}\right)\right]\Delta\overline{Q}^{**}_{i,j-1,k} + \left[I + \tfrac{1}{\Delta\eta}\left(\tilde{B}^+_{i,j,k} - \tilde{B}^-_{i,j,k} + 2\mathrm{Re}^{-1}\,\overline{B}^v_{i,j,k}\right)\right]\Delta\overline{Q}^{**}_{i,j,k} \\ + \left[\tfrac{1}{\Delta\eta}\left(\tilde{B}^-_{i,j+1,k} - \mathrm{Re}^{-1}\,\overline{B}^v_{i,j+1,k}\right)\right]\Delta\overline{Q}^{**}_{i,j+1,k} = \Delta\overline{Q}^{*}_{i,j,k} \tag{2-56}$$

$$\left[-\tfrac{1}{\Delta\varsigma}\left(\tilde{C}^+_{i,j,k-1} + \mathrm{Re}^{-1}\,\overline{C}^v_{i,j,k-1}\right)\right]\Delta\tilde{Q}_{i,j,k-1} + \left[I + \tfrac{1}{\Delta\varsigma}\left(\tilde{C}^+_{i,j,k} - \tilde{C}^-_{i,j,k} + 2\mathrm{Re}^{-1}\,\overline{C}^v_{i,j,k}\right)\right]\Delta\tilde{Q}_{i,j,k} \\ + \left[\tfrac{1}{\Delta\varsigma}\left(\tilde{C}^-_{i,j,k+1} - \mathrm{Re}^{-1}\,\overline{C}^v_{i,j,k+1}\right)\right]\Delta\tilde{Q}_{i,j,k+1} = \Delta\overline{Q}^{**}_{i+1,j,k} \tag{2-57}$$

Redefining the terms in Equations 2-55 through 2-57 as:

$$
\begin{aligned}
CAM &= -\tfrac{1}{\Delta\xi}\left(\tilde{A}^{+}_{i-1,j,k} + \mathrm{Re}^{-1}\,\overline{A}^{v}_{i-1,j,k}\right)\\
CA &= I + \tfrac{1}{\Delta\xi}\left(\tilde{A}^{+}_{i,j,k} - \tilde{A}^{-}_{i,j,k} + 2\,\mathrm{Re}^{-1}\,\overline{A}^{v}_{i,j,k}\right)\\
CAP &= \tfrac{1}{\Delta\xi}\left(\tilde{A}^{-}_{i+1,j,k} - \mathrm{Re}^{-1}\,\overline{A}^{v}_{i+1,j,k}\right)
\end{aligned}
\tag{2-58}
$$

$$
\begin{aligned}
CBM &= -\tfrac{1}{\Delta\eta}\left(\tilde{B}^{+}_{i,j-1,k} + \mathrm{Re}^{-1}\,\overline{B}^{v}_{i,j-1,k}\right)\\
CB &= I + \tfrac{1}{\Delta\eta}\left(\tilde{B}^{+}_{i,j,k} - \tilde{B}^{-}_{i,j,k} + 2\,\mathrm{Re}^{-1}\,\overline{B}^{v}_{i,j,k}\right)\\
CBP &= \tfrac{1}{\Delta\eta}\left(\tilde{B}^{-}_{i,j+1,k} - \mathrm{Re}^{-1}\,\overline{B}^{v}_{i,j+1,k}\right)
\end{aligned}
\tag{2-59}
$$

$$
\begin{aligned}
CCM &= -\tfrac{1}{\Delta\varsigma}\left(\tilde{C}^{+}_{i,j,k-1} + \mathrm{Re}^{-1}\,\overline{C}^{v}_{i,j,k-1}\right)\\
CC &= I + \tfrac{1}{\Delta\varsigma}\left(\tilde{C}^{+}_{i,j,k} - \tilde{C}^{-}_{i,j,k} + 2\,\mathrm{Re}^{-1}\,\overline{C}^{v}_{i,j,k}\right)\\
CCP &= \tfrac{1}{\Delta\varsigma}\left(\tilde{C}^{-}_{i,j,k+1} - \mathrm{Re}^{-1}\,\overline{C}^{v}_{i,j,k+1}\right)
\end{aligned}
\tag{2-60}
$$

Equations 2-55 through 2-57 become:

$$CAM_{i,j,k}\,\Delta\overline{Q}^{*}_{i-1,j,k} + CA_{i,j,k}\,\Delta\overline{Q}^{*}_{i,j,k} + CAP_{i,j,k}\,\Delta\overline{Q}^{*}_{i+1,j,k} = RHS_{i,j,k} \tag{2-61}$$

$$CBM_{i,j,k}\,\Delta\overline{Q}^{**}_{i,j-1,k} + CB_{i,j,k}\,\Delta\overline{Q}^{**}_{i,j,k} + CBP_{i,j,k}\,\Delta\overline{Q}^{**}_{i,j+1,k} = \Delta\overline{Q}^{*}_{i,j,k} \tag{2-62}$$

$$CCM_{i,j,k}\,\Delta\tilde{Q}_{i,j,k-1} + CC_{i,j,k}\,\Delta\tilde{Q}_{i,j,k} + CCP_{i,j,k}\Delta\tilde{Q}_{i,j,k+1} = \Delta\overline{Q}^{**}_{i+1,j,k} \tag{2-63}$$

Now putting these in a block tridiagonal format, the following is obtained for the ξ sweep:

$$
\begin{bmatrix}
CA_{1,j,k} & CAP_{1,j,k} & & & \\
CAM_{2,j,k} & CA_{2,j,k} & CAP_{2,j,k} & & \\
& \ddots & \ddots & \ddots & \\
& & CAM_{IM-1,j,k} & CA_{IM-1,j,k} & CAP_{IM-1,j,k}\\
& & & CAM_{IM,j,k} & CA_{IM,j,k}
\end{bmatrix}
\begin{bmatrix}
\Delta\overline{Q}^{*}_{1,j,k}\\
\Delta\overline{Q}^{*}_{2,j,k}\\
\vdots\\
\Delta\overline{Q}^{*}_{IM-1,j,k}\\
\Delta\overline{Q}^{*}_{IM,j,k}
\end{bmatrix}
=
\begin{bmatrix}
RHS_{1,j,k}\\
RHS_{2,j,k}\\
\vdots\\
RHS_{IM-1,j,k}\\
RHS_{IM,j,k}
\end{bmatrix}
\tag{2-64}
$$

then for the η sweep:

$$\begin{bmatrix} CB_{i,1,k} & CBP_{i,1,k} & & & \\ CBM_{i,2,k} & CB_{i,2,k} & CBP_{i,2,k} & & \\ & \ddots & \ddots & \ddots & \\ & & CBM_{i,JM-1,k} & CB_{i,JM-1,k} & CBP_{i,JM-1,k} \\ & & & CBM_{i,JM,k} & CB_{i,JM,k} \end{bmatrix} \begin{bmatrix} \Delta\overline{Q}^{**}_{i,1,k} \\ \Delta\overline{Q}^{**}_{i,2,k} \\ \vdots \\ \Delta\overline{Q}^{**}_{i,JM-1,k} \\ \Delta\overline{Q}^{**}_{i,JM,k} \end{bmatrix} = \begin{bmatrix} \Delta\overline{Q}^{*}_{i,1,k} \\ \Delta\overline{Q}^{*}_{i,2,k} \\ \vdots \\ \Delta\overline{Q}^{*}_{i,JM-1,k} \\ \Delta\overline{Q}^{*}_{i,JM,k} \end{bmatrix} \tag{2-65}$$

and finally for the ς sweep:

$$\begin{bmatrix} CC_{i,j,1} & CCP_{i,j,1} & & & \\ CCM_{i,j,2} & CC_{i,j,2} & CCP_{i,j,2} & & \\ & \ddots & \ddots & \ddots & \\ & & CCM_{i,j,KM-1} & CC_{i,j,KM-1} & CCP_{i,j,KM-1} \\ & & & CCM_{i,j,KM} & CC_{i,j,KM} \end{bmatrix} \begin{bmatrix} \Delta\tilde{Q}_{i,j,1} \\ \Delta\tilde{Q}_{i,j,2} \\ \vdots \\ \Delta\tilde{Q}_{i,j,KM-1} \\ \Delta\tilde{Q}_{i,j,KM} \end{bmatrix} = \begin{bmatrix} \Delta\overline{Q}^{**}_{i,j,1} \\ \Delta\overline{Q}^{**}_{i,j,2} \\ \vdots \\ \Delta\overline{Q}^{**}_{i,j,KM-1} \\ \Delta\overline{Q}^{**}_{i,j,KM} \end{bmatrix} \tag{2-66}$$

In Equations 2-64 through 2-66, *IM*, *JM*, *KM* represent the last *i*, *j*, and *k* index in the computational grid. For each sweep, the block tridiagonal system is solved using a LU decomposition method, which is outlined in Appendix A.

Unlike many other CFD models, Corsair is a fully unsteady flow solver and does not have a steady state capability for multi blade row simulations. This has the disadvantage of requiring the use of very small initial time steps in order to handle start-up transients. Solutions are started by ramping up to this small time step and thus wheel speed over a user specified number of iterations. Once the ramping is complete, the time step is gradually increased by decreasing the number of iterations per cycle. To facilitate this tricky procedure, Corsair re-reads the input deck every time a number of pre-specified iterations have been completed. The number of iterations per cycle is adjusted according to the residual dumped in the output file after each iteration.

2.3 Boundary Conditions

One of the most important factors determining the success or failure of a numerical simulation is the boundary conditions. The boundary conditions used in Corsair can be broadly classified as either natural boundaries or zonal boundaries [40,41]. Both types of boundaries are handled in a two step method, comprised of an implicit formulation during pseudo time steps followed by enforcement of the boundary condition via a post iterative update after each physical time step. The natural boundaries include the axial inlet and exit along with the hub, outer casing, and airfoil surfaces. Zonal boundaries comprise the patch and overlay boundaries, including the slip boundary between adjacent blade rows, the circumferential periodic boundary between adjacent passages in the same blade row, the Chimera boundary between O-grids and H-grids, and the continuity condition between the O-grid and clearance grid. A brief description of each boundary condition is now given along with its numerical implementation in Corsair.

To apply the implicit portion of the axial inlet boundary condition, the first row of blocks from equation 2-64 are set as:

$$\begin{aligned} RHS_{1,j,k} &= 0 \\ CA_{1,j,k} &= C \cdot I \\ CAP_{1,j,k} &= -C\left({J_{2,j,k}}\big/{J_{1,j,k}} \right) \cdot I \end{aligned} \qquad (2\text{-}68)$$

Where C is the Courant number (specified in the input deck and allows control of stability vs. convergence speed), I is the identity matrix, and J is the Jacobian matrix of coordinate transformation. The post iterative update depends on whether the axial inlet flow is subsonic or supersonic. If supersonic, then all flow quantities are set to their free stream values. If the axial inlet flow is subsonic, however, four quantities are specified with the fifth being the Riemann invariant. A few different combinations are available for these four quantities as given in Table 2-2.

BC 1	BC 2	BC 3	BC 4	BC 5
$S = S_\infty$	$P_t = P_{t\infty}$	$S = S_\infty$	$P_t = P_{t\infty}$	$P_t = P_{t\infty}$
$v = v_\infty$	$v = v_\infty$	$v = u \cdot \tan\alpha$	$v = u \cdot \tan\alpha$	$T_t = T_{t\infty}$
$w = w_\infty$	$w = w_\infty$	$w = u/(\tan\beta \cdot \cos\alpha)$	$w = u/(\tan\beta \cdot \cos\alpha)$	$v = u \cdot \tan\alpha$
$R_1 = u + 2c/\gamma - 1$	$R_1 = u + 2c/\gamma - 1$	$R_1 = u + 2c/\gamma - 1$	$R_1 = u + 2c/\gamma - 1$	$w = u/(\tan\beta \cdot \cos\alpha)$
$R_2 = u - 2c/\gamma - 1$	$R_2 = u - 2c/\gamma - 1$	$R_2 = u - 2c/\gamma - 1$	$R_2 = u - 2c/\gamma - 1$	$R = u - 2c/\gamma - 1$

Table 2-2. List of axial inlet boundary conditions

Where S is entropy; u, v, and w the axial, circumferential, and radial velocities respectively; R the Riemann invariants; P_t and T_t the total pressure and total temperature; c the local speed of sound; γ the ratio of specific heats; α and β the flow pitch and yaw angles respectively; and the subscript ∞ refers to the inlet free stream values.

Similarly, the implicit portion of the axial exit boundary condition involves setting the last row of blocks from Equation 2-64 as:

$$RHS_{IM,j,k} = 0$$
$$CA_{IM,j,k} = C \cdot I \qquad (2\text{-}69)$$
$$CAM_{IM,j,k} = -C\left(J_{IM-1,j,k} / J_{IM,j,k} \right) \cdot I$$

As with the axial inlet boundary, the post iterative update depends on whether the axial exit flow is subsonic or supersonic. If it's supersonic, then all flow quantities are extrapolated from the interior domain. If the axial exit flow is subsonic however, a constant pressure is imposed at midspan with the pressure at other spans prescribed by the radial equilibrium condition:

$$\frac{\partial P}{\partial r} = \frac{\rho v_t^2}{r} \tag{2-70}$$

This results in quasi-2d equilibrium flow, where *P* is the spanwise pressure, v_t is the tangential or axial velocity, and *r* is the radius from the center of the hub. To obtain the remaining quantities, the circumferential and radial velocities, along with entropy and the Riemann invariant are extrapolated from upstream.

For surfaces, including the hub, outer casing, and airfoil, three different types of boundary conditions exist; slip (Euler condition), no slip with specified heat flux, or no slip with specified surface temperature. The implicit portion of the slip condition involves setting the associated RHS and off-diagonal block to zero and the associated diagonal block to the identity matrix. As an example, consider the hub surface which becomes a boundary in the zeta sweep:

$$\begin{aligned} \Delta\overline{Q}^{**}_{i,j,1} &= 0 \\ CC_{i,j,1} &= 0 \\ CCP_{i,j,1} &= I \end{aligned} \tag{2-71}$$

The post iterative update enforces the tangency condition along the surface by setting the normal contravariant velocity to zero. For reference, the contravariant velocities are simply those defined in the curvilinear coordinate system and may be written using the coordinate transformation metrics:

$$U = \xi_t + \xi_x u + \xi_y v + \xi_z w$$

$$V = \eta_t + \eta_x u + \eta_y v + \eta_z w \qquad (2\text{-}72)$$

$$W = \zeta_t + \zeta_x u + \zeta_y v + \zeta_z w$$

Continuing along with the example of the post iterative update at the hub, the contra-variant velocity normal to the hub, *W*, is set to zero and the Cartesian velocities *u*, *v*, and *w* are solved using:

$$\begin{bmatrix} u \\ v \\ w \end{bmatrix} = J^{-1} \begin{bmatrix} (\eta_x\zeta_z - \eta_z\zeta_y) & -(\xi_y\zeta_z - \xi_z\zeta_y) & (\xi_y\eta_z - \eta_y\xi_z) \\ -(\eta_x\zeta_z - \eta_z\zeta_x) & (\xi_x\zeta_z - \xi_z\zeta_y) & -(\xi_x\eta_z - \xi_z\eta_x) \\ (\eta_x\zeta_y - \eta_y\zeta_x) & -(\xi_x\zeta_y - \xi_y\zeta_x) & (\xi_x\eta_y - \xi_y\eta_x) \end{bmatrix} \begin{bmatrix} U - \xi_t \\ V - \eta_t \\ W - \zeta_t \end{bmatrix} \qquad (2\text{-}73)$$

The pressure and density at the surface are taken to be the same as at the first grid point above the surface, from which the remaining conservative variables are easily calculated.

As stated earlier, the viscous no slip boundary conditions come in two forms, one involves specifying a heat flux at the surface while the other requires specifying the temperature of the surface. The implicit portions of these boundary conditions are very similar and will be discussed together. To begin, the RHS block of the associated boundary is set to zero and the associated diagonal block is defined as:

$$\begin{bmatrix} \alpha & 0 & 0 & 0 & 0 \\ 0 & C & 0 & 0 & 0 \\ 0 & 0 & C & 0 & 0 \\ 0 & 0 & 0 & C & 0 \\ C \cdot \left(u_{wall}^2 + v_{wall}^2 + w_{wall}^2\right) & -C \cdot u_{wall} & -C \cdot v_{wall} & -C \cdot w_{wall} & C \end{bmatrix} \qquad (2\text{-}74)$$

Where C is the courant number and u_{wall}, v_{wall}, and w_{wall} are the velocities at the surface in Cartesian coordinates. For a specified temperature at the surface, α is simply set to the courant number, while for a specified heat flux at the surface it is defined as:

$$\alpha = C*(1+\partial T/(T_{wall}\cdot k)) \tag{2-75}$$

Where ∂T is the specified heat flux at the surface, T_{wall} is the surface temperature, and k is the thermal conductivity of the flow over the surface. The associate off diagonal block is defined as:

$$J_{wall+1}\big/J_{wall}\begin{bmatrix} \beta_1 & \beta_2 & \beta_3 & \beta_4 & \beta_5 \\ 0 & 0 & 0 & 0 & 0 \\ 0 & 0 & 0 & 0 & 0 \\ 0 & 0 & 0 & 0 & 0 \\ \left(u_{wall}^2+v_{wall}^2+w_{wall}^2\right) & -u_{wall} & -v_{wall} & -w_{wall} & 1 \end{bmatrix} \tag{2-76}$$

For the case of a specified heat flux, $\beta_1 = 1$ and $\beta_2 = \beta_3 = \beta_4 = \beta_5 = 0$. If the temperature at the surface is specified instead:

$$\begin{aligned} \beta_1 &= \tfrac{1}{2}(u_{wall+1}^2+v_{wall+1}^2+w_{wall+1}^2)/(c_v T_{wall}) \\ \beta_2 &= u_{wall+1}/(c_v T_{wall}) \\ \beta_3 &= v_{wall+1}/(c_v T_{wall}) \\ \beta_4 &= w_{wall+1}/(c_v T_{wall}) \\ \beta_5 &= 1/(c_v T_{wall}) \end{aligned} \tag{2-77}$$

Where the subscript *wall+1* denotes values at the grid point just above the surface, c_v is the specific heat at constant volume, and T_{wall} is the specified temperature of the surface. The post iterative update involves calculating density at the surface based on the temperature at the surface:

$$\rho_{wall} = \frac{P_{wall+1}}{R\cdot T_{wall}} \tag{2-78}$$

The pressure at the surface is taken to be the same as the grid point just above the surface, thus allowing total energy at the surface to be easily calculated. For the case where heat flux at the surface is specified, the temperature at the wall is approximated as:

$$T_{wall} = T_{wall+1} + ds \cdot \left(\partial T / k \right) \qquad (2\text{-}79)$$

Where *ds* is the distance between the surface and the first grid point above the surface.

The slip boundary between adjacent blade rows begins with the generation of the H-grids for the blade rows themselves. When initially generated, the downstream boundary of the upstream row grid corresponds to the upstream boundary of the downstream row grid. The upstream row grid is then extended downstream by two axial grid locations such that they match the first two upstream axial grid locations from the downstream row grid. Finally, the downstream row grid is extended upstream by two axial grid locations in the same fashion. This process is illustrated for a 2D radial slice in Figure 2-2.

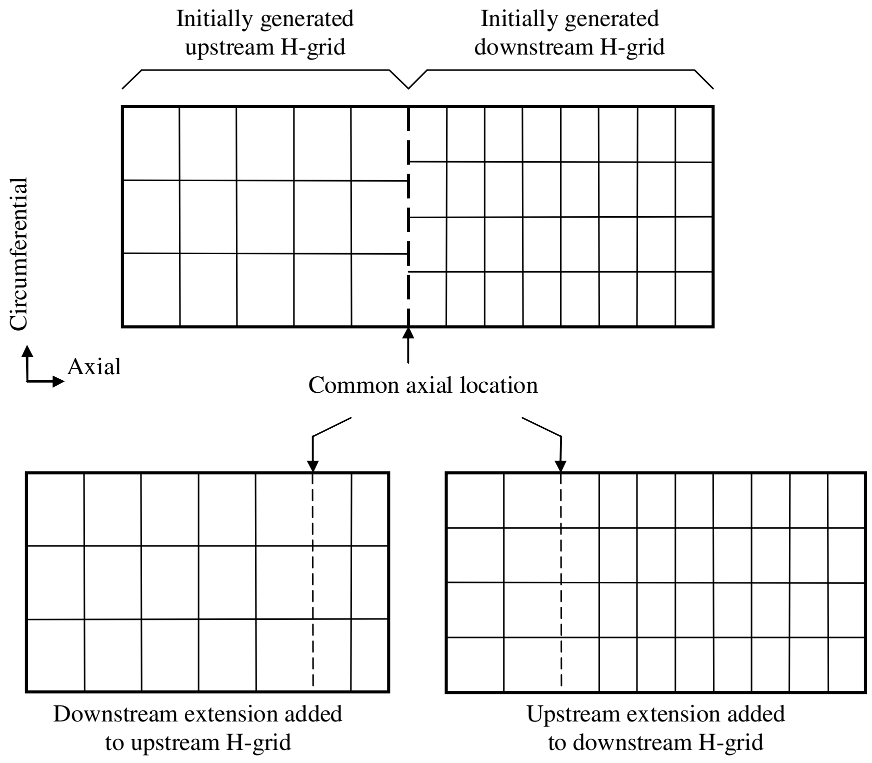
Initially generated upstream H-grid
Initially generated downstream H-grid
Circumferential
Axial
Common axial location
Downstream extension added to upstream H-grid
Upstream extension added to downstream H-grid

Figure 2-2. Generation of grid extensions for slip boundary condition

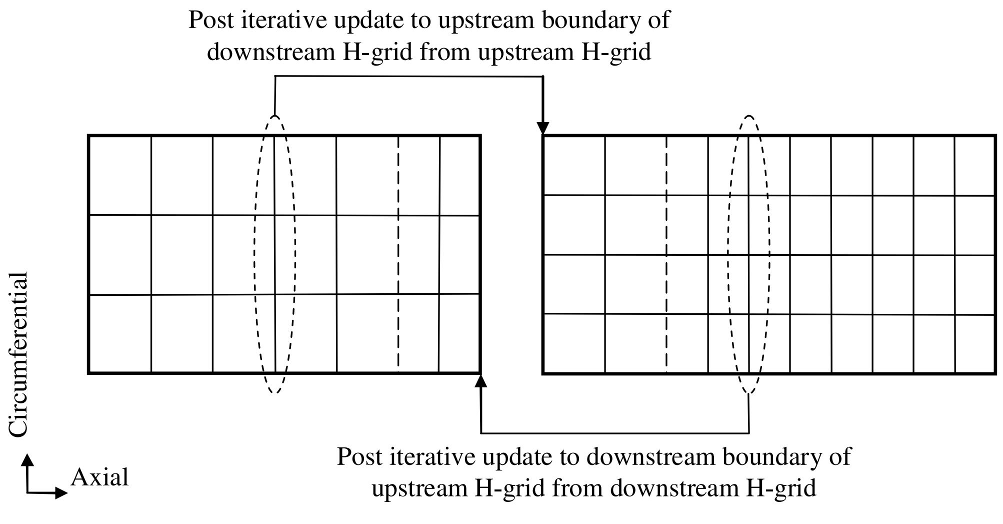
Post iterative update to upstream boundary of downstream H-grid from upstream H-grid
Circumferential
Axial
Post iterative update to downstream boundary of upstream H-grid from downstream H-grid

Figure 2-3. Post iterative update for slip boundary condition

The implicit portion of the slip boundary is applied as a dirichlet condition by setting the associated RHS and off diagonal blocks to zero and the diagonal block to the identity matrix. The post iterative update consists of setting values on the boundary to those of the associated overlap grid locations as illustrated in Figure 2-3. The reason for extending the grid overlap between adjacent blade rows by two grid locations rather than by a single location is to ensure the boundary conditions do not interfere with one another and produce spurious numerical oscillations. When the number of circumferential locations is different between the upstream and downstream H-grids (as shown in the illustrations), simple linear interpolation is used to obtain the value from the closest two circumferential grid locations. This same linear interpolation with simple periodicity is also used for cases when blade rows are rotating relative to one other. For such cases, the circumferential and radial Cartesian velocities are first transformed into tangential and normal velocities which are used for the interpolation, after which the circumferential and radial Cartesian velocities are recovered based on the circumferential angle of the point being interpolated.

The circumferential periodic boundary condition between adjacent passages in the same blade row employs an integrated implicit portion. This results in no modification of the RHS or coefficient matrix blocks. Instead, all values calculated on the boundary use quantities from ghost points created by the periodic condition, including the metrics of coordinate transformation. Figure 2-4 illustrates the periodic condition along with the ghost points for a 2D radial slice. In Figure 2-4, dashed lines show the cells formed by the ghost points and the arrows indicate where values for the ghost points are taken from.

Similarly, the post iterative update is based on the periodic condition as well, but is enforced at the boundary instead of the ghost points, as illustrated in Figure 2-5.

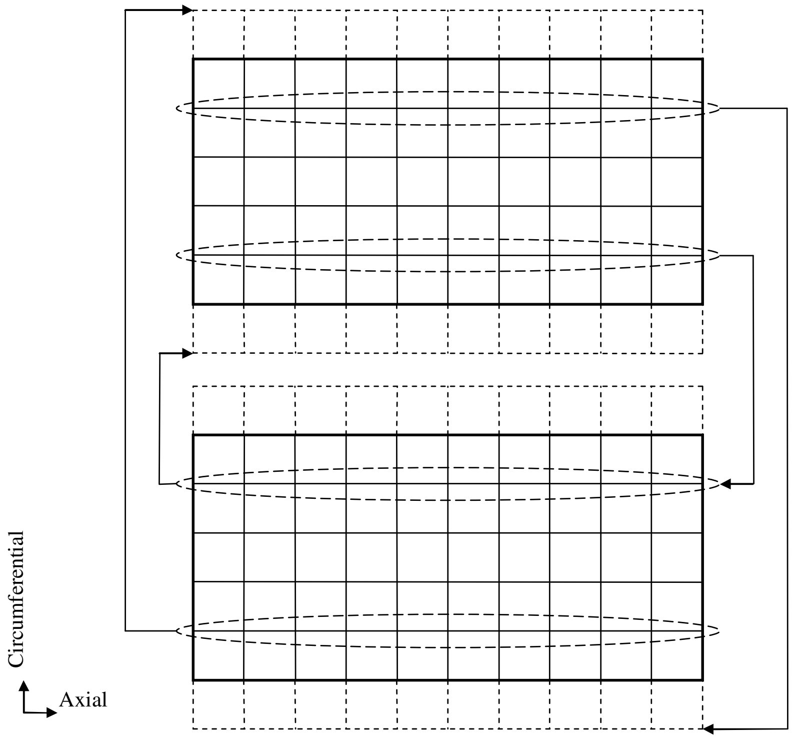

Figure 2-4. Illustration of circumferential periodic condition and ghost points

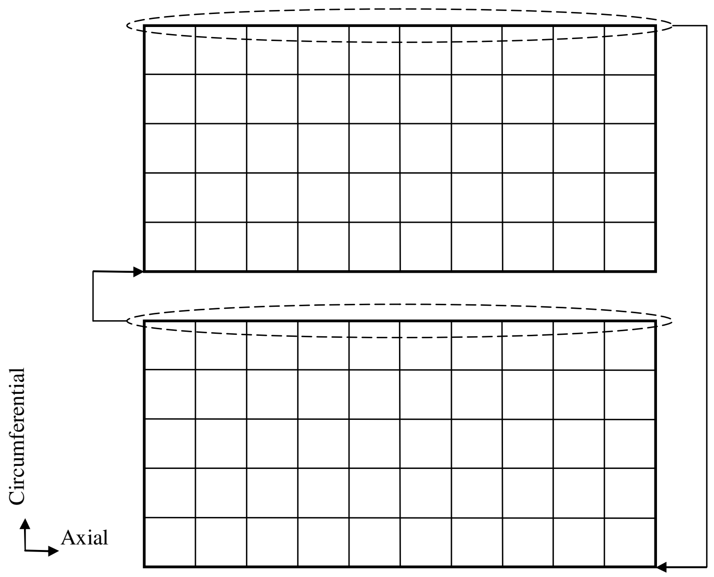

Figure 2-5. Post iterative update of circumferential periodic boundary

The Chimera patch boundary condition between an O-grid and H-grid on which it is overlaid, uses a dirichlet condition for the implicit portion. This is similar to what is done for the axial slip boundary, except in addition to points on the boundary, points cut from the interior of the H-grid to accommodate the O-grid are also "zeroed out" by setting their associated RHS and off diagonal blocks to zero along with their diagonal block to the identity matrix. To apply the post iterative update, values at the boundary are interpolated from the overlapping grid using shape functions. The shape functions are not only used for weighting the surrounding values for the interpolation, but also serve to determine if a point being interpolated lies in the triangle formed by three points from the overlapping grid. As an example, take the small section of the overlap between an H-grid and O-grid for a 2D radial slice as illustrated in Figure 2-6.

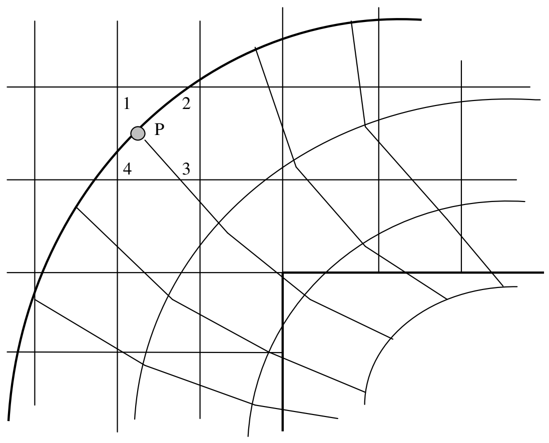

Figure 2-6. Section of overlap region between an O-grid and H-grid

In Figure 2-6, point P is on the boundary of the O-grid and for the post iteration update the conservative variables at point P are interpolated from the portion of the H-grid which encloses it, namely points 1 – 4. Figure 2-7 is a simplified illustration of this and includes the location of the shape functions (N_1-N_6) which will be calculated, first to determine which triangular half encloses point P and second to interpolate the values at point P by weighting the contribution from each of the points in the triangular half determined to enclosed point P. The reason for splitting the box which encloses point P into two triangles is because the shape functions for a triangle can be calculated using global coordinates. By contrast, the shape functions for a box require the use of local coordinates based about the centroid of the box.

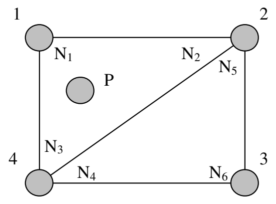

Figure 2-7. Simplified view of overlap region between O-grid and H-grid

The shape functions for the case illustrated in Figure 2-7 are as follows:

$$
\begin{aligned}
N_1 &= \frac{1}{2A_1}\left[(x_2yz_4 - x_4yz_2) + (yz_2 - yz_4)x_p + (x_4 - x_2)yz_p\right] \\
N_2 &= \frac{1}{2A_1}\left[(x_4yz_1 - x_1yz_4) + (yz_4 - yz_1)x_p + (x_1 - x_4)yz_p\right] \\
N_3 &= \frac{1}{2A_1}\left[(x_1yz_2 - x_2yz_1) + (yz_1 - yz_2)x_p + (x_2 - x_1)yz_p\right] \\
N_4 &= \frac{1}{2A_2}\left[(x_3yz_4 - x_4yz_3) + (yz_3 - yz_4)x_p + (x_4 - x_3)yz_p\right] \\
N_5 &= \frac{1}{2A_2}\left[(x_4yz_2 - x_2yz_4) + (yz_4 - yz_2)x_p + (x_2 - x_4)yz_p\right] \\
N_6 &= \frac{1}{2A_2}\left[(x_2yz_3 - x_3yz_2) + (yz_2 - yz_3)x_p + (x_3 - x_2)yz_p\right] \\
A_1 &= \frac{1}{2}(x_1yz_2 + x_2yz_3 + x_3yz_1 - x_1yz_3 - x_2yz_1 - x_3yz_2) \\
A_2 &= \frac{1}{2}(x_2yz_3 + x_3yz_4 + x_4yz_2 - x_2yz_4 - x_3yz_2 - x_4yz_3) \\
yz &= \sqrt{y^2 + z^2}\,\tan^{-1}\left(\frac{y}{z}\right)
\end{aligned}
\tag{2-80}
$$

Where A_1 and A_2 are the areas of the two triangles formed by points 1 2 4 and 2 3 4 respectively, and yz is the equivalent arc length at a fixed radius. All three shape functions for the triangle which contains point P will have a value between 1 and 0. If the triangle doesn't enclose point P, at least one of the shape functions will have a value outside this range. In Corsair, a simple brute force search is used to determine the triangle to use for interpolating the values at each of the boundary points. However, the shape functions give more information than just whether a point lies in or outside the triangle formed by them, it also indicates which direction point P lies if it's outside the triangle. This idea is elaborated in Appendix B and used to speed up the search of interpolation points, particularly when the O-grid and H-grid are moving relative to one another. Given the three shape functions for the triangle in which point P lies (N_1 N_2 N_3 in this case), the values at point P are interpolated via:

$$\varphi_p = N_1 \cdot \varphi_1 + N_2 \cdot \varphi_2 + N_4 \cdot \varphi_4 \tag{2-81}$$

Where φ represents the five conservative flow variables and the subscripts denote the point location of the variable.

When a clearance grid is used, boundary conditions are not only needed to enforce continuity between the O-grid and clearance grid but also at the collapsed centerline of the clearance grid. Both of these conditions arise in the eta sweep of the clearance grid, with no modifications required to the solution of the O-grid. These boundary conditions begin with the generation of the clearance grid, which is extended by one constant eta "ring" such that the outer two rings of the clearance grid coincide with the two inner most rings of the O-grid. Figure 2-8 illustrates this overlap of the constant eta "rings" between the O-grid and clearance grid.

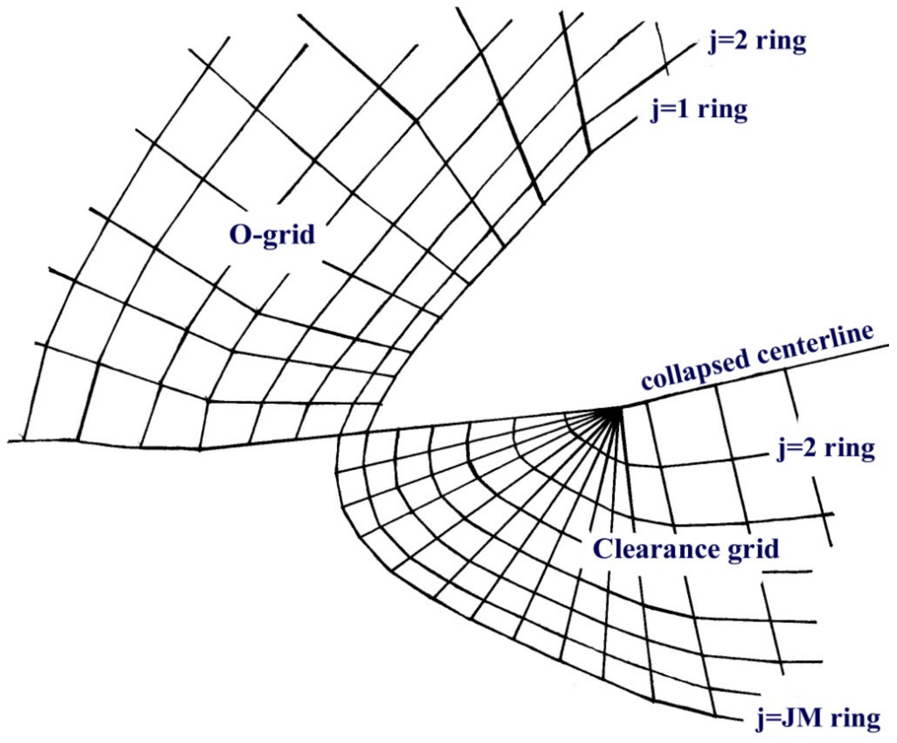

Figure 2-8. Illustration of overlap between an O-grid and clearance grid

The implicit portion of these boundary conditions involves using 10 ghost points in the eta direction from the O-grid to extend the calculation of the clearance grid well into the O-grid region. The primary reason for this is stability, since the number of constant eta "rings" is often very small, especially for thin airfoils. Next the RHS and off diagonal blocks for the first and last locations (i.e. *j=1* and *j=JM+10*) are set to zero while the associated diagonal block for these two locations is set to the identity matrix. After solving the block tri-diagonal matrix, only values for the original clearance grid are updated. Due to the eta extension into the O-grid, no post iterative update is needed at the O-grid clearance grid interface. However, a post iterative update is required at the collapsing centerline of the clearance grid to maintain continuity of the flow. This post iterative update involves interpolating values at the collapsed centerline from the opposite j=2 constant eta “ring”, as illustrated in Figure 2-9. The interpolation is a simple linear one based on axial locations.

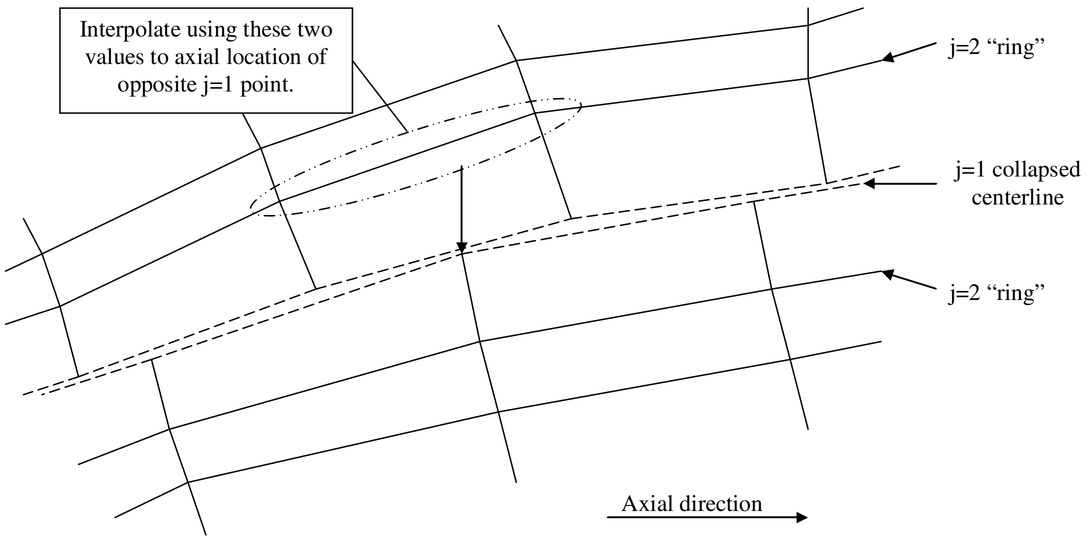
Interpolate using these two values to axial location of opposite j=1 point.
j=2 “ring”
j=1 collapsed centerline
j=2 “ring”
Axial direction

Figure 2-9. Post iterative update of clearance grid collapsing centerline

In this chapter, a detailed discussion of the solution method employed by Corsair has been covered. An overset O-H grid topology based on curvilinear coordinates is used upon which to solve the equations of motion on. The equations of motion are derived from the three dimensional Navier-Stokes equations with a dual (or pseudo) time step to improve convergence. After non-dimensionalization, the three dimensionally coupled equations of motion are split into three one dimensional equations using an Approximate Factorization. This results in a set of one dimensional equations with an explicit RHS and an implicit LHS, which are then solved in succession along each curvilinear coordinate using an Alternating Diagonal Implicit algorithm. In addition, a brief discussion of the boundary conditions available in Corsair was given.

3. NUMERICAL EVALUATION OF COORDINATE TRANSFORMATION METRICS

As covered in the previous chapter, Corsair uses a body-fitted curvilinear coordinate system to help generalize the equations of motion. To convert between these curvilinear coordinates and actual spatial coordinates, a mapping in the form of coordinate transformation metrics is used. While mathematical formula for these metrics was given in the previous chapter, the actual numerical evaluation of these transformations is a bit different and, as will be shown, more than one method for their evaluation exists in the open literature. Additionally, the numerical evaluation of the temporal metrics in the version of Corsair distributed by NASA is incomplete; it is based on an assumption of only rigid fluid grid rotation about the axial centerline. The deforming fluid grids ultimately arising from the FSI module require a complete implementation of the temporal metrics. Thus, this chapter explores several methods in the open literature for the numerical evaluation of both spatial and temporal metrics, including comparisons of their performance when implemented in Corsair, with the best method being used for the remainder of this research.

The use of higher order finite difference schemes to solve non-trivial 3D geometries demands that issues of free-stream preservation and metric cancellation be carefully addressed. Such errors, which arise in the finite difference discretization of the governing equations when written in the conservative form, can catastrophically degrade the fidelity of second and higher order approaches [42,43]. By deriving the equations of motion in conservative form, the following identities have been implicitly invoked:

$$I_1 = (\xi_x / J)_\xi + (\eta_x / J)_\eta + (\zeta_x / J)_\zeta = 0 \tag{3-1}$$

$$I_2 = (\xi_y / J)_\xi + (\eta_y / J)_\eta + (\zeta_y / J)_\zeta = 0 \tag{3-2}$$

$$I_1 = (\xi_z / J)_\xi + (\eta_z / J)_\eta + (\zeta_z / J)_\zeta = 0 \tag{3-3}$$

$$I_4 = (1 / J)_\tau + (\xi_t / J)_\xi + (\eta_t / J)_\eta + (\zeta_t / J)_\zeta = 0 \tag{3-4}$$

The first three identities constitute a differential statement of surface conservation for a closed cell, while the fourth identity expresses volume conservation and is often referred to in the literature as the Geometric Conservation Law (GCL). While the definitions for the coordinate transformation metrics given in Equation 2-18 were sufficient to derive the equations of motions for body fitted curvilinear coordinates, they fail to satisfy these metric identities due to the lack of metric cancellation, resulting in grid induced errors for regions of large variation and near singularities. Two main methods have been introduced in the CFD community for enforcing these metric identities for higher order finite difference schemes.

3.1 Recasting in Conservative Form

Thomas and Lombard [44] proposed recasting the coordinate transformation metric equations in a "conservative" form prior to discretization:

$$
\begin{array}{lll}
\xi_x = J\left[(y_\eta z)_\zeta - (y_\zeta z)_\eta\right] & \xi_y = J\left[(z_\eta x)_\zeta - (z_\zeta x)_\eta\right] & \xi_z = J\left[(x_\eta y)_\zeta - (x_\zeta y)_\eta\right] \\
\eta_x = J\left[(y_\zeta z)_\xi - (y_\xi z)_\zeta\right] & \eta_y = J\left[(z_\zeta x)_\xi - (z_\xi x)_\zeta\right] & \eta_z = J\left[(x_\zeta y)_\xi - (x_\xi y)_\zeta\right] \\
\zeta_x = J\left[(y_\xi z)_\eta - (y_\eta z)_\xi\right] & \zeta_y = J\left[(z_\xi x)_\eta - (z_\eta x)_\xi\right] & \zeta_z = J\left[(x_\xi y)_\eta - (x_\eta y)_\xi\right]
\end{array}
\qquad (3\text{-}5)
$$

When the transformation metrics are recast in this manner and the derivatives are evaluated with the same high-order formulas employed for the fluxes, free-stream preservation is recovered in general time-invariant 3D curvilinear geometries [45].

For deforming and moving grids, identity I_4 must also be satisfied to eliminate metric cancellation errors and to ensure free-stream preservation. As distributed, Corsair does not take this into account since the only rigid grid motion around the axial centerline of the geometry is used and thus there is no grid deformation. However, since the FSI module being linked to Corsair will introduce both grid deformation and grid motion other than around the axial centerline, the physical time step derivative in Equation 2-16 is split using the chain rule of differentiation as follows:

$$
\tilde{Q}_\tau = (Q/J)_\tau = (1/J)\cdot Q_\tau + Q\cdot(1/J)_\tau \qquad (3\text{-}6)
$$

The reason for applying this only to the physical time step is that all grid point locations are held fixed during the pseudo time step. To incorporate this modification into Corsair, the time derivative of the inverse Jacobian is calculated at the beginning of each physical time step and simply combined with the RHS. Instead of attempting to compute the time derivative of the inverse Jacobian directly from the grid coordinates at various time levels (either analytically or numerically), the GCL identity I_4 is invoked to evaluate $(1/J)_\tau$:

$$(1/J)_\tau = \left[(\xi_t/J)_\xi + (\eta_t/J)_\eta + (\zeta_t/J)_\zeta\right] \tag{3-7}$$

Where the time metrics are defined as:

$$\xi_t / J = -\left[x_\tau(\xi_x / J) + y_\tau(\xi_y / J) + z_\tau(\xi_z / J)\right]$$

$$\eta_t / J = -\left[x_\tau(\eta_x / J) + y_\tau(\eta_y / J) + z_\tau(\eta_z / J)\right] \tag{3-8}$$

$$\zeta_t / J = -\left[x_\tau(\zeta_x / J) + y_\tau(\zeta_y / J) + z_\tau(\zeta_z / J)\right]$$

In many practical applications involving deforming grids (such as the dynamic aeroelastic FSI model developed), the grid speeds are not known a priori and must therefore be approximated to the desired degree of accuracy using the evolving coordinates at several time levels. Higher order finite difference schemes retain their superior accuracy on rapidly distorting grids when this procedure is used to determine the time metrics [46].

3.2 Finite Volume Concept

An alternate approach to enforcing the metric identities and thus preserving free-stream capturing in high order finite difference schemes is the finite volume to finite difference concept proposed by Vinokur [47]. In this approach, the coordinate transformation metrics represent normal surfaces and the Jacobian becomes the inverse of the volume formed by these surfaces. This approach begins with the derivation of the finite volume formulation, which is then adapted to the finite difference grid. The integral form of the metric identities can be written as:

$$\oint_S n\, dS = 0 \tag{3-9}$$

$$V(t_2) - V(t_1) = \int_{t_1}^{t_2} \oint_{S(t)} n \cdot v_c dS\, dt \tag{3-10}$$

where S represents the cell surface, n is the normal to the surface, V is the volume of the cell, and v_c represents the surface velocity relative to the non-inertial frame but expressed in the inertial frame. The first identity is a mathematical expression for a closed cell while the second identity represents the conservation of volume for a time-varying cell from time t_1 to time t_2. By applying the same curvilinear coordinate transformation as used with the governing equation of motion, these two expressions take the following differential form for a finite volume:

$$\left(S^{\xi}\right)_{\xi} + \left(S^{\eta}\right)_{\eta} + \left(S^{\zeta}\right)_{\zeta} = 0 \tag{3-11}$$

$$V_{\tau} = \left(S^{\xi} \cdot r_{\tau}\right)_{\xi} + \left(S^{\eta} \cdot r_{\tau}\right)_{\eta} + \left(S^{\zeta} \cdot r_{\tau}\right)_{\zeta} \tag{3-12}$$

Where the surfaces and volume are related to the metric derivatives and Jacobian by:

$$\begin{aligned} r &= [x \quad y \quad z]^T \\ S^{\xi} &= r_{\eta} \times r_{\zeta} = \tfrac{1}{J}[\xi_x \quad \xi_y \quad \xi_z]^T \\ S^{\eta} &= r_{\zeta} \times r_{\xi} = \tfrac{1}{J}[\eta_x \quad \eta_y \quad \eta_z]^T \\ S^{\zeta} &= r_{\xi} \times r_{\eta} = \tfrac{1}{J}[\zeta_x \quad \zeta_y \quad \zeta_z]^T \\ V &= r_{\xi} \cdot r_{\eta} \times r_{\zeta} = \tfrac{1}{J} \end{aligned} \tag{3-13}$$

Figure 3-1 shows a regular hexahedral cell for a finite volume, where all the edges are assumed to be straight lines.

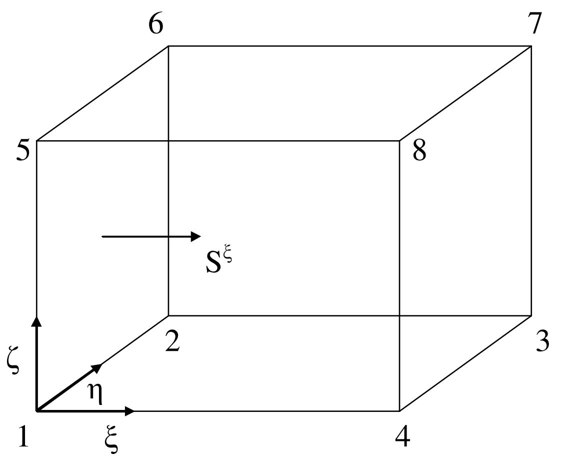

Figure 3-1. Geometry of a finite volume hexahedral cell

From Figure 3-1, the surface vectors are given by:

$$
\begin{aligned}
S^\xi &= \tfrac{1}{2}(r_6 - r_1)\times(r_5 - r_2) \\
S^\eta &= \tfrac{1}{2}(r_5 - r_4)\times(r_8 - r_1) \\
S^\zeta &= \tfrac{1}{2}(r_3 - r_1)\times(r_2 - r_4)
\end{aligned}
\tag{3-14}
$$

Note that the surface vectors are taken in the positive coordinate direction so as to satisfy the geometric identities on the hexahedron. The surface vector evaluations in Equation 3-14 can be regarded as the evaluation of the free-stream capturing metrics for a stationary grid.

Next the standard time metrics are considered using finite volume notation:

$$
\begin{aligned}
\frac{\xi_t}{J} &= -S^\xi \cdot r_\tau \\
\frac{\eta_t}{J} &= -S^\eta \cdot r_\tau \\
\frac{\zeta_t}{J} &= -S^\zeta \cdot r_\tau
\end{aligned}
\tag{3-15}
$$

Unfortunately, it has been shown that time metrics in equation 3-15 will not maintain the free-stream even with the use of free-stream capturing metrics [48]. Even worse, such inconsistent time metrics do not satisfy the GCL. To demonstrate this, consider Equation 3-12, which represents the GCL in finite volume. Now let the grid move in the rigid rotation, that is $V_\tau = 0$ and $r_\tau = U$ x r. Then the left hand side of Equation 3-12 is zero, but the right hand side results in $\left(r \times S^\xi\right)_\xi + \left(r \times S^\eta\right)_\eta + \left(r \times S^\zeta\right)_\zeta \neq 0$. This indicates that the use of the GCL condition (Equation 3-12) for computing V_τ can be erroneous. In other words, the GCL condition is necessary to preserve the free-stream, but not sufficient to construct consistent metrics in space and time. Fortunately, this can be overcome by redefining the time metrics as the time averaged volume swept by the surface [47]:

$$\frac{\xi_t}{J} = -\frac{1}{\Delta t}\int_{t_1}^{t_2} S^\xi \cdot r_\tau dt = -\frac{V_{S^\xi}}{\Delta t}$$

$$\frac{\eta_t}{J} = -\frac{1}{\Delta t}\int_{t_1}^{t_2} S^\eta \cdot r_\tau dt = -\frac{V_{S^\eta}}{\Delta t} \qquad (3\text{-}16)$$

$$\frac{\zeta_t}{J} = -\frac{1}{\Delta t}\int_{t_1}^{t_2} S^\zeta \cdot r_\tau dt = -\frac{V_{S^\zeta}}{\Delta t}$$

To demonstrate this, let $S(t_1) = S_{1562}$ and $S(t_2) = S_{1'5'6'2'}$ as illustrated in Figure 3-2. The volume swept by the xi surface vector between time t_1 and time t_2 becomes:

$$V_{S^\xi} = V_{122'1'566'5'} = \tfrac{1}{3}\left(S_{11'5'5} + S_{122'1'} + S_{1562}\right)\cdot\left(r_{6'} - r_1\right) \qquad (3\text{-}17)$$

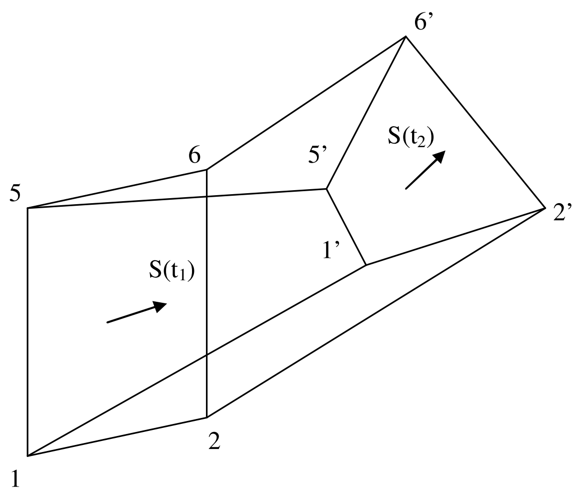

Figure 3-2. Volume swept by a surface

It is worth noting that the time metrics defined by Equation 3-16 contain all information about the movement of a cell surface, including translation, rotation, and deformation. By contrast, the time metrics in Equation 3-15 are a simple product of the surface area and velocity of the cell centroid, thus they can only represent translational motion. As with the previous discussion of the Thomas and Lombard approach, the physical time step derivative in Equation 2-16 is split using the chain rule of differentiation as per Equation 3-6. However, the time derivative of the inverse Jacobian now takes the following form using the metric identity Equation 3-12 with the modified time metrics just discussed:

$$\left(\frac{1}{J}\right)_\tau = V_\tau = -\left[\left(\frac{V_{S^\xi}}{\Delta t}\right)_\xi + \left(\frac{V_{S^\eta}}{\Delta t}\right)_\eta + \left(\frac{V_{S^\zeta}}{\Delta t}\right)_\zeta\right] \tag{3-18}$$

To apply the previous discussion to a finite difference grid, the edges of the hexahedron in Figure 3-1 are redefined as a double sized cell in the finite difference grid (i.e. $r_1 = r_{i-1,j-1,k-1}$, $r_2 = r_{i-1,j+1,k-1}$, $r_3 = r_{i-1,j+1,k+1}$, $\cdots$, $r_8 = r_{i+1,j-1,k+1}$). Since the surfaces are now effectively quad sized, the surface vectors defined in Equation 3-14 must now be divided by a factor of four and the volume of the cell by a factor of 8. In order to obtain higher accuracy, the surfaces are evaluated at the center of the hexahedron as described in reference[48]:

$$\begin{aligned}
S^{\xi}_{i,j,k} &= \tfrac{1}{8}\left(r_{i,j+1,k+1} - r_{i,j-1,k-1}\right)\times\left(r_{i,j-1,k+1} - r_{i,j+1,k-1}\right)\\
S^{\eta}_{i,j,k} &= \tfrac{1}{8}\left(r_{i-1,j,k+1} - r_{i+1,j,k-1}\right)\times\left(r_{i+1,j,k+1} - r_{i-1,j,k-1}\right)\\
S^{\zeta}_{i,j,k} &= \tfrac{1}{8}\left(r_{i+1,j+1,k} - r_{i-1,j-1,k}\right)\times\left(r_{i-1,j+1,k} - r_{i+1,j-1,k}\right)
\end{aligned} \tag{3-19}$$

This helps obtain higher accuracy by relaxing the “straight line edge” requirement for the hexahedron mentioned earlier, since the line between any three successive points on a finite difference grid will mostly likely not be straight. For convenience of comparison with the standard definition, the spatial metric derivatives at point (i, j, k) are evaluated as:

$$\begin{aligned}
&\xi_x = J\left[\tfrac{1}{8}\left(dy_1 dz_2 - dz_1 dy_2\right)\right] \quad \xi_y = J\left[\tfrac{1}{8}\left(dz_1 dx_2 - dx_1 dz_2\right)\right]\\
&\xi_z = J\left[\tfrac{1}{8}\left(dx_1 dy_2 - dy_1 dx_2\right)\right] \quad \eta_x = J\left[\tfrac{1}{8}\left(dy_3 dz_4 - dz_3 dy_4\right)\right]\\
&\eta_y = J\left[\tfrac{1}{8}\left(dz_3 dx_4 - dx_3 dz_4\right)\right] \quad \eta_z = J\left[\tfrac{1}{8}\left(dx_3 dy_4 - dy_3 dx_4\right)\right]\\
&\zeta_x = J\left[\tfrac{1}{8}\left(dy_5 dz_6 - dz_5 dy_6\right)\right] \quad \zeta_y = J\left[\tfrac{1}{8}\left(dz_5 dx_6 - dx_5 dz_6\right)\right]\\
&\zeta_z = J\left[\tfrac{1}{8}\left(dx_5 dy_6 - dy_5 dx_6\right)\right]
\end{aligned} \tag{3-20}$$

$$\begin{aligned}
dx_1 &= x_{i,j+1,k+1} - x_{i,j-1,k-1} & dy_1 &= y_{i,j+1,k+1} - y_{i,j-1,k-1} & dz_1 &= z_{i,j+1,k+1} - z_{i,j-1,k-1}\\
dx_2 &= x_{i,j-1,k+1} - x_{i,j+1,k-1} & dy_2 &= y_{i,j-1,k+1} - y_{i,j+1,k-1} & dz_2 &= z_{i,j-1,k+1} - z_{i,j+1,k-1}\\
dx_3 &= x_{i+1,j,k+1} - x_{i-1,j,k-1} & dy_3 &= y_{i+1,j,k+1} - y_{i-1,j,k-1} & dz_3 &= z_{i+1,j,k+1} - z_{i-1,j,k-1}\\
dx_4 &= x_{i+1,j,k-1} - x_{i-1,j,k+1} & dy_4 &= y_{i+1,j,k-1} - y_{i-1,j,k+1} & dz_4 &= z_{i+1,j,k-1} - z_{i-1,j,k+1}\\
dx_5 &= x_{i+1,j+1,k} - x_{i-1,j-1,k} & dy_5 &= y_{i+1,j+1,k} - y_{i-1,j-1,k} & dz_5 &= z_{i+1,j+1,k} - z_{i-1,j-1,k}\\
dx_6 &= x_{i-1,j+1,k} - x_{i+1,j-1,k} & dy_6 &= y_{i-1,j+1,k} - y_{i+1,j-1,k} & dz_6 &= z_{i-1,j+1,k} - z_{i+1,j-1,k}
\end{aligned}$$

From Equations 3-13, the volume of the hexahedron cell must be calculated in order to obtain the Jacobian. While numerous formulas exist for this calculation, the two most efficient numerical algorithms are the Long Diagonal (LD) method and the Tetrakis Hexahedron (TH) method [49]. The LD method splits the hexahedron into six tetrahedra, but introduces directional preferences along the diagonals selected for triangulation, resulting in a broken symmetry which is undesirable from a physics standpoint. The TH method preserves the diagonal symmetry by defining an additional vertex at the barycenter of each face, but as a result requires more floating point operations or flops, 72 compared to 60 for the LD method. The formulas for these methods using the double sized cell edges are given in Equations 3-21 and 3-22.

$$
\begin{aligned}
\tfrac{3}{8}V_{LD} = &\left\{\left(r_{i-1,j+1,k+1} - r_{i-1,j-1,k-1}\right)\times\left(r_{i-1,j-1,k+1} - r_{i-1,j+1,k-1}\right)\cdot\left(r_{i+1,j+1,k+1} - r_{i-1,j-1,k-1}\right)\right\} \\
&+\left\{\left(r_{i-1,j-1,k+1} - r_{i+1,j-1,k-1}\right)\times\left(r_{i+1,j-1,k+1} - r_{i-1,j-1,k-1}\right)\cdot\left(r_{i+1,j+1,k+1} - r_{i-1,j-1,k-1}\right)\right\} \\
&+\left\{\left(r_{i+1,j+1,k-1} - r_{i-1,j-1,k-1}\right)\times\left(r_{i-1,j+1,k-1} - r_{i+1,j-1,k-1}\right)\cdot\left(r_{i+1,j+1,k+1} - r_{i-1,j-1,k-1}\right)\right\}
\end{aligned}
\tag{3-21}
$$

$$
\begin{aligned}
\tfrac{12}{8}V_{TH} = &\left\{\left[\left(r_{i+1,j+1,k+1} - r_{i+1,j-1,k-1}\right)+\left(r_{i-1,j+1,k+1} - r_{i-1,j-1,k-1}\right)\right]\times\left[r_{i+1,j+1,k+1} - r_{i-1,j+1,k-1}\right]\right. \\
&\left.\cdot\left[r_{i+1,j+1,k-1} - r_{i-1,j-1,k-1}\right]\right\} \\
&+\left\{\left[r_{i-1,j+1,k+1} - r_{i-1,j-1,k-1}\right]\times\left[\left(r_{i+1,j+1,k+1} - r_{i-1,j+1,k-1}\right)+\left(r_{i+1,j-1,k+1} - r_{i-1,j-1,k-1}\right)\right]\right. \\
&\left.\cdot\left[r_{i+1,j+1,k+1} - r_{i-1,j-1,k+1}\right]\right\} \\
&+\left\{\left[r_{i+1,j+1,k+1} - r_{i+1,j-1,k-1}\right]\times\left[r_{i+1,j-1,k+1} - r_{i-1,j-1,k-1}\right]\right. \\
&\left.\cdot\left[\left(r_{i+1,j+1,k+1} - r_{i-1,j-1,k-1}\right)+\left(r_{i+1,j+1,k-1} - r_{i-1,j-1,k-1}\right)\right]\right\}
\end{aligned}
\tag{3-22}
$$

Taking special note of Equation 3-15 with reference to Equation 3-19, the number of flops for the LD method can be considerably reduced by reusing the calculated surfaces of the spatial derivatives of the metrics. In addition, the LD and TH methods for computing the volume of a cell can also be used for calculating the volume swept by each surface vector to obtain the time metrics. In comparison with the Thomas and Lombard approach of recasting the metrics in conservative form, the finite volume concept has the advantage of not being dependent on the differencing scheme used for the fluxes.

3.3 Performance Investigation

As distributed by NASA, Corsair uses the finite volume concept for the spatial derivative metrics along with Equation 3-15 for the evaluation of time metrics. However as shown in reference [48], the resulting time metrics are then inconsistent. In addition, since grids are not allowed to deform in the version of Corsair distributed by NASA, the time derivative of the Jacobian is not included in the time derivative of the solution vector Q.

An investigation of the two methods just discussed for evaluating both the spatial and temporal metrics was performed using the procedure in reference [50], the results of which were then used to determine the best method to implement in Corsair to correct the metric calculation deficiencies. For these test, all boundary conditions were turned off and Corsair was compiled with double precision (15 digits) floating point accuracy. To ensure all boundary conditions had been turned off, an uniform flow field (u=1, v=w=0) was marched in time on a 21x21x21 uniform grid with unity spacing between adjacent points (which effectively sets the metrics to unity) for 200 time steps with a Δt of 0.05. As expected, there was no variation in the v and w velocities from their initial values of zero. The procedure in reference [50] involves reproducing this same free-stream flow, but on a heavily distorted or wavy 3D grid. Error is measured as maximum variation in the *v* and *w* velocities from zero. The wavy 3D grid used for these tests is defined by the following formulae:

$$x_{i,j,k}(\tau) = x_{\min} + \Delta x_0 \left[(i-1) + A_x \sin(2\pi\omega\tau) \sin\left(\frac{n_{xy}\pi(j-1)\Delta y_0}{L_y} \right) \sin\left(\frac{n_{xz}\pi(k-1)\Delta z_0}{L_z} \right) \right]$$

$$y_{i,j,k}(\tau) = y_{\min} + \Delta y_0 \left[(j-1) + A_y \sin(2\pi\omega\tau) \sin\left(\frac{n_{yx}\pi(i-1)\Delta x_0}{L_x} \right) \sin\left(\frac{n_{yz}\pi(k-1)\Delta z_0}{L_z} \right) \right] \tag{3-23}$$

$$z_{i,j,k}(\tau) = z_{\min} + \Delta z_0 \left[(k-1) + A_z \sin(2\pi\omega\tau) \sin\left(\frac{n_{zx}\pi(i-1)\Delta x_0}{L_x} \right) \sin\left(\frac{n_{zy}\pi(j-1)\Delta y_0}{L_y} \right) \right]$$

$$i = 1 \ldots IL; \quad j = 1 \ldots JL; \quad k = 1 \ldots KL; \quad \Delta x_0 = \frac{L_x}{IL-1}; \quad \Delta y_0 = \frac{L_y}{JL-1}; \quad \Delta z_0 = \frac{L_z}{KL-1}$$

To begin with, a stationary 3D wavy grid as shown in Figure 3-3 was generated from Equation 3-23 by setting the parameters IL=JL=KL=21, A_x=A_y=A_z=1, L_x=L_y=L_z=4, n_{xy}=n_{yz}=…=n_{zy}=4, ω=1, and τ=0.25 (the time at which maximum displacement occurs).

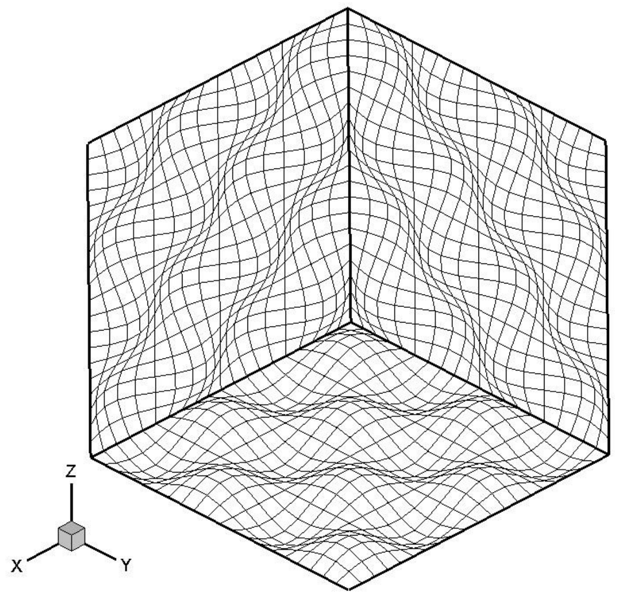

Figure 3-3. Three-dimension wavy grid

This grid was then used to evaluate the performance of the spatial derivative metrics. An initial solution of uniform flow (u=1, v=w=0) was then marched in time for 50 time steps with a $\Delta\tau$=0.05 using first, second, and third order spatial accuracy with three Newton sub-iterations. The resulting maximum deviations of the v and w velocities from zero for the various methods and spatial accuracy are displayed in Table 3-1.

	1st Order	*2nd Order*	*3rd Order*
Standard Definition	7.271E-2	1.011E-1	1.162E-1
Conservative Recasting	7.463E-14	1.085E-14	1.140E-14
FV Concept w/ LD	5.859E-16	6.320E-16	6.358E-16
FV Concept w/ TH	5.122E-16	6.154E-16	5.215E-16

Table 3-1. Free-stream preservation errors for stationary 3D wavy grid

As expected, the largest error occurs for the standard definition of the metrics given in Equation 2-18. While the conservatively recast metrics of Thomas and Lombard show significant improvement compared to the standard definition, they are not quite as accurate as the finite volume concept. This may be due to the accumulation of numerical or round off error, as the conservative recasting method does entail significantly more numerical operations than the finite volume concept. There is little to no difference between the long diagonal (LD) and tetrakis hexahedron (TH) methods used to calculated volumes in the finite volume concept method. However, the long diagonal does have the advantage of requiring significantly fewer flops since the surface vectors can be reused in calculating the volume of the cell.

Next, the ability of each method to preserve the free-stream on a dynamically deforming curvilinear grid was tested. Again, the wavy 3D grid described by Equation 3-23 was used but with the following parameters: $IL=JL=KL=31$, $A_x=A_y=A_z=1.5$, $L_x=L_y=L_z=12$, $n_{xy}=n_{yz}=\ldots=n_{zy}=4$, and $\omega=1$. An initial uniform flow solution was marched in time with a $\Delta\tau=0.005$ for 50 time steps with the grid deformed at each time step according to Equation 3-23. Thus, the 3D grid begins with a uniform spacing of 0.4 between adjacent points but ends up with the maximum deformation similar to Figure 3-3 after 50 time steps. As with testing of the spatial metric derivatives, this simulation was run for first, second, and third order spatial accuracy with different combinations of temporal and spatial metric derivative calculation methods. The resulting maximum deviation of v and w from their initial value of zero for each combination is shown in Table 3-2 and is used to gauge their performance.

Spatial Method	*Temporal Method*	*1st Order*	*2nd Order*	*3rd Order*
Corsair (No J_τ Correction) *FV Concept (LD) & Std. Def.*		6.865E-2	8.552E-2	8.813E-2
Std. Def.	*Std. Def.*	4.396E-3	4.783E-3	4.718E-3
Std. Def.	*V_S(LD)*	3.945E-3	4.541E-3	4.489E-3
Conserv. Recast	*Std. Def.*	6.506E-8	3.944E-13	2.613E-13
Conserv. Recast	*V_S(LD)*	2.321E-9	1.283E-13	1.022E-13
FV Concept (LD)	*Std. Def.*	6.020E-9	1.461E-14	2.613E-14
FV Concept (LD)	*V_S(LD)*	7.052E-11	2.928E-15	1.385E-16
FV Concept (TH)	*V_S(TH)*	5.625E-11	2.344E-15	1.254E-16

Table 3-2. Free-stream preservation errors for deforming 3D wavy grid

In Table 3-2, the first method tested is the unmodified version of Corsair in which the Jacobian is assumed not to change with time. The remainder of Table 3-2 is split up into combinations of methods for evaluating the spatial and temporal metric derivatives. For spatial methods, Std. Def. is the standard definition given by Equation 2-18, Conserv. Recast is the conservatively recast form of the spatial metrics given by Equation 3-5, and FV Concept (LD) & FV Concept (TH) are the finite volume concept given in Equation 3-19 with the volume of the hexahedron calculated using the long diagonal and tetrakis hexahedron methods, respectively. For the temporal methods, Std. Def. is the standard definition given in Equation 3-8, and V_S(LD) & V_S(TH) are the finite volume concept of a volume swept by the surface vectors given in Equation 3-16 using the Long Diagonal and Tetrakis Hexahedron formulae respectively.

Results for the unmodified version of Corsair illustrate the importance of including the temporal derivative of the Jacobian in the temporal derivative of the solution vector Q, even with a high order spatial metric derivative method. Along similar lines, the results using the standard definition for the spatial metric derivatives show large errors, regardless of the spatial metric derivative method used. The conservative recasting method for the spatial metric derivatives shows marked improvement over the standard definition, but still has a larger error than the finite volume concept method. A slight improvement gain for the conservative recasting method is shown when paired with the swept volume idea from the finite volume concept method for calculating the temporal metric derivatives. Most likely, this improvement is the result of accounting for deformation of the spatial metrics between time steps. When paired with the standard definition for the temporal metric derivatives, the finite volume concept using long diagonals results in error similar to that for the conservatively recast metrics method. However, when the finite volume method for spatial metric derivatives is paired with the swept volume method for the temporal metric derivatives, the error is noticeably reduced. Lastly, there appears to be very little difference in terms of error between using the long diagonal or tetrakis hexahedron methods for calculating volumes when the finite volume concept is used for both spatial and temporal metric derivatives.

In this chapter, three numerical methods for the evaluation of the coordinate transformation metrics were investigated for use in Corsair. These methods included the standard analytical form, the conservatively recast form, and the finite volume to finite difference concept. Each method was examined using a highly distorted static and dynamically deforming, wavy grid for spatial and temporal metrics respectively. The error associated with each method was quantified as the maximum deviation of non-axial velocities from zero when performing a uniform axial free-stream reproduction test. In addition, combinations of spatial and temporal methods were compared, including use of long diagonals and tetrakis hexahedrons for the calculations of volumes in the finite volume to finite difference method. Results clearly show that the standard analytical form produces significant free-stream errors when deformed three dimensional grids are used with a finite difference solver. Hence the standard analytical form of the metrics should be avoided when using a finite difference solver with a deformed curvilinear grid. While the conservatively recast method significantly reduced these errors, the finite volume to finite difference concept was able to reduce them even further and with fewer floating point operations. Although the tetrakis hexahedron method showed slightly better results, it requires significantly more floating point operations than the long diagonal method when reusing the surface vectors (spatial metric derivatives) in computing the temporal metric derivatives (swept volumes). Thus, the finite volume concept with long diagonals was chosen to correct the metric calculation deficiencies in Corsair.

4. WALL FUNCTION

As outlined in Section 1.1, one of the main objectives required in order for the resulting aeroelastic solver to be used as a design tool is reduction of the time required to run a simulation. One of the most direct ways of achieving this is simply to reduce the total number of grid points used in the simulation, since the runtime is directly proportional. In a typical Corsair simulation, the grid density near solid surfaces is intentionally high in order to accurately calculate the shear stress using a finite difference approach, a technique commonly known as gridding to the wall. Accurate calculation of the shear stress is critical, as it is used for calculation of turbulence in the flow and additionally will be utilized by the FSI module to determine the aerodynamic forces on the blade surface. By replacing the finite difference calculation of the shear stress with one based on empirical data (i.e. a wall function), the number of grid points near solid surfaces and thus the total number of grid points can be substantially reduced while still obtaining accurate shear stresses. This chapter covers the wall function added to Corsair for the current research, including the use of the shear stress in the turbulence model, and a comparison of the two shear stress methods using a fourth standard configuration turbine blade.

4.1 Background Boundary Layer Theory

In the 1930s, Prandtl and Von Karman deduced that turbulence consists of three separate layers: a very small inner layer next to the surface where viscous (molecular) shear is dominant termed the laminar sub-layer, an outer layer where turbulent (eddy) shear is dominant called the fully turbulent zone, and a transition layer called the buffer zone [51]. It is common in turbulence modeling to regroup these three layers into just two regions, an inner region which includes the laminar sublayer, the buffer layer, and part of the fully turbulent zone, and an outer region which consists of the remaining part of the fully turbulent zone [52]. To delineate between these two regions, a non-dimensional coordinate y^+ of approximately 400 is taken to be the upper limit of the inner region, where y^+ is defined as

$$y^+ = \frac{y\sqrt{\rho_{wall}\left|\tau_{wall}\right|}}{\mu_{wall}} \tag{4-1}$$

Here, y is the normal distance from the wall, ρ_{wall} is the density at the wall, τ_{wall} is the shear stress at the wall, and μ_{wall} is the laminar viscosity at the wall.

The unsteady Navier-Stokes equations fully describe the fluid flow field including turbulence, but require resolving very small spatial and temporal details in order to correctly model turbulence. A common approach used in order to obtain meaningful results with reasonable grid densities is to average the equations of motion over relatively small time periods [52]. This results in the Reynolds Averaged Navier-Stokes (RANS) form of the equations of motion with apparent stresses due to the time unsteadiness. Boussinesq introduced a hypothesis, commonly referred to as the Boussinesq assumption, which simply states that the apparent stress can be related to the strain multiplied by the turbulent viscosity [52]. Thus, to include the effects of turbulence, the molecular viscosity μ in the stress terms of the Navier-Stokes Equations is replaced by ($\mu_l + \mu_t$) and the term (μ / Pr) in the heat conduction term is replaced by ($\mu_l / \mathrm{Pr}_l + \mu_t / \mathrm{Pr}_t$), where the l and t subscripts denote laminar and turbulent quantities respectively. By using this approach, the Navier-Stokes equations remain unchanged in form. For air, the turbulent Prandtl number, Pr_t, and the laminar Prandtl number, Pr_l, are generally taken to be 0.9 and 0.74 respectively. The laminar viscosity is generally modeled by Sutherland's law, where μ_l is a function of the local static temperature [51]. However, the turbulent viscosity, μ_t, is not so easily determined and as a result, several turbulence models have been developed over the years to solve for this term in order to close the RANS formulation of the equations of motion.

4.2 Algebraic Model

Zero-equation turbulence models use equations where the turbulent fluctuating correlations are related to the mean flow field quantities by algebraic relationships. The underlying assumption in such models is that the local rate of turbulence production is approximately equal to the rate of turbulence dissipation. Furthermore, they do not include convection of turbulence. Obviously, this is contrary to the physics of most flow fields, since the past history of flow must be accounted for. However, these models are mathematically simple and their incorporation into a numerical code is relatively easy to accomplish. One of the most commonly used zero-equation turbulence models is the Baldwin-Lomax model [53]. In this two-layer model, the turbulent viscosity μ_t is described by

$$\mu_t = \begin{Bmatrix} \mu_{t-inner} & s \le s_{crossover} \\ \mu_{t-outer} & s > s_{crossover} \end{Bmatrix} \tag{4-2}$$

Where s is the distance normal to the surface and $s_{crossover}$ is the smallest value at which $\mu_{t\text{-}inner}$ equals $\mu_{t\text{-}outer}$. In the inner region, the turbulent viscosity is calculated using the Prandtl-Van Driest formulation

$$\mu_t = \rho l^2 |\omega| \tag{4-3}$$

where ω is the vorticity defined as

$$\omega = \frac{\partial v}{\partial x} - \frac{\partial u}{\partial y} \tag{4-4}$$

and the mixing length l is given by

$$l = \kappa y \left(1 - e^{-\left(y^+ / A^+ \right)} \right) \tag{4-5}$$

Here, κ is the Von Karman constant (~0.41) and A^+ is a parameter which depends on the streamwise pressure gradient and has a value of 26 for zero-pressure gradient flows.

However, Granville [54] has provided a review of alternative formulae which may be used in order to account for the presence of pressure gradients and surface roughness. He proposed the following formula for the mixing length to most closely match experimental data

$$l = \kappa y \sqrt{\tau^*} \left(1 - e^{-\left(y^+ \sqrt{1+bP^+} / 26 \right)} \right) \tag{4-6}$$

where b is set to 14.0 for $P^+ < 0$ (favorable pressure gradient) and to 16.4 for $P^+ > 0$ (adverse pressure gradient). The parameter P^+ represents the pressure gradient and is defined as

$$P^+ = \left(\frac{\nu}{\rho u \left(\tau_{wall} \tau^*\right)^3} \right) \frac{\partial P}{\partial x} \tag{4-7}$$

Here, v is the kinematic viscosity and τ^* represents the non-dimensional total shear stress close to the wall and is given by

$$\tau^* = 1 + P^+ y^+ \tag{4-8}$$

The turbulent viscosity in the outer region is approximated by

$$\mu_t = \alpha \rho C_{CP} F_{wake} F_{Kleb} \tag{4-9}$$

where α is the Clauser constant and usually assigned a value of 0.0168 for flows in which the momentum thickness Reynolds number is greater than 5000, and

$$F_{wake} = \min\left[y_{\max} G_{\max}, C_{wake} y_{\max} \frac{(\Delta V)^2}{G_{\max}} \right] \tag{4-10}$$

Typically, C_{wake} is given a value of 0.25 and the term $y_{\max}$ is the value of y corresponding to the maximum value of G, denoted $G_{\max}$, across the layer where

$$G(y) = \frac{l}{\kappa}|\omega| = y|\omega|\left(1 - e^{-\left(y^+ / A^+ \right)} \right) \tag{4-11}$$

The difference between the absolute values of the maximum and minimum velocities within the viscous region is denoted by ΔV. For wall bounded flows, the minimum velocity occurs at the surface where the velocity is zero, thus

$$\Delta V = \left(u^2 + v^2 + w^2 \right)^{1/2} \tag{4-12}$$

For shear layer flows, ΔV is defined as the difference between the maximum velocity and the velocity at the $y_{\max}$ location, hence

$$\Delta V = \left(u^2 + v^2 + w^2 \right)^{1/2}_{\max} - \left(u^2 + v^2 + w^2 \right)^{1/2}_{y_{\max}} \tag{4-13}$$

F_{Kleb} is an intermittency factor which provides additional smoothing and is defined as

$$F_{Kleb} = \left[1 + 5.5\left(\frac{C_{Kleb}\,y}{y_{\max}}\right)^6\right]^{-1} \tag{4-14}$$

and as before, $y_{\max}$ is the y location where $G_{\max}$ occurs. Typical values for the Klebanoff constant C_{Kleb} and C_{CP} are 0.3 and 1.6, respectively, for zero to mild pressure gradients. However, according to Granville [55], these "constants" should really be variable and suggest a fit to known properties of Cole's wake law and equilibrium pressure gradients

$$C_{Kleb} = \frac{2}{3} - \frac{0.01312}{0.1724 - \beta^*} \tag{4-15}$$

where

$$\beta^* = \frac{y_{\max}}{u_t}\frac{\partial V}{\partial x} \tag{4-16}$$

and u_t is the friction velocity. The velocity gradient in β^* is calculated outside the viscous region. Once the Klebanoff constant has been evaluated, C_{CP} is calculated using

$$C_{CP} = \frac{3 - 4C_{Kleb}}{2C_{Kleb}\left(2 - 3C_{Kleb} + C_{Kleb}^3\right)} \tag{4-17}$$

This modification is believed to give the Bawin-Lomax model accuracy comparable to the mixing-length and Clauser iterative models.

Corsair uses the modified version of the Baldwin-Lomax turbulence model just discussed. Additional modifications, based on the developers' experience with compressor and turbine geometries, are also employed in Corsair [56]. First, the equations are applied along grid lines rather than normals to the surface. This avoids the calculation of all the normal distances and the interpolation of flow variables. Second, the switchover location between the inner and outer models is not allowed to move more than a specified number of grid points between adjacent streamwise locations. In addition, a second derivative smoothing function is used on the turbulent viscosity field in separated flow regions. This eliminates non-physical gradients in the turbulent viscosity near separation points. Thirdly, a cutoff value is imposed on the turbulent viscosity (nominally 1200 times the free-stream laminar viscosity). Finally, a limit is imposed on $s_{crossover}$ in order for it not to occur too far beyond the wall.

<u>4.3 Wall Function Model</u>

Implementation of the Baldwin-Lomax turbulence model requires the wall shear stress. In the original form of Corsair distributed by the NASA Marshal Space Flight Center, the wall shear stress is calculated using a finite difference approach. This requires a very fine grid spacing, or clustering, to be used near solid surfaces such as the hub, shroud, and blade, in order to resolve the entire boundary layer ($y^+ \sim 2$) and obtain the correct shear stress. In addition, this fine grid spacing requires a significantly small time step in order to maintain stability via the CFL law [52]. To overcome these limitations, wall functions have been implemented in Corsair. Wall functions make use of empirical data to determine the wall shear stress based on the Reynolds number at a normalized distance away from the wall. By using this empirical relationship, the grid needs only to be fine enough near the surface to ensure the log-linear correlation is valid. According to turbulent boundary layer theory, the inner layer obeys the following relationship at the wall:

$$\mathrm{Re} = y^+ u^+ \tag{4-18}$$

where y^+ is the inner region normalized distance, u^+ is the inner region normalized velocity, and Re is the local Reynolds number just above the surface. The relationship between u^+ and y^+ is well known from experimental work of turbulent water flow in smooth pipes [51]. Additionally, Spalding devised a single composite formula which describes this relationship for the entire wall-related region [57]:

$$y^+ = u^+ + e^{-\kappa b}\left[e^{\kappa u^+} - 1 - \kappa u^+ - \frac{(\kappa u^+)^2}{2} - \frac{(\kappa u^+)^3}{6}\right] \tag{4-19}$$

In the Equation 4-19, κ is the Von Karman constant and assigned the value of 0.41 while b is the logarithmic friction law constant and is typically given a value of 5.5 for hydraulically smooth surfaces. The first part of Equation 4-19 represents the viscous sublayer ($y^+ = u^+$), while the second half represents the buffer and logarithmic layers. This formula blends the three regions in a smooth fashion, which shows excellent agreement with experimental data up to a y^+ of ~500, where a slight wake occurs [51].

Implementation of wall functions in Corsair starts with a calculation of the local Reynolds number at the first grid point away from the surface:

$$\mathrm{Re} = \left(\frac{\rho W \delta y}{\mu_l}\right) \tag{4-20}$$

where δy is the normal distance from the surface, W is the relative velocity vector, and ρ is density. A curve fit to the u^+- y^+ relationship from Spalding's formula along with Equation 4-1, is then used to determine u^+ and y^+ from the calculated local Reynolds number. Once u^+ is known, the shear stress at the wall is given by:

$$\tau_w = \frac{\rho W^2}{u^+} \tag{4-21}$$

In addition, the local skin friction coefficient can also be calculated according to:

$$C_f = \frac{2}{(u^+)^2} \tag{4-22}$$

In terms of the inner law-of-the-wall distance, *y*+, a maximum value of ~500 can now be used with wall functions versus a maximum of ~2 without.

4.4 Surface Roughness

Surface roughness (resulting from deposits, erosion, or finishing) can have a significant effect on the aerodynamic performance of turbomachinery [58,59]. This effect comes from the break up of the thin viscous sublayer, which increases the wall friction and thus changes the location of transition from laminar to turbulent flow. Since surface roughness can greatly change the location of transition, it is important to include its effect in the turbulence model. The simplest way to incorporate surface roughness in most turbulence models is through the computation of the wall stress via the wall friction. In Corsair, such a method described by Shabbir and Turner is utilized [60].

The effect of surface roughness enters Spalding's formula, Equation 4-19, via the logarithmic friction law constant *b*. It is important to note that this limits the effect of surface roughness to the buffer and logarithmic layers. However, since the lower buffer layer and laminar sublayer have been blended in Spalding's formula, the effects of surface roughness can be applied to the upper part of the buffer layer, at best. Thus, this limits the minimum y^+ for inclusion of surface roughness effects in the wall function using Spalding's formula to ~20 [60].

The sand roughness experiments of Nikuradse characterized the effect of roughness on the velocity profile by the equivalent sand roughness Reynolds number defined as:

$$k_s^+ = \frac{\rho k_s \sqrt{\tau_w/\rho}}{\mu_w} \tag{4-23}$$

where k_s is the equivalent sand roughness height [61]. The surface is considered hydraulically smooth if $k_s^+ \leq 5$ and is considered completely rough if $k_s^+ \geq 70$. The range in between, $5 < k_s^+ < 70$, is the known as the transition range. Based on the measurements of Nikuradse, the logarithmic friction law constant can be expressed as a function of surface roughness:

$$b = B - 2.5\ln\left(k_s^+\right) \tag{4-24}$$

where the coefficient B has been determined experimentally for a range of surface roughness values. For hydraulically smooth and rough surfaces, B is a function of k_s^+, but for completely rough surfaces it is a constant with an average value of 8.5.

In the work of Shabbir and Turner, families of curves are plotted for the variation of the skin friction coefficient as a function of local Reynolds number for various surface roughness values, where the coefficient B was obtained from reference [61]. This plot is reproduced here as Figure 4-1 and also includes lines of constant k_s^+/y^+. This data was used to plot the local Reynolds number as a function of the ration between surface roughness to the first grid point height above the surface (k_s^+/y^+) for different values of surface roughness, reproduced here as Figure 4-2. Given these two plots, the local Reynolds number, and the ratio of surface roughness to the first grid point height above the surface (k_s^+/y^+), the skin friction coefficient can be determined explicitly. To aid in programming this method, the plots in Figures 4-1 and 4-2 have been curve fitted using polynomials.

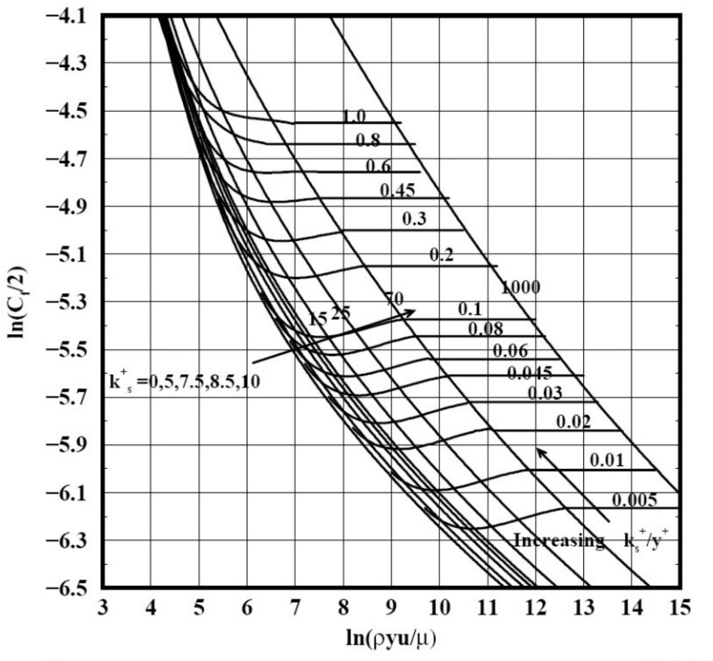

Figure 4-1. Skin friction coefficient as a function of local Reynolds number

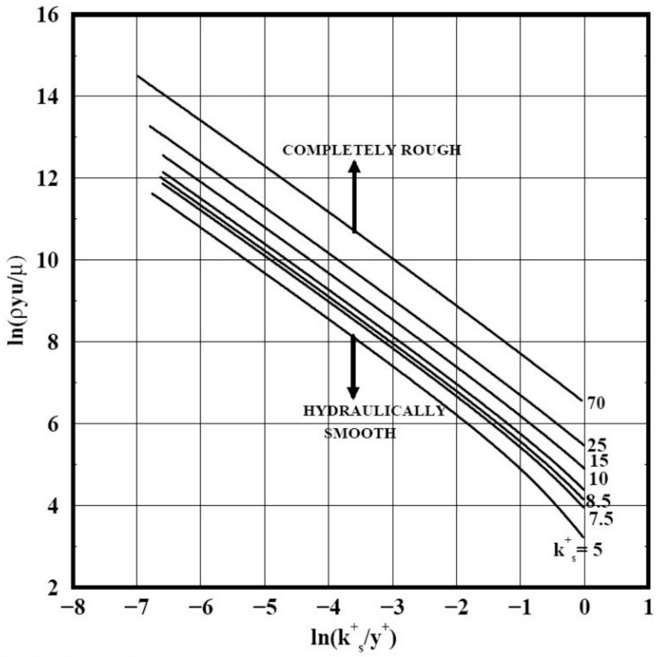

Figure 4-2. Local Reynolds number as a function of surface roughness to grid height ratio

For a given grid and surface roughness, the ratio $k_s^+/y^+ = k_s/y$ is fixed. The corresponding local Reynolds number then determines one of three possible surface conditions and the associated skin friction. First, a calculation of $\mathrm{Re}_{\mathrm{smooth}}$ is made from a curve fit to Figure 4-2 for $k_s^+ = 5$. If the local Reynolds number is equal to or smaller than $\mathrm{Re}_{\mathrm{smooth}}$ then the surface is hydraulically smooth and a curve fit to the skin friction coefficient is made from Figure 4-1. If the surface is found not to be hydraulically smooth, then it is checked to see if it is completely rough. To determine this, $\mathrm{Re}_{\mathrm{rough}}$ is calculated from the curve fit for $k_s^+ = 70$ in Figure 4-2. if the local Reynolds number is equal to or greater than $\mathrm{Re}_{\mathrm{rough}}$, then the surface is completely rough and the skin friction coefficient is computed from a curve fit for $k_s^+ = 70$ in Figure 4-1.

If the surface is not hydraulically smooth or completely rough, then it is obviously in the transition region. For this case, the skin friction coefficient is calculated in three steps. In the first step, k_s^+/y^+ along with the local Reynolds number *Re* are used in conjunction with Figure 4-2 to determine which two lines (out of the seven) encompass the surface under consideration, call these two associated Reynolds numbers Re_1 and Re_2. In the second step, the corresponding lines on Figure 4-1 are identified and the skin friction coefficients, call them C_{f1} and C_{f2}, are calculated from their curve fits. In the third step, the desired skin friction coefficient C_f is obtained with a simple linear interpolation:

$$C_f = C_{f1} + \frac{(C_{f2} - C_{f1})}{(\mathrm{Re}_2 - \mathrm{Re}_1)}(\mathrm{Re} - \mathrm{Re}_1) \tag{4-25}$$

4.5 Test Case

To test the implementation of these wall functions, an appropriate test case is required. A typical case used to test both the implementation of wall functions and turbulence models is a flat plate [62,63]. In such test cases, free-stream conditions such as pressure, temperature, and Mach number are specified and the numerical results compared to either analytical or experimental data for skin friction at the wall surface. A major drawback to this particular type of test case involves the difficulty of generating an O-grid for an infinitely thin flat plate. In addition, the skin friction coefficients used in the wall function are experimentally obtained from tests on flat plates, making such a test redundant.

Instead, a more realistic turbomachinery test case involving the fourth standard configuration (STCF4) is used to test the wall function implementation in Corsair. The fourth standard configuration represents a typical section of a modern free standing turbine, with relatively high blade thickness and camber, operating under strong subsonic flow conditions. It is ideally suited for testing since a wealth of experimental results from the annular cascade facility at the Lausanne Institute of Technology exists in the public domain [64]. The cascade consists of twenty prismatic blades, each with a chord of approximately 2.83 inches and a span of just over 1.57 inches, with 45 degree turning and a maximum thickness to chord ratio of 0.17. The stagger angle is 56.6 degrees with a blade to blade pitch of 2.2 inches. For this test, case three of the experimental test series is used. For this case, the inlet and exit flow angles are 45.5 and 71.0 degrees, respectively, with inlet and exit Mach number of 0.28 and 0.90, respectively. For this test, the pressure coefficients at mid-span for both the gridding-to-wall and wall functions are compared with experimental measurements. For the gridding-to-wall simulation, a refined O-grid (271x67x51) with a distance to first grid line from the blade surface of 0.00003 inches was used resulting in a maximum y^+ of ~1.85. The wall function simulation used a coarser O-grid (241x29x51) with a distance to first grid line from the blade surface of 0.0018 inches resulting in a maximum y^+ of ~48.2. For both simulations, the same H-grid (161x85x51) was used and the simulations were run at third order accuracy with a single Newton sub-iteration. While three Newton sub-iterations are generally used to reduce error from the approximate factorization of the governing equations, a single Newton sub-iteration is sufficient for these runs since the solution is steady state (not time accurate) and quicker results can be obtained. Both solutions were run for the same non-dimensional time. However, the gridding-to-wall simulation required a time step one third the size of the wall function simulation in order to maintain stability. As a result of the time step and grid size differences, the gridding-to-wall run took roughly 4.5 times longer than the wall function run. Figure 4-3 is a contour plot of the Mach numbers for the wall function simulation at mid-span, illustrating the fourth standard configuration flow domain.

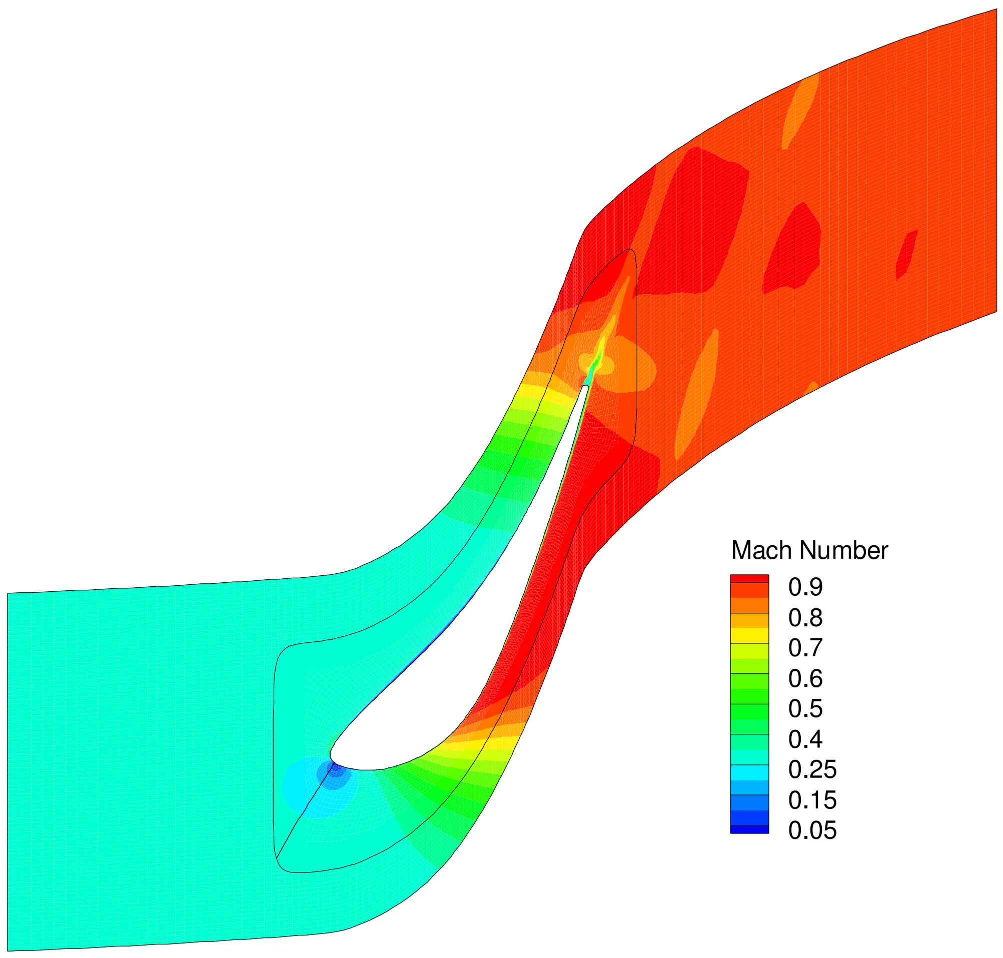

Figure 4-3. STCF4 flow domain

Figure 4-4 shows the coefficient of pressure at mid-span for the two runs compared with the time averaged experimental measurements.

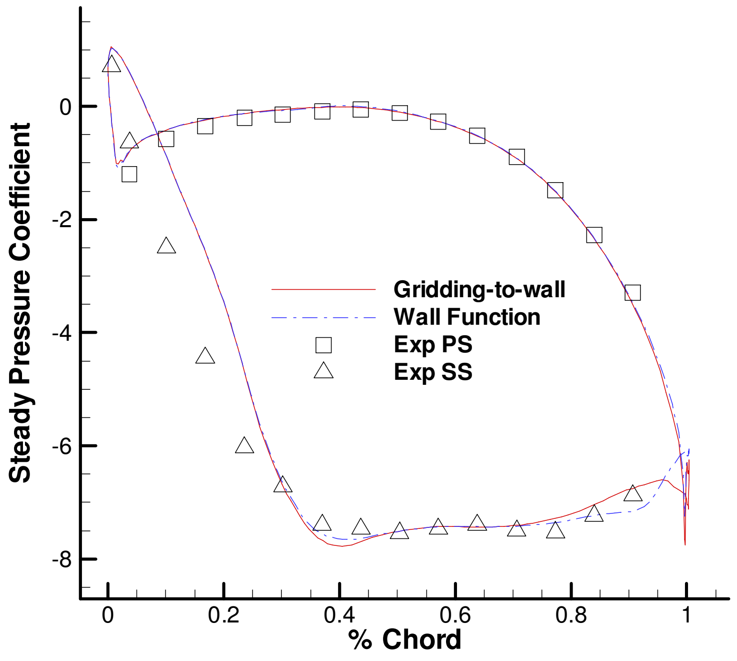

Figure 4-4. STCF4 pressure coefficients at mid-span

As shown in Figure 4-4, there is little to no difference between the results obtained using the gridding-to-wall method versus the wall function. There is a slight difference between the two at the trailing edge of the suction side, but this is most likely due to the vortex shed by the rounded trailing edge of the fourth standard configuration. Comparison with the experimental data is also quite good. The difference between experimental and computational simulation results in the first 30% of the chord is due to uncertainty in the inlet flow angle of the experiment, as described in the Lausanne Institute of Technology report.

The addition of a wall function to Corsair for the calculation of shear stress at solid surfaces was discussed in this chapter. A background introduction of boundary layer theory was presented to show the importance of accurate shear stress calculations and the use of this quantity in the turbulence model employed in Corsair. The wall function replaces the gridding-to-the-wall, finite difference approach, used in the original version of Corsair. Details of the wall function implementation were also covered including the ability to account for surface roughness. More importantly in meeting the objectives in section 1.1, the wall function allows for a significant reduction in grid cluster near solid surfaces, resulting in overall smaller grids and thus reduced runtimes. Finally, a comparison of the two methods was made using the fourth standard configuration. The results not only showed a reduction in runtime due to the reduction in grid size, but also from the ability to use larger time steps while still maintaining stability.

5. ADDITIONAL PARALLELIZATION

One of the objects for this research as outlined in section 1.1 was to create an aeroelastic solver that could be used in the design phase of turbomachinery. While the incorporation of the wall function discussed in the previous chapter significantly reduces the runtime for a simulation, even greater reductions are desired. This chapter covers the restructuring/rewriting of the flow solver along with addition domain decomposition which was added, in order to further reduce runtimes. Details of the computer resources utilized for this research are also given.

5.1 Existing Parallelization in Corsair

As distributed by NASA Marshall Space Flight Center, Corsair is parallelized for use with MPI and MP-threads [10]. MPI is used for the coarse breakup of the computational grid, with each grid being solved on a separate node. MP-threads is used to further break up the calculations of each grid by using multiple Cores/CPUs on each node. While the calculations in Corsair have been parallelized via MPI and open-MP, the data structure has been kept serial. For SMP shared memory architectures such as the one Corsair was developed on, this program structure is rather efficient. Unfortunately, this same program structure on distributed memory architectures, such as the Beowulf cluster used for this research, have severe parallelization and memory limitations. For example, since the Beowulf cluster used for this research consist of single core nodes, the open-MP feature of Corsair could not be used and thus only the coarse breakup of one grid per node via MPI could be used. Further, the serial data model limits the problem size that can be solved since the entire problem domain must fit in the memory of each node used in a parallel run. This serial data model also results in a tremendous amount of communication, since the entire flow domain must be updated after each iteration on all nodes used for a parallel run. To overcome these limitations, Corsair was rewritten with a focus on distributing the data structure with the calculations. The resulting flow solver, called Thunder, allows for more parallel scalability, a reduced nodal memory footprint, and the ability to solve larger problem on distributed memory architectures such as the Beowulf cluster used for this research. In addition, a general clean up of the code is achieved, resulting in faster performance and allowing for easier integration of the FSI module.

5.2 Target Computational Platform

For this research, the target computational platform is the Taylor Beowulf cluster which consists of 92 compute nodes, 3 head nodes, and a file server all connected using a Gigabit network. The compute nodes are grouped into two racks each composed of 46 nodes and a 48 port gigabit network switch (see Figure 5-1), while a third 48 port gigabit network switch is used to connect the head nodes and file server together. To tie the network switches together, two ports from each of the compute node group network switches are bonded together and connected to the network switch used for the head nodes and file server in a tree configuration. Although bonding two ports together effectively doubles the bandwidth between the switches, this does not fully compensate for cases where parallel runs are split between compute node racks. However, it was found during initial setup and testing of the cluster that this tree configuration did provide better performance than a ring configuration between the three network switches. The network configuration for the Taylor cluster is shown in Figure 5-2. Each compute node consists of a single core 2.4 GHz AMD Athlon 64 3800+ processor with 1 GB of DDR400 RAM along with a 40 GB hard drive providing local scratch space. While multi-core processors were available, their cost/performance at the time of the Taylor cluster construction precluded them from being used for the compute nodes. In addition, the ability for the chosen scheduler & queue system to handle multi-core nodes was not fully developed yet [65], resulting in the belief that for most users multi-core nodes would lead to a waste of computing resources. DLink 1248T 48 port GigE switches along with CaT6 cables are used for the network. The Taylor cluster uses the 64 bit version of cAos 2.0 Linux distribution along with Torque for the queue system and Maui for queue management.

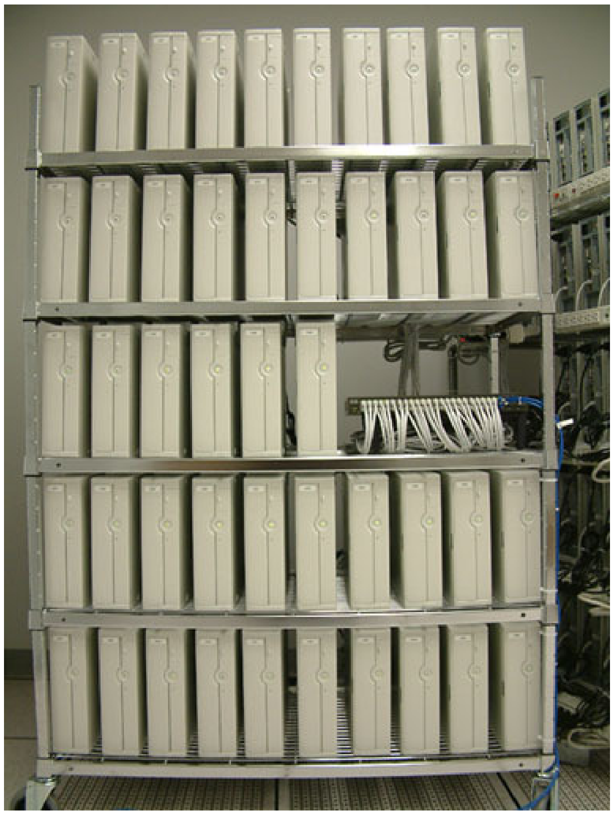
Figure 5-1. Taylor cluster compute node rack

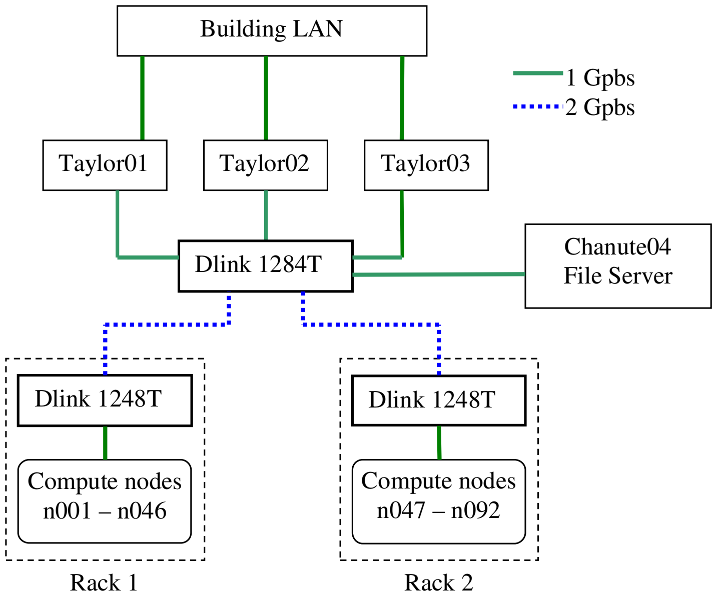

Figure 5-2. Taylor cluster network configuration

5.3 Code Restructuring

As stated earlier, Corsair uses a parallelized calculation with serial data program structure. While this type of structure can run efficiently on SMP supercomputers with shared memory, such a program structure is very inefficient on distributed memory architectures, such as the Beowulf cluster used in this research, for two primary reasons [66,37]. First, the serial memory model limits the size of problems which can be solved to what will fit in the memory of a single node. For the Taylor Beowulf cluster, this limits the size of a problem to ~1 GB of memory, which based on experience roughly translates to a problem domain of 1.5 million total grid points when using double precision accuracy. Second, since each node must maintain an up to date copy of the entire problem domain (grid points, flow variables, etc.), a tremendous amount of communication is required between all the nodes after each iteration.

Corsair is written in FORTRAN 77 and thus one of its inconveniences is that the source code must be recompiled for each new problem size. To do this, a parameter file containing the index size of several arrays must first be edited to fit the desired target problem. However, since several key index sizes are grouped together, the resulting arrays are often much larger than they need to be. Corsair also uses a somewhat unusual vector based storage method. While large vectors are used to store the solution and grid points for the entire problem domain, smaller multi-dimensional arrays are used for temporary storage of appropriate portions of the problem domain while they are being used in calculations or being solved for. This storage method makes it easier to update the entire flow domain after each iteration, since the data is already in a packed form, but in addition to requiring more memory, it also incurs a heavy time penalty each time a large portion of these vectors is written into a multi-dimensional array or vice versa.

To overcome these issues, a restructure version of Corsair called Thunder was developed using only MPI for parallelization. The decision to use MPI instead the mixed hybrid MPI and openMP model used in Corsair is based on two reasons. First, programming with hybrid parallel models is prone to errors. Second, modern implementations of MPI (such as MPICH, LAM, and openMPI) are optimized to run on multi-core/multi-CPU noded systems just as well as single core/CPU noded systems. Unlike Corsair, Thunder is written in Fortran 95 and takes advantage of dynamically allocated multi-dimensional arrays for storing data, thus removing the need to recompile the code for each new problem size. In addition, each node stores only its portion of the flow domain, along with a minimum amount of data required for the ghost points. This significantly reduces the nodal memory footprint, along with the amount of communication required after each iteration.

Unlike most parallel flow solvers [67], the grid and solution files in Thunder are not split before or during a run, but rather read and written as whole files by the master node. Since the size of these files for a particular problem might be bigger than the amount memory on the master node, it reads only the grid/solution for a single blade at a time, passes this information via MPI to the appropriate node(s), and then proceeds to read in the grid/solution for the next blade. For writing grid and solution files, a similar process is used in reverse. Thunder also has the ability for each node to read and/or write its solution and/or grid files in a broken up manner. However, complete grid and solution files are often more desired by CFD users for post processing of results and by having

Thunder read/create these files as whole, reduces the extra step of splitting/joining individual files.

Early in the development of Thunder, it was noticed that one of the main reasons for the serial data structure in Corsair was the need for information during the solution process about the global problem domain, such as the number overlap/Chimera points between O- and H-grids. A simple preprocessing utility called thsplit was developed to solve this problem. Some of the information each node receives from the splitup file generated by thsplit is given in table 5-1. In addition to providing this information about the global problem domain, thsplit also includes the logic for breaking up individual grids and nodal communication information, such as which nodes a particular node must exchange information with.

num_rows	Number of blade rows
total_num_blades	Total number of blades
my_blade	Blade in row this node solves for
my_blade_master	First node assigned to my_blade
my_row	Row this node solves for
my_row_master	First node assigned to my_row
k_global(4)	K indexes in global problem domain (1=first local, 2=last local, 3=last global, 4=global tip clearance start)
imx_h, jmx_h, kmx_h	Index sizes of problem portion for H-grid solved by this node
imx_o, jmx_o, kmx_o	Index sizes of problem portion for O-grid solved by this node
imx_c, jmx_c, kmx_c	Index sizes of problem portion for clearance grid solved by this node
cutout_idx(4)	Beginning and ending Indexes (i and j) for H-grid cutout
num_chm_pts_o	Number of O-grid overlap/Chimera points
num_chm_pts_h	Number of H-grid overlap/Chimera points
min_rad_in	Inlet radius of the hub for my_row
max_rad_in	Inlet radius of shroud for my_row
tip_rad_in	Inlet radius of blade tip for my_row
num_blades(n)	Number of blades in each row n
num_procs_blade(n)	Number of processors used for each blade in row n
overlap(n)	Number of radial overlap points in row n
split_type(n)	1 if O- and H-grid on same node, 2 otherwise
ogrid(n)	True or false, based on an O-grid being present for row n
tip_clearance(n)	True or false, based on a clearance grid being present for row n

Table 5-1. Some global information generated by thsplit for each node

While most of the capabilities in Corsair have been duplicated in Thunder, a few such as hot streaks and film cooling have not yet been added. The addition of these capabilities to Thunder would be rather straight forward, but they have not been implemented yet as they were not needed for this research. In addition, Corsair has the ability to model centrifugal compressors while Thunder does not. However, unlike the hot streaks and film cooling, this capability would require a significant amount of source code rework to implement in Thunder. Fortunately, this research only deals with axial flow turbomachinery and thus the capability to model centrifugal compressors was left out of Thunder.

In order to give Thunder more parallel flexibility, an option to keep both the O- and H-grid of a blade or portion thereof on the same node was added. This capability is specified when running thsplit via split_type. As shown in Table 5-1, a one indicates both O- and H-grid for a blade or blade portion be kept on the same node, thus allowing better scalability when these two grids are different sizes and eliminating the communication of flow variables for the overlap/Chimera post iterative update. In addition, this feature provides more parallelization by allowing an H-grid with a long inlet or exit to be decomposed into separate axial sections. For example, a passage with a long inlet can be broken into two rows, one with the inlet portion of the H-grid and no overlaid O-grid and a separate row with the remaining H-grid and overlaid O-grid. By setting split_type to two, the O- and H-grids are split onto separate nodes, reverting to the normal decomposition behavior of Corsair.

Another significant difference between the structure of Thunder and Corsair is the use of separate communicators for O-grids, H-grids, CFD work, and FSI work compared to the single mpi_comm_world communicator used in Corsair. This allows for more efficient groups of communications to occur and is very helpful when creating barrier calls for which only a particular group of nodes must be synchronized. Each node in a parallel run of Thunder dumps an output deck which in addition to tracking residuals for its portion of the flow field also lists the node it is running on, making the debugging process on large numbers of nodes much easier.

Along with the general clean up of code, variables in Thunder are much better defined. In Corsair, common blocks, implicit declarations, equivalent statements, and six character variable names make following or adding to the source code a difficult process at best. In thunder, all global variables are defined in the globaldata module using descriptive names, with implicit none used throughout the code to easily trap undeclared variables. Additionally, the precision of real variables in Thunder is specified in the globaldata module and in the Makefile. Thunder can be built for single, double, or quad precision via the Makefile and the number of digits used for each type of precision is specified in the globaldata module. When compiling Corsair for double or single precision via compiler flags, the source code also has to be modified in numerous locations to ensure mpi_real8 or mpi_real respectively is used for sending real data via MPI calls. This simple variable tells MPI how many bits make up a real variable and if set incorrectly, scrambles data sent by MPI. Instead of using the mpi_real or mpi_real8 defined in the MPI header file, Thunder uses its own declared variable, mpi_real_prec, which is set at the beginning of code to the compiled precision using the MPI command mpi_type_create_f90_real. This ensures all real data sent using MPI commands is done correctly.

5.4 Increased Parallelization

To add more parallelization to Thunder and thus increase turn around time for cases involving only a single blade passage, logic was added for splitting individual O- and H-grids onto separate nodes. Numerous different options exist in the literature for accomplishing this with CFD codes [67,68,69,70,71]. Since Thunder is based on structured grids, the most straight forward method is to break up the grids along one or more of the grid indexes. For both the O- and H-grids, the axial or i index is always the largest, followed by the circumferential or j, and lastly the radial or k directions. From a purely parallel standpoint, the axial direction should thus be the best choice for breaking up the grids, since it would allow for more decomposition and the best possibility for good load balancing. However, from a CFD standpoint, breaking up the grids in the axial direction involves several problems. First of which, the axial direction involves the most amount of fluid flow changes and thus any error introduced via boundary conditions to handle the splitting of the domain in the axial direction will be greatly amplified. Along similar lines, the boundary conditions for such a decomposition of the domain would require numerous ghost points and associated communication overhead to ensure continuity. Second, the axial direction for the H-grid is different than that for the O-grid, which would make the communication pattern for overlap/Chimera post iterative updates very complicated. Similar issues exist for decomposing the grids in the circumferential or j direction.

Thus the ideal direction for decomposing both O- and H-grids is in the radial or k direction, since the physical translation of this direction is the same for both grid types, unlike the axial and circumferential directions. Also, the least amount of change in the 3D flow field occurs in the radial direction, thus any error introduced by boundary conditions for handling the decomposition is minimized. Lastly, the radial boundary conditions themselves are rather straight forward, as the patch condition between axially adjacent H-grids can be easily modified for both the O- and H-grids in the radial direction.

As previously mentioned, a utility called thsplit was created to handle and optimize the decomposition of the grids in the radial direction. The input deck for thsplit requires the following information from the user for each blade row: number of nodes to use for each blade, the splitype, number of radial overlap points to use, and which blade to use for calculation of the splitup. Figure 5-3 illustrates a radial decomposition overlap of three points. While a minimum of two points can theoretically be used, experience has shown that three overlap points is optimal, with more overlap points not yielding any better convergence. To accomplish the splitup in an organized fashion, a handful of rules are created to control how grids are decomposed in the radial direction. These rules are based on the ideas of keeping the communication between decomposed portions of the grid simple and maintaining the best load balancing. The first rule is that all O- and H-grids in a row are split along the same radial indexes, keeping communication of the overlap/Chimera and radial periodic post iterative updates between single nodes. This rule also implies that if split_type is set to two, the number of nodes per blade must be a multiple of two. For structured grids, load balancing is almost entirely dependent on the number of grid points between nodes being as equal as possible. Thus the second decomposition rule is to split the grids in such a manner that the individual portions have as close to possible the same number of grid points. In reality, this can be very difficult to accomplish, especially if the O- and H-grids are to be separated. However, if the grids are broken up between a relatively few number of nodes, adding or subtracting a radial slice when generating the grids can help balance things, at least in the radial direction. If a clearance grid is present, it is kept with its associated O-grid portion and the O-grid, along with the H-grid, can not be split along any radial index where the clearance grid resides. This prevents the massive amount of communication which would be required for the continuity condition between the O-grid and clearance grid. In general, clearance grids significantly reduce the amount of decomposition which can be accomplished while obtaining good load balancing.

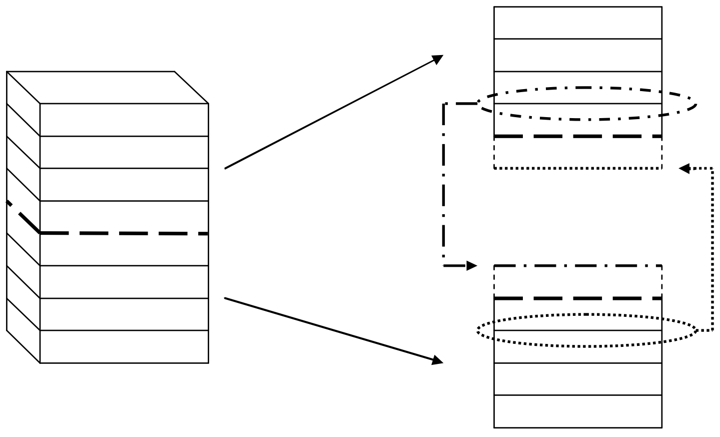

Figure 5-3. Illustration of three radial overlap points

The algorithm in thsplit uses these rules as follows. First the number of processors to be used for a blade is checked against split_type. If split_type is two, then the number of processors to be used is checked to make sure it is a multiple of two (aborting the run if not) and setting the number of desired blade sections to one half the number of processors to be used per blade. If split_type is one, then the number of desired blade sections is simply set to the number of processors per blade. The number of points for both the O-grid, and clearance grid if present, are totaled and the number of overlap points between radial sections is multiplied by the number of desired blade sections minus one and added to this total, resulting in the total number of grid points. This is then divided by the number of desired blade sections to determine the optimal number of grid points each section should contain in order to obtain good load balancing. However, it rarely works out that the optimal number of grid points correlates to a whole number of radial 2D slices. For such cases, the number of grid points resulting from using a whole numbers of 2D slices is compared to the optimal number of points for a blade section. Whichever number of whole 2D slices comes closest to this value is used. Next, the number of points in this section is subtracted from the total number of points and the total number of remaining points is divided by the number of desired blade sections minus one. The process then repeats for the remaining number of blade sections. To ensure the clearance grid is kept with its associated O-grid and thus satisfy one of the decomposition rules mentioned earlier, the decomposition algorithm is carried out starting at the shroud and working toward the hub. If the optimal number of 2D slices for the first section is less than that used by the clearance grid, then the first section is increased to include the clearance grid. An example using a clearance grid is now given to help illustrate this process.

For this example, consider the fourth standard configuration (STCF4) used earlier to test the wall functions. Assume that the H-grid is 161x65x50, the O-grid is 241x33x50, and a clearance grid of 241x17x5 are used and the number of processors per blade is set to ten with split_type set to one (O- and H-grids not separated) and a radial overlap of three points. First the total number of points would be (241 x 33 x 50) + (241 x 17 x 5) + (3 x (10 – 1) x 241 x 33) = 632,866 points. It is interesting to note from this calculation how many additional grid points are added as ghost points, in this case 241 x 33 x 9 or a whopping 71,577 points! Next, this is divided by the desired number of blade sections, ten, which results in the optimal block size of 63,286.6 points. Obviously the optimal block size does not result from a whole number of 2D slices. Since this case also includes a tip clearance grid, the first block must include this grid and its associated O-grid portion. Quickly calculating the number of grid points involved, 241 x 50 x 5 =

60,250 points, the clearance grid and its associate O-grid portion are found to be within the block size for this case. Now to determine the k slice at which to make the first cut, the number of points for each additional slice below the clearance grid is added till the optimal block size is reached, in this case 241 x 33 = 7,953 points. Doing this, a cut at k of 47 would result in a block size of 60,250 or 3,036.6 points under the optimal block size. A cut at k of 48 however would result in a block size of 68,203 or 4,916.4 points over the optimal block size. Thus the first block is from k of 47 to 51. The remaining total number of grid points is then recalculated as 632,866 – (241 x 33 x 5) – (241 x 17 x 5) = 572,616 grid points. Dividing by the remaining nine desired blade sections gives an optimal block size of 63,624 points. Dividing this by the size of each 2D O-grid section, 63,624 / (241 x 33) = 8, thus the next blade section will contain 8 slices and be from k of 42 to 49. The reason the section ends at 49 instead of 47 is because of the three point overlap. Also note that only the number O- and Clearance grid points are used when determining the decomposition. This is because the H-grid, like the O-grid, has the same number of points at each radial slice and thus does not change the calculated radial slices. Repeating this process, each of the remaining blade sections will contain 8 slices as shown in Table 5-2.

Node	Radial slice (k indexes)	Grid types	Total number of grid points
1	1 – 8	O & H	147,344
2	6 – 13	O & H	147,344
3	11 – 18	O & H	147,344
4	16 – 23	O & H	147,344
5	21 – 28	O & H	147,344
6	26 – 33	O & H	147,344
7	31 – 38	O & H	147,344
8	36 – 43	O & H	147,344
9	41 – 48	O & H	147,344
10	46 – 50	O, H, & Clearance	112,575

Table 5-2. Decomposition indexes of example STCF4 grid domain

When dealing with multi-blade row configurations, the H-grids between blade rows must exchange information along the slip boundary. Since the number blades defining this slip boundary may be different in axially adjacent rows and Thunder uses a distributed data model, a communication procedure using sets of master nodes was implemented. This procedure begins with the exchanging of coordinate information at the slip boundary between axially adjacent rows. First, each node sends its portion of the slip boundary coordinate information to the master node for the blade (blade master node) in that row. Next, each of these blade master nodes sends its slip boundary coordinates to the row master node. Finally, the row master nodes for axially adjacent rows exchange coordinate information. These coordinates are then stored on the row masters for interpolation after each iteration. A similar process for the flow field variables is used for the post iterative update. Each node sends its flow field variables for the adjacent rows slip boundary to the blade master node, the blade master node(s) then send this information to the row master node. The row master nodes then exchange these flow field variables at the slip boundary with each other, from which they interpolate the correct flow field values based on circumferential location and periodicity. Finally, the row master node sends the appropriate portions of the interpolated slip boundary values to blade master nodes, which then pass the appropriate portions of this information onto the individual nodes associated with the same blade.

5.5 Parallel Performance

To gauge the performance of Thunder, a single blade row from the Fourth Standard Configuration (STCF4) is once again modeled for case 3 of the experimental test suite [64]. The grids for this case are 241x33x51 for the O-grid and 161x65x51 for the H-grid. These grid sizes are chosen such that the resulting total number of grid points for each grid are relatively close, helping obtain reasonable load balancing. Before investigating the parallel scalability of Thunder, a comparison to Corsair is performed using two nodes (one for the O-grid and the other for the H-grid) with identical grids and input decks. For this comparison, both codes were compiled using the Intel compilers with optimization level 3. Thunder is set for double precision (15 digits) and Corsair compiled with the –r8 flag, thus building it with 15 digits of precision as well. Both simulations are run at first order spatial accuracy with single Netwon sub-iterations for 32000 iterations, which allowed for a relatively converged steady state solution. The runtime and nodal memory usage for each are shown in Table 5-3.

	Corsair	Thunder
Total Runtime	39.61 hours	30.57 hours
Nodal memory footprint node 1 (node 2)	712048 KB (698128 KB)	354700 KB (285396 KB)

Table 5-3. Runtime and memory usage comparison between Thunder and Corsair

In Table 5-3, the nodal memory footprint is obtained by using the pmap command on each node for the process ID of the executable, thus these values are for all memory being utilized on a node including shared libraries. The results demonstrate that Thunder is ~23% faster than Corsair and is able to distribute the memory requirements for the problem domain between the two nodes, thus reducing the nodal memory footprint by roughly one half. The increase in speed can be contributed to different factors. First, Thunder has fewer memory operations than Corsair, which uses a vector storage model with temporary multi-dimensional arrays. On modern PC platforms, memory operations (copying data back and forth between arrays, especially out of order) can be very time consuming, with a single memory operation being equal to four floating point operations [72]. In addition, loops in Thunder have been optimized by keeping them in column majored order, which is not always the case in Corsair. Lastly, because Thunder uses a distributed memory layout, the amount of communication after each iteration is limited to only ghost points, compared with Corsair's need to communicate the entire problem domain after each iteration. When comparing the final solutions between Corsair and Thunder, the maximum difference in RMS residuals for the five flow variables is 4.01E-13. For reference, the largest RMS residual is 1.33E-10.

Before demonstrating the parallel performance of Thunder, a brief discussion regarding the theoretical capability of the decomposition method used is presented. It is safe to assume that the serial run time per iteration in Thunder is on the order of the number of grid points used:

$$T_S = \Theta\{(IM)(JM)(KM)\} \tag{5-1}$$

where *IM, JM,* and *KM* represent the number of points in each of the three directions. For the parallel run time, an assumption is made that the number of grid points can be equally divided by the number of processors assigned to that grid, thus resulting in sections of equal size or number of grid points. For the radial decomposition method chosen for this research, the ability to accomplish this is based on a combination of the original grid size, the number of overlap points, and the number of sections desired. As previously discussed, the number of overlap points is usually kept to three to obtain good convergence, leaving the grid size and number of desired sections as the two variables one may manipulate in order to obtain equally sized sections of the grid. Even when a tip clearance grid is introduced into this calculation, adding or subtracting one or two radial slices from the total number of grids is enough to obtain relatively equal sized grid sections. Using this radial decomposition entails the communication of *(IM)(JM)* solution vectors, each containing 5 flow variables at the overlap region, resulting in 5*(IM)(JM)* values. Thus the parallel run time in order of complexity can be approximated as:

$$T_P = \Theta\left\{\frac{(IM)(JM)(KM) + (IM)(JM)ovlp(P-1)}{P}\right\} + \Theta\{4(5(IM)(JM) + l)\} \tag{5-2}$$

In Equation 5-2, ovlp is the number of overlap points, *P* is the number of processors. Although documentation for the Dlink switches used in the Taylor cluster is very brief, it does refer to using a spanning tree, which is a method of performing cut through routing.

Thus in the order of complexity for the parallel run time given in Equation 5-2, communication complexity for a cut through routing of *m+l* is used, where *m* is the message size and *l* is the number of links or jumps between processors [73]. The number of messages passed is set to 4, since the center blade/grid sections will need to exchange information at the overlap boundary with both the section below and above. For the Taylor cluster network configuration, the number of links between processors is 2 when the processors communicating are on the same rack, but 4 when the processors are on different racks. While it is obviously desirable to have all processors used in a parallel run on the same rack and thus *l* equal to 2, this can not be guaranteed do to the first available assignment method used by the queue system on the Taylor cluster. Using the standard definitions [73], speedup and efficiency in orders of complexity are given as:

$$S=\frac{T_S}{T_P}=\frac{\Theta\{(IM)(JM)KM)\}}{\Theta\left\{\dfrac{(IM)(JM)(KM)+(IM)(JM)ovlp(P-1)}{P}\right\}+\Theta\{(5(IM)(JM)+l)2\}}$$

$$=\Theta\left\{\frac{(KM)P}{KM+ovlp(P-1)+\left(10+\dfrac{2l}{(IM)(JM)}\right)P}\right\} \tag{5-3}$$

$$E=\frac{S}{P}=\Theta\left\{\frac{KM}{KM+ovlp(P-1)+\left(10+\dfrac{2l}{(IM)(JM)}\right)P}\right\} \tag{5-4}$$

By defining the amount of work done, *W*, as the serial run time, the overhead time (difference between parallel and serial runtimes) can be defined in terms of *W* and the number of processors, *P*. Additionally, the overhead time can be split into extra calculations and communication required for the radial decomposition:

$$W = (IM)(JM)(KM)$$

$$T_O(W,P) = T_{xcalc} + T_{comm} = \frac{ovlp(P-1)W}{KM} + P\left(10 + \frac{2l(KM)}{W}\right) \tag{5-5}$$

Using this, the parallel efficiency [61] can be rewritten in terms of work and number of processors:

$$E = \frac{W}{W + T_O(W,P)} = \frac{1}{1 + T_O(W,P)/W}$$

$$\frac{T_O(W,P)}{W} = \frac{1-E}{E} \tag{5-6}$$

$$W = \frac{E}{1-E} T_O(W,P) = \overline{K} T_O(W,P)$$

$$\hat{W}_{xcalc} = \overline{K}\frac{ovlp(P-1)}{KM}, \quad \hat{W}_{comm} = \sqrt{\overline{K}2l(KM)P} \tag{5-7}$$

Equations 5-7 give the isoefficiency in terms of overlap points, number of processors, and total number of 2D slices for both the extra calculations and communications. These isoefficiencies dictate how large the original problem domain must grow with added processors to maintain a given parallel efficiency. From this it can be seen that the driving factor for both extra calculations and communications is the number of radial 2D slices, *KM*.

The preceding discussion and equation development is for a split_type of one, where both the O- and H-grids are on the same processor. For a split_type of two, where the O- and H-grids are on separate processors, a similar model can be derived. First, the difference in the O- and H-grid sizes must be accounted for. In practical use, the O-grid is generally larger than the H-grid, so for simplicity *W* is taken as the number of O-grid points and the serial run time is redefined using a multiplier *G*, which is one plus the ratio of H-grid to O-grid points. It is also important to note that the number of radial slices, *KM*, for the O- and H-grids is always the same due to the way these grids are defined and generated. With this assumption, the orders of complexity for the parallel and serial run times with split_type of two are derived as:

$$T_S = \Theta\{G \cdot W\} \tag{5-8}$$

$$\begin{aligned} T_P &= \Theta\left\{\frac{\frac{W}{2} + \frac{W}{2KM} ovlp\left(P/2 - 1\right)}{P/2}\right\} \\ &\quad + \Theta\left\{4\left(5\frac{W}{2KM} + l\right) + \frac{(KM + ovlp)\left(P/2 - 1\right)chmp}{P/2} + 2l\right\} \\ &= \Theta\left\{\frac{W}{P} + \frac{Wovlp(P-2)}{2(KM)P}\right\} \\ &\quad + \Theta\left\{\frac{5W}{KM} + \frac{(KM + ovlp)(P-2)chmp}{P} + 6l\right\} \end{aligned} \tag{5-9}$$

Where *chmp* is the total number of Chimera points (both O- and H-grid) per 2D radial slice. The speedup and efficiency are:

$$S = \frac{T_S}{T_P} = \Theta\left\{\frac{G \cdot W2(KM)P}{2(KM)WP + W(p-2)ovlp + 10WP + 2(KM)(KM + ovlp)(P-2)chmp + 12(KM)Pl}\right\} \tag{5-10}$$

$$E = \frac{S}{P} = \Theta\left\{\frac{G \cdot W2(KM)}{2(KM)WP + W(p-2)ovlp + 10WP + 2(KM)(KM + ovlp)(P-2)chmp + 12(KM)Pl}\right\} \tag{5-11}$$

and the overhead time becomes:

$$T_O(W,P) = T_{xcalc} + T_{comm} \tag{5-12}$$
$$= \frac{ovlp(P-2)W}{2(KM)P} + \left\{ \frac{5W}{KM} + \frac{(KM+ovlp)(P-2)chmp}{P} + 6l \right\}$$

Finally, the isoefficiencies are:

$$\hat{W}_{xcalc} = \overline{K}\frac{ovlp(P-2)}{2(KM)P}, \quad \hat{W}_{comm} = \frac{2(KM+ovlp)chmp}{P} \tag{5-13}$$

The parallel scalability of Thunder on the Taylor cluster is investigated next using the same grids and input deck as for the comparison with Corsair, but with different split_types and numbers of processors per blade. To gauge load balancing and the ratio of communication to calculation, Thunder is profiled using calls to cpu_time. The cpu_time call returns the elapsed time in seconds since the beginning of code execution. To gauge load balancing, the time before and after calls to mpi_barrier differenced and totaled together as MPI wait time. Similarly, time spent for communications is obtained by differencing cpu_time calls before and after mpi_send, mpi_recv, mpi_sendrecv, and mpi_bcast calls. Since these are blocking calls and only the actual communication time is desired, mpi_barrier calls inserted before each of these and the time before and after each of these mpi_barrier calls differenced and added to the MPI wait time total. Lastly, calculation time obtained by differencing cpu_time calls before and after the main portion of the code, then subtracting MPI wait and communication times. It is important to note time spent on initialization at the beginning of the code and freeing memory at the end of the code are not included in this timing. In order to plot these values against one another, the MPI wait, MPI communication, and calculation times averaged among the nodes used for the parallel simulation. For the serial runtime required in calculating speedup, Thunder was run on a single node with both number of processors and split_type set to one.

Tables 5-4 and 5-5 lists the ratio of total number of ghost points to original problem domain, raw run times in seconds, speedup, parallel efficiency, and the maximum nodal memory footprint for several number of processors with split_type of one and two respectively. Runs with more than 10 processors for split_type of one, and 20 for splity_type of two, were not performed since the number of ghost points for such cases is more than half the number of points in the original problem domain.

P	$\frac{\textit{ghost pts.}}{KM}$	T_{wait} (sec)	T_{comm} (sec)	T_{calc} (sec)	T_{total} (sec)	S	E (%)	NMF_{max} (MB)
1	0	0.0	0.0	213710.1	213710.1	1.00	100.00	528.3
2	0.06	101.3	8120.5	110285.3	118507.1	1.80	90.17	298.7
3	0.12	184.1	4259.4	75166.8	79610.4	2.68	89.48	231.8
4	0.18	347.1	5561.8	58395.9	64304.8	3.32	83.08	199.3
5	0.24	1705.0	6119.0	48691.0	56515.0	3.78	75.63	181.4
6	0.29	1219.6	6555.2	42343.3	50118.2	4.26	71.07	164.7
7	0.35	2007.0	6400.0	37654.2	46061.3	4.64	66.28	156.5
8	0.41	1044.6	7495.9	34814.1	43354.7	4.93	61.62	153.2
9	0.47	2818.0	9206.5	31592.7	43617.4	4.90	54.44	148.1
10	0.53	2257.5	9098.3	29349.3	40705.1	5.25	52.50	139.9

Table 5-4. Parallel performance for split_type of one

P	$\frac{\textit{ghost pts.}}{KM}$	T_{wait} (sec)	T_{comm} (sec)	T_{calc} (sec)	T_{total} (sec)	S	E (%)	NMF_{max} (MB)
2	0	3081.0	170.3	106803.0	110054.3	1.94	97.09	354.7
4	0.06	1881.7	4102.3	55338.0	61322.0	3.49	87.13	267.3
6	0.12	1412.8	2278.4	37816.8	41508.0	5.15	85.81	177.8
8	0.18	1740.4	2906.1	29211.9	33858.4	6.31	78.90	162.1
10	0.24	3242.3	3008.9	24303.3	30554.5	6.99	69.94	144.8
12	0.29	2886.0	3568.8	21204.5	27659.3	7.73	64.39	136.7
14	0.35	3497.0	3622.7	18886.4	26006.1	8.22	58.70	128.4
16	0.41	2858.8	4056.4	17462.7	24377.9	8.77	54.79	125.8
18	0.47	4825.9	4609.8	15882.3	25318.0	8.44	46.89	123.0
20	0.53	4121.8	4908.3	14726.1	23756.2	9.00	44.98	117.5

Table 5-5. Parallel performance for split_type of two

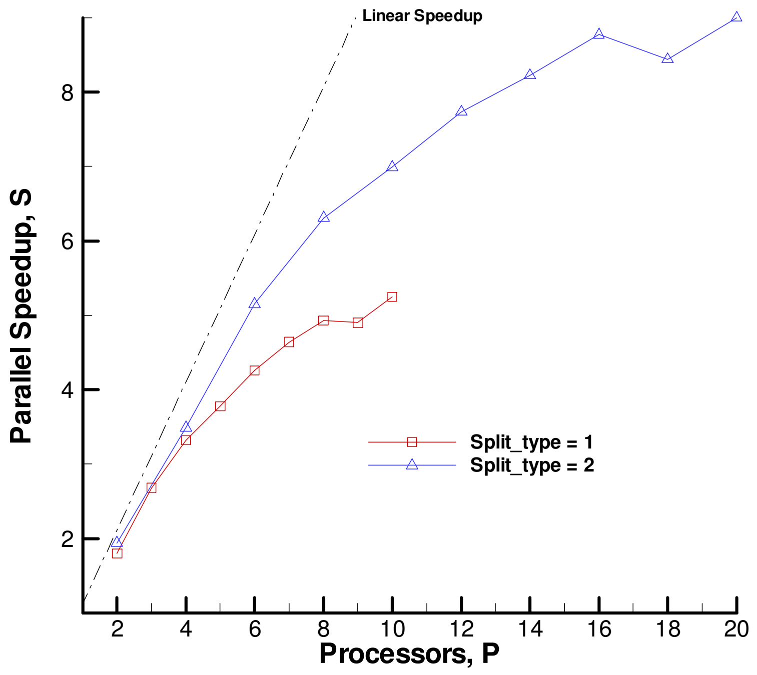

Figure 5-4. Speedup performance

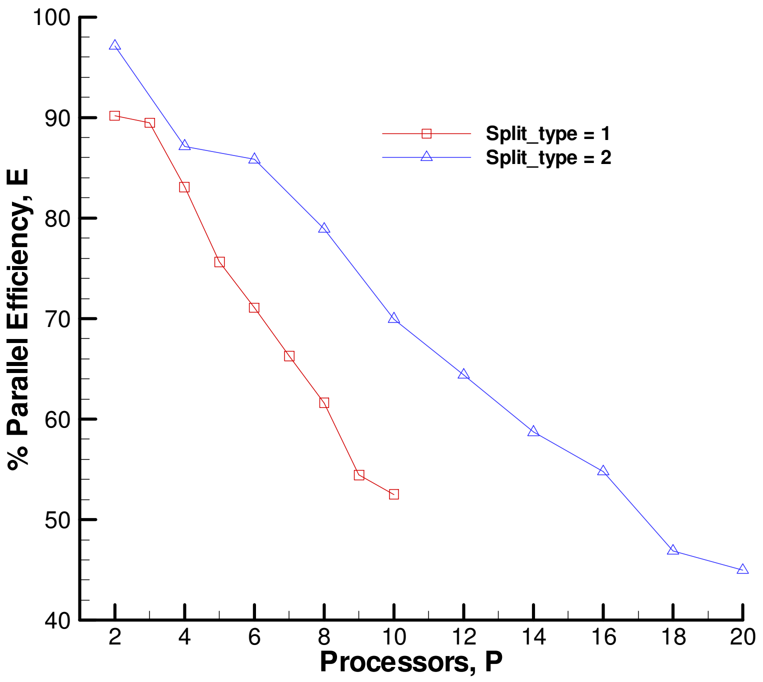

Figure 5-5. Parallel efficiency

Figure 5-4 shows the parallel speedup of Thunder for the test case used with various numbers of processors. From this plot, it is evident that a split_type of two gives nearly double the performance as a split_type of one with increased numbers of processors. This is not surprising, as splitting the O- and H-grids up onto separate processors does not incur any extra cost of calculations for ghost points. In addition, this case was chosen such that the O- and H-grids were of relatively the same size. For cases when the grids are very different sizes, uneven load balancing between processors handling O- versus H-grids would cause a significant drop in the scalability of split_type two. This can also be seen from the equations for speedup developed earlier, i.e. when G becomes much larger than two. In comparison, a split_type of one is not affected by this and thus the reason for implementing it in Thunder. Figure 5-4 also shows that the radial decomposition method chosen is capable of maintaining relatively good parallel scalability for breaking a blade into four radial sections. From Table 5-4, this correlates to a ratio between total ghost points added and the original problem domain of roughly 20%. Beyond this 20% ratio, parallel scalability starts to significantly deviate from linear speedup for both split_types. Lastly, a slight dip in the speedup curves for the case of 9 blade sections can be seen in Figure 5-4. This occurs for both split_types and is the result of uneven radial blade sections, i.e. (51 + 8*3)/9 = 75/9 ~8.33. Figure 5-5 gives the percent parallel efficiency of Thunder for the chosen test case and various numbers of processors. As with parallel scalability, the same sort of observations between split_types can be seen. It is interesting to note though that for the same number of radial blade sections, a split_type of one gives slightly better parallel efficiency, especially when comparing the last data point for each, which correlates to ten radial sections.

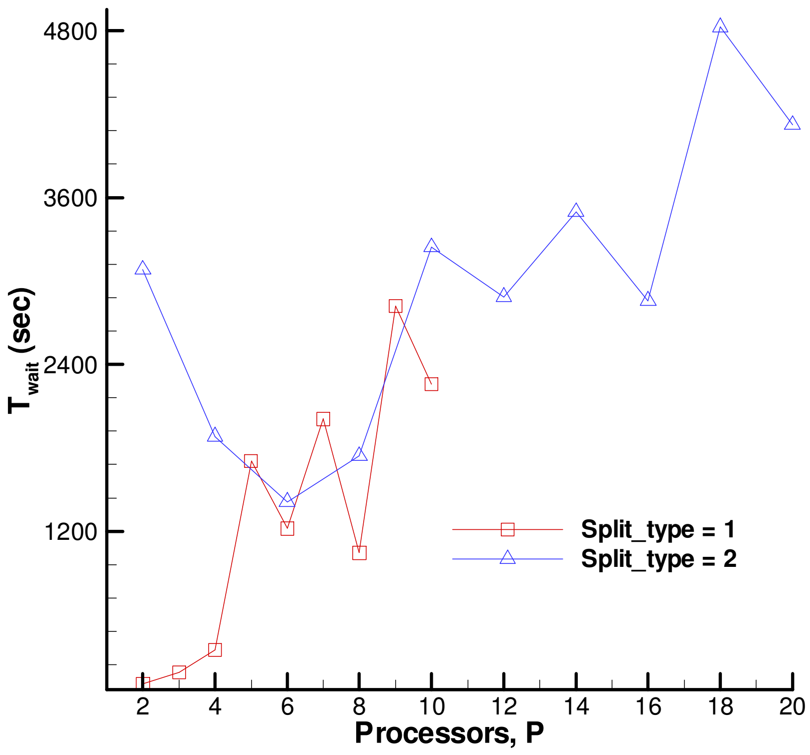

Figure 5-6. Average idle times

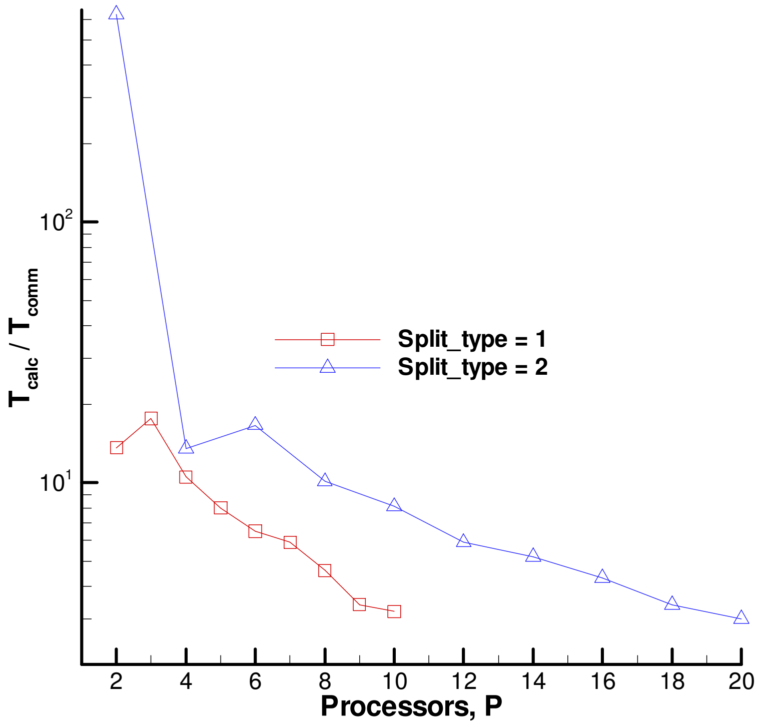

Figure 5-7. Calculation to communication times

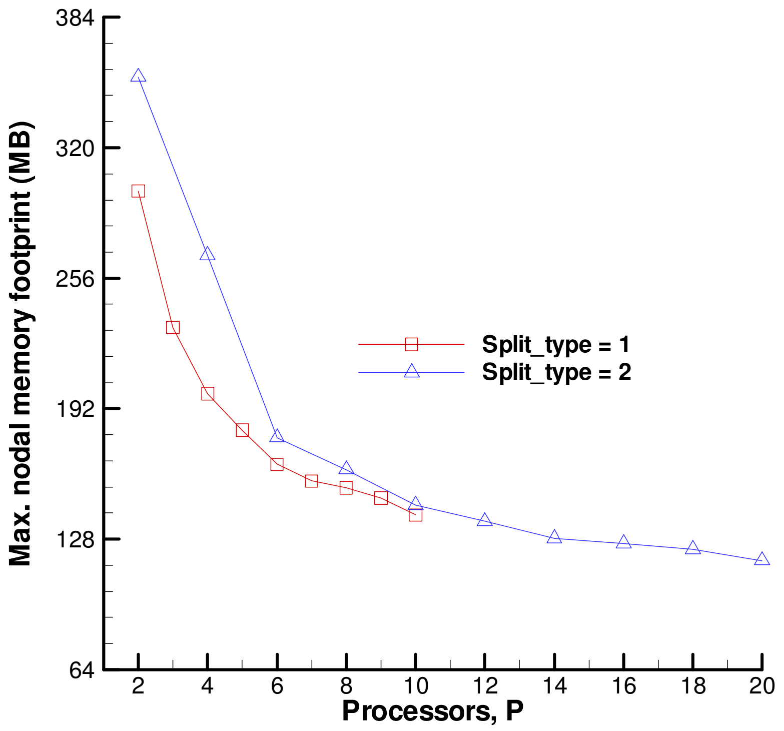

Figure 5-8. Maximum nodal memory footprint

Figure 5-6 shows the average wait time in seconds per number of processors for both split_types. This wait or idle time is a good indicator of the load balancing between nodes. Note that for a split_type of one, the wait time jumps for 5, 7, and 9 processors. These data points correlate to cases where the number of radial slices per blade section is not equal. The same can be seen for a split_type of two, i.e. 10, 14, and 18 processors. In addition, the curve for a split_type of two gives an indication of load imbalance between the O- and H-grids, even when the number of radial blade slices is equal such as the data point for two processors.

Figure 5-7 illustrates the ratio of calculation to communication time per number of processors. From these curves, it is easily seen that as more processors are added and the number of radial slices solved on each processor goes, the amount of time spent on communication remains relatively constant. In addition, the curve for a split_type of two clearly shows that the radial decomposition method chosen has a relatively large overhead, resulting from the exchange of flow variables at the ghost points. As before, splitting the O- and H-grids onto separate processors increases the ratio of calculation to communication time. Once again, this is not surprising since a split_type of two takes advantage of dividing the calculation of these two grid portions while not incurring the extra communication overhead at ghost points. Finally, both curves show that the ratio of calculation to communication time asymptotically approach a constant, where the number of 2D radial slices and load misbalancing begin to offset the communication time which is fairly constant regardless the number of processors used.

Figure 5-8 demonstrates that the goal of reducing the nodal memory footprint has been achieved. As with the other plots, the improvements are limited to a small number of processors or blade sections, in this case six blade sections which correlates to six and twelve processors for split_types of one and two respectively. Again, the curves asymptotically approach a constant, in this case roughly 128 MB, with an increase in the number of processors.

At first glance, the results of this investigation point to limited improvements from the implemented radial decomposition. However, the case used for this investigation was for a single blade with relatively equal sized O- and H-grid components. In normal use, multiple blades and blade rows would be simulated for which the radial decomposition method could be used for each blade in each blade row. Thus the performance gauged from this investigation, even for a limited number of processors, should be scalable to larger problems. Additionally, the reduction in nodal memory footprint allows for these larger problems to be solved on the same cluster, which previous to this redesign, could not be used to solve problems of such sizes. The reason such a larger problem was not used in this investigation of the parallel performance was simply due to computational resources, both in time and number of nodes required for each run. Still, the cylinder case used to test the Fluid Structure Interaction model makes use of a significantly larger problem domain, with larger grids and even three blade rows.

In conclusion, reductions in simulation runtime were achieved through a combination of code restructuring/rewriting and the addition of domain decomposition. The restructuring/rewriting of code resulted in an instant 23% overall performance gain. While the implemented domain decomposition provides an additional level of parallelism, its parallel performance substantially decreases when the ratio of ghost points (required for the decomposition) to original domain size exceeds 20%. In addition, the restructuring of the code, combined with the added domain decomposition, demonstrated a tremendous reduction in the nodal memory footprint, allowing for much larger problem domains to be solved on the same computer cluster system given enough nodes are available.

6. FLUID STRUCTURE INTERACTION MODULE

In this chapter, the Fluid Structure Interaction (FSI) module used in the developed of the aeroelastic solver is discussed. Details on the generation of the structural model, mapping between the fluid and structural grids, transfer of displacements and loads between fluid and structural models, flow of information, and time stepping are covered. In addition, differences of indexing and grid topology between the FSI module and Thunder/Corsair are given, including the conversion utilities to handle these issues.

The unsteady aeroelastic solver developed in this research is based on the idea of loosely coupling Thunder to a Computational Structural Dynamics (CSD) model. In order to keep this coupling as flexible as possible, a general FSI module [36] developed for the United States Air Force is used. The main purpose of this general FSI module is to transfer information between Thunder and the CSD model along the wetted-surface of the blade. While this may sound trivial at first, it is far from the case. Primary difficulty lies in the fundamental differences between CFD and CSD methods, namely grid topography and time stepping.

6.1 Structural Model Generation

Generation of the structural model for use with the developed aerelastic solver in this research begins with generation of the structural grid or mesh. To generate this mesh, the open source 3D finite element mesh generator gmsh [74] is utilized. The FSI module [36] includes scripts for running gmsh in batch mode, while still allowing user control over mesh quality and density. One of the inputs required by these scripts is obviously a set of coordinates to describe the structure. For simplicity, these coordinates are taken from the O-grid, specifically those making up the surface of the structure to be modeled. A utility called thunder_FSI_prep, which also handles numerous conversions and will be discussed later in this chapter, performs extraction of these coordinates into a file used by the gmsh batch scripts. The resulting mesh is then used along with another FSI module script to generate an Ansys Parametric Design Language or apdl file. Structural parameters including Young's modulus, density, Poisson's ratio, and boundary conditions along with the list of wetted surface nodes are set using this apdl file. Finally, this apdl file is converted into a structural model using Ansys®, producing database and surface files.

6.2 Mapping

The methodology used in the general FSI module follows closely to that discussed by Farhat [75]. To begin this method, the fluid/structure interface boundary (also termed the wet surface) is denoted as Γ and the following two boundary conditions are imposed:

$$\sigma_s \cdot n = -pn + \sigma_F \cdot n \tag{6-1}$$

$$\delta_s = \delta_F \tag{6-2}$$

where, δ is displacement, p is pressure, n is the normal vector, σ is the stress tensor, and the subscripts S and F denote the structural and fluid models respectively. Equation 6-1 states that the tractions on the wet surface of the structure are in equilibrium with those on the fluid side of Γ, thus the conservation of load transfer. Equation 6-2 expresses the compatibility between the displacement fields of the structure and the fluid at the fluid/structure interface, or simply the conservation of the deformation transfer. In addition, the structural and deforming fluid mesh motions are also coupled by the following continuity conditions imposed at Γ:

$$x = \delta_S \tag{6-3}$$

$$\frac{\partial x}{\partial t} = \frac{\partial \delta_s}{\partial t} \tag{6-4}$$

where *x* denotes a fluid grid point location and *t* is time. It should be noted that the formulation presented here is tailored for aeroelastic simulations. However, it also covers hydroelastic and structural acoustics vibrations along with a large class of linear and non-linear fluid/structure interaction problems. It is also assumed that the CSD model is based on Finite Element Analysis (FEA), since this approximation method has dominated the field of CSD since 1975. Conversely, no such assumptions are made about the CFD model.

Enforcing these conditions requires that a mapping be performed between the fluid grid and the structural grid at the wetted surface Γ. For this mapping, each fluid grid point or node is associated with one and only one structural element for the displacement transfer, and each structural element is associated with one or more fluid nodes for the load transfer. In the FSI module, this mapping is achieved in three passes [36]. In the first pass, an alternating digital tree search [76] is performed to locate all fluid nodes at the wetted surface that are near a given structural element. This search is fast, operating with an order of M $\log_2$M time, where M is the total number of fluid nodes at the wetted surface. A second pass comprises a point-in-polygon test which eliminates false positives (i.e. fluid nodes that are near the element but not near enough to fall within specified geometric tolerances). Finally, a third pass is made to resolve any degenerate cases of a fluid node associated with more than one structural element (produced by concavity of the structure) or associated with no structural elements (produced by convexity of the structure). Figure 6-1 illustrates an example interface between a fluid grid and a structural grid. In this example, the first pass associates fluid nodes B and C with the structural element bounded by the large volume. The second pass retains only fluid node B with the structural element bounded by the small shaded volume. Structural concavity and convexity, which produce multi- and zero associations which are resolved in the third pass, are illustrated in right portion of Figure 6-1. This mapping is a preprocessing operation which is performed only once for a given set of structural and fluid meshes.

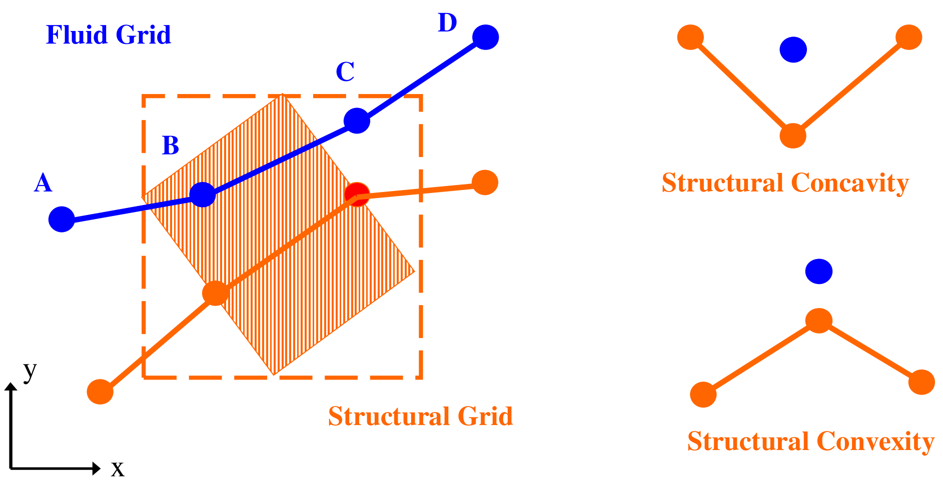

Figure 6-1. Example mapping at the interface

6.3 Displacement and Load Transfer

One means of enforcing the boundary condition in Equation 6-1 exactly is to compute the tractions on both sides of the fluid/structure interface using the same discretization method and mesh. For this research, the assumption is made that the fluid grid is finer than the structure mesh along the fluid/structure interface. Hence, the surface forces and moments induced by the fluid on the structure are calculated using the discretization method of the fluid and the geometrical support $\Gamma_F(\Gamma_S)$. This strategy guarantees that the momentum of all loads acting on the fluid/structure interface will always be equal to zero. In order to ensure that the total energy of these interface loads will also be equal to zero at all time steps, the following method is used to evaluate the forces and moments induced by the fluid on the structure.

Let $\hat{\delta}_F$ and $\hat{\delta}_S$ denote a fluid and structure admissible virtual displacement field respectively. In this case, admissible means that the traces of $\hat{\delta}_F$ and $\hat{\delta}_S$ on the fluid/structure interface are equal at the fluid/structure interface boundary. Regardless of the approximation method chosen for enforcing compatibility on the fluid/structure interface boundary between the virtual or real displacement fields of the fluid and the structure, the outcome can be formulated:

$$\hat{\delta}_{Fj} = \sum_{i=1}^{i=i_S} c_{ji}\hat{\delta}_{Si} \qquad j \in \Gamma_F, \quad i \in \Gamma_S \tag{6-5}$$

where $\hat{\delta}_{Fj}$ is the discrete value of $\hat{\delta}_F$ at the fluid point j, $\hat{\delta}_{Si}$ is the discrete value of $\hat{\delta}_S$ at the structure node i, and i_S and c_{ji} are constants that depend on the chosen method of approximation. Now consider a virtual displacement field $\hat{\delta}_F$ that is zero on each degree of freedom in the flow domain except those on the boundary Γ_F. Regardless of the discretization method used for solving the flow problem, $\hat{\delta}_F$ can be expressed as:

$$\hat{\delta}_F = \sum_{j=1}^{j=j_F} D_j\hat{\delta}_{Fj} \qquad j \in \Gamma_F \tag{6-6}$$

where D_j is a function with a local or global support on Γ_F. The virtual work on the fluid tractions acting on Γ_F can then be written as:

$$\delta W^F = \int_{\Gamma_P} (-pn + \sigma_F \cdot n)\hat{\delta}_F ds = \sum_{j=1}^{j=j_F} \int_{\Gamma_F} (-pn + \sigma_F \cdot n) D_j \hat{\delta}_{Fj} ds = \sum_{j=1}^{j=j_F} F_j \hat{\delta}_{Fj} \tag{6-7}$$

where F_j has the physical meaning of a numerical pressure flux or nodal fluid force and is given by:

$$F_j = \int_{\Gamma_F} (-pn + \sigma_F \cdot n) D_j ds \tag{6-8}$$

Substituting Equation 6-5 into Equation 6-7 leads to:

$$\delta W^F = \sum_{j=1}^{j=j_F} F_j \hat{\delta}_{Fj} = \sum_{i=1}^{i=i_S} \left(\sum_{j=1}^{j=j_F} F_j c_{ji} \right) \hat{\delta}_{Si} \tag{6-9}$$

Noting that the virtual work of the finite element structure forces and moments acting on Γ_S can be written as:

$$\delta W^S = \sum_{i=1}^{i=i_S} f_i \hat{\delta}_{Si} \tag{6-10}$$

and that the energy is conserved at the fluid/structure interface if $\delta W^F = \delta W^S$, the following is obtained:

$$f_i = \sum_{j=1}^{j=j_F} [F_j][c_{ji}] \tag{6-11}$$

Notice that the expression for f_i in the above equation does not depend on the discretization method of the structure. The term in the first bracket of Equation 6-11 depends exclusively on the discretization method of the flow solver, and the term in the second bracket depends only on the approximation method selected for enforcing the compatibility of Γ between the displacement fields of the fluid and the structure.

A natural but not necessarily mathematically optimal approximation method for enforcing Equation 6-2 is a consistent finite element based interpolation method. It's natural since the structural problem is assumed to be solved using a FEA model, and therefore the structural displacement field δ_S^e inside the wet region of an element e is given by:

$$\delta_S^e = \sum_{i=1}^{i=ie} N_i \delta_{Si} \tag{6-12}$$

where i_e denotes the total number of wet nodes belonging to element e, and N_i is the finite element shape function associated with node i of element e. Hence, in the presence of fluid and structure meshes with non-matching discrete interfaces, Equation 6-2 can be discretized by;

1. Pairing each fluid grid point S_j on Γ_F with the closest wet structural element $\Omega_S^e \in \Gamma_S$.

2. Determining the natural coordinates X_j in Ω_S^e of the fluid point S_j.

3. Interpolating δ_F inside Ω_S^e using the same shape functions N_i as in Equation 6-10, obtaining:

$$\delta_{Fj} = \delta_F(S_j) = \delta_S(X_j) = \sum_{i=1}^{i=ie} N_i(X_j)\delta_{Sj} \qquad j \in \Gamma_F, \quad i = \Gamma_S \tag{6-13}$$

From Equations 6-5 and 6-13, it follows that for a finite element approximation of the fluid/structure displacement compatibility conditions, $c_{ji} = N_i(X_j)$ and therefore:

$$f_i = \sum_{j=1}^{j=j_F} N_i(X_j) F_j \tag{6-14}$$

In the FSI module the fluid stress tensor is integrated using Gauss quadrature to determine the aero loading at a given fluid node [36]. Bilinear shape functions from finite element theory are used to evaluate the stress tensor at the Gauss points using a choice of either full or reduced integration [77]. The lower left portion of Figure 6-2 depicts nine fluid nodes (solid circles) which form four fluid cells (large squares) at the interface. In this example, the area of integration for the center node is shown bounded by dotted lines and is formed from four quadrilateral facets. The quadrilateral facets are formed from vertices located at the fluid cell face centroids, cell wall midpoints, and the fluid node of interest. By doing this, quadrilateral facets are formed independent of the polygon shape that forms the fluid cell face, permitting a single algorithm to be utilized independent of the fluid cell shape. To the upper right of Figure 6-2 is an enlargement of the upper right facet, shown with four Gauss integration points (crosses).

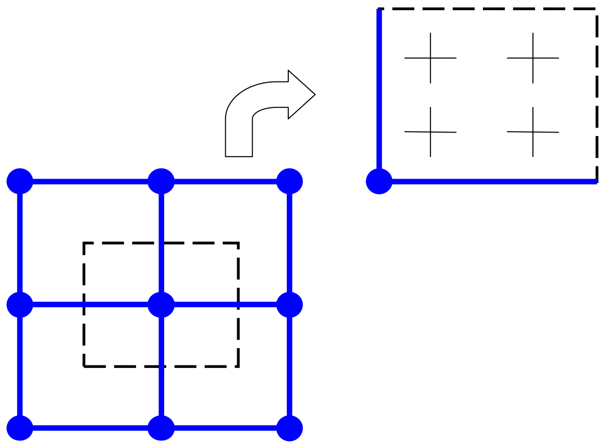
Figure 6-2. Area for Gauss quadrature

As discussed earlier, the loading of the interface fluid nodes is conservatively transferred across the interface to the structural nodes on the interface using shape functions. The FSI module employs 2-D, isoparametric shape functions based on the polygon shape of the structural element face at the interface [36]. Figure 6-3 illustrates this transfer from the fluid grid to the structural grid, where the fluid and structural nodal force vectors are F and f, respectively and is governed by Equation 6-14.

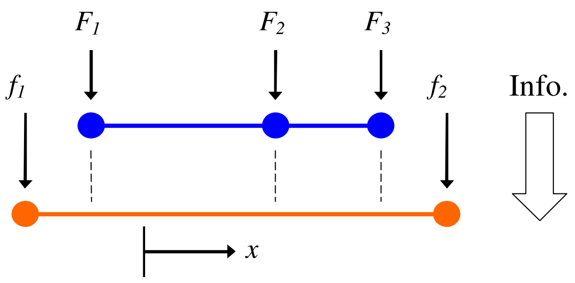

Figure 6-3. Conservative transfer of forces

The same shape functions are again used in the FSI module to transfer the computed displacements of the structural nodes lying on the interface across to the fluid nodes lying on the interface. The interpolation process is illustrated in Figure 6-4, where fluid and structural node displacement vectors δ_F and δ_S respectively.

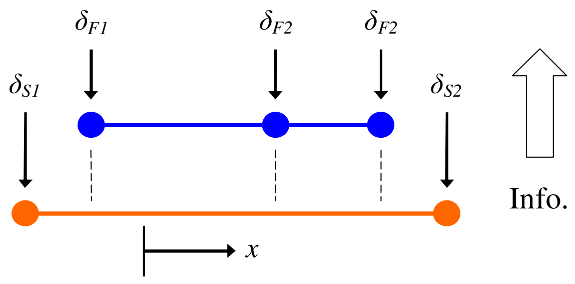

Figure 6-4. Interpolative transfer of displacements

An algebraic method for structural fluid grids is used in the FSI module to project the interface displacements smoothly into the interior of the fluid grid, deforming it so as to maintain the original grid quality, yet body-fitted to the new blade position [78]. Anchor points are defined a specified distance away from the blade. The locus of anchor points forms a closed surface within which the mesh deforms. The upper portion of Figure 6-5 depicts the locus of anchor points forming a rectangular boundary around a deforming blade shown in two positions. The method operates on lines of constant computational coordinate, beginning with the point touching the blade (cross-hatched) and ending at the anchor point. The method steps are schematically presented in the lower portion of Figure 6-5. The blade displacement is applied to all points on the line, translating the mesh line from (1) to (2). An arc length based Hermite function blends lines (1) and (2), forming the final mesh line (3).

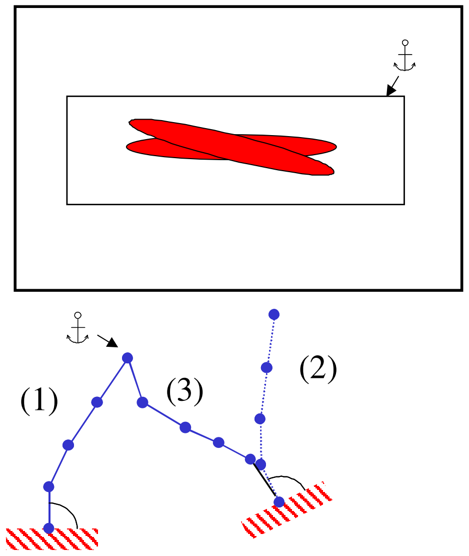

Figure 6-5. Algebraic deformation of fluid grid points

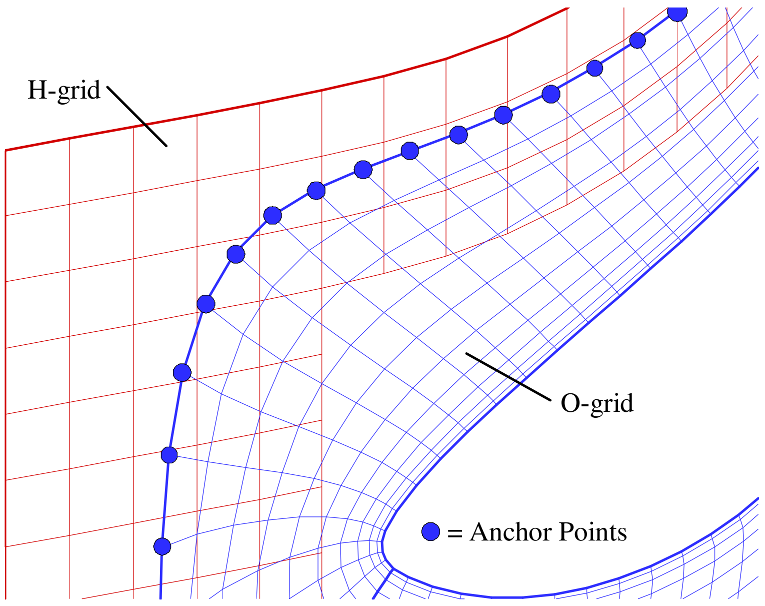

Figure 6-6. Illustration of anchor points in O-grid topography

Figure 6-6 illustrates these anchor points in terms of the O-grid topography used in Corsair/ Thunder. For this overlaid grid topography, the H-grid is held rigid along with the outer-most ring. The remaining O-grid points are then deformed by the FSI module as just described.

To reduce possible fluid grid shearing, the method was modified for applications in the blade tip region such that the anchor point is changed to a sliding point that is free to move along the shroud surface. This is accomplished by spline fitting the hub or case wall in the meridional space and projecting the displacement along the local unit tangent vector of the wall, then moving the sliding point arc length distance equal to the projected displacement. Sliding in the circumferential direction is handled similarly in azimuthal space.

6.4 Information Flow and Time Stepping

Now that a method has been developed for how to exchange information across the fluid/structure boundary, a method must now be developed for when to exchange this information. In many situations, the actual time-step sizes of the fluid and structure are quite different. The result is that many fluid time steps may need to be performed for each solid time step or vice versa. For such cases, the best approach is to use an implicit coupling with a time-staggered algorithm. A conventional serial time-staggered algorithm is shown in Figure 6-7 below, where Q is the flow solution and the arrows indicate the direction of information travel and time stepping:

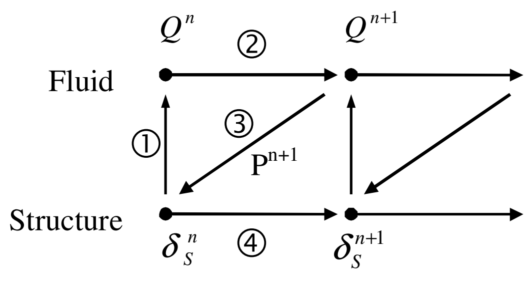

$$\delta_F^n = \delta_S^{n-1}$$

$$\delta_F^{n+1} = \delta_S^n$$

Figure 6-7. Conventional serial time-staggered algorithm

This scheme is attractive due to its simplicity. However, the scheme in Figure 6-7 is only first order time accurate, even when the underlying flow and structural solvers are second order time accurate. An equally important difficulty arises if the fluid solver uses the Geometric Conservation Law (GCL) to deal with moving grids, which Corsair / Thunder does. A sufficient condition for the GCL to be mathematically consistent is that it must exactly predict a uniform flow. It has been shown that for first and second order time accurate methods, the velocity of the deforming fluid mesh must be computed as follows in order to satisfy the CGL [44,79,80].

$$\dot{x} = \frac{x_{n+1} - x_n}{\Delta t} \tag{6-15}$$

The semi-discrete equations describing the motion of the structure are usually solved by a second order time accurate scheme in FEA models, where:

$$\dot{\delta} \neq \frac{\delta_{n+1} - \delta_n}{\Delta t} \tag{6-16}$$

It follows that if a basic partitioned procedure satisfies the GCL and the first of the continuity conditions (Equation 6-3), then it violates the second continuity condition (Equation 6-4) at the interface Γ. If $x = \delta_s$ is enforced at the fluid/structure interface and the velocity of deforming fluid mesh at the interface boundary Γ is computed using Equation 6-15, then the following holds at the interface Γ if the structural equations of motion are time integrated by a second order scheme:

$$\dot{x} = \frac{x_{n+1} - x_n}{\Delta t} = \frac{\delta_{n+1} - \delta_n}{\Delta t} \neq \dot{\delta} \tag{6-17}$$

In particular, when the conventional serial time-staggered algorithm of Figure 6-7 is used with Equation 6-15 in order to satisfy the GCL and with a second order structural time integrator, it violates the continuity of the velocity field across the fluid/structure interface Γ. Thus, under such conditions the algorithm in Figure 6-7 introduces an error in the prediction of the exchange of kinetic energy between the fluid and the structure on the boundary Γ.

To overcome some of this error, the FSI module makes use of sub-iterations to improve the synchronization between the fluid and structural grids [36], thus increasing accuracy at each time step. The number of sub-iterations is specified by the user in the input decks and in reference to Figure 6-7, would loop through the cycle 1-2-3. In addition, this error is centered about the time step used, thus the smaller the time step, the smaller the error. For the FSI module, the time step used for both Thunder and Ansys® is the same. Since Thunder requires a much smaller time step than Ansys® for convergence, mostly due to the finer grid density, this error is kept to a minimum.

The flow of information in the general FSI module is shown in Figure 6-8, where the completion of one cycle can occur once or several times per time step depending on the degree of coupling specified in the input decks [36]. In Figure 6-8, blue sections indicate fluid solver tasks (Thunder), red sections indicate tasks performed by structural solver (Ansys®), and the green sections indicate operations by the FSI module. The flow of information begins with the fluid solver, which provides the fluid stress tensor that is integrated over the wetted surface by the FSI module to yield the instantaneous aero load acting on the structure. The structural solver then converges based on these boundary conditions to produce the resulting structural displacements. These displacements at the wetted surface are then projected into the fluid mesh, thereby smoothly deforming it. The fluid solver then recalculates the metrics and Jacobian for the deformed grid and is run to convergence, thus completing one cycle.

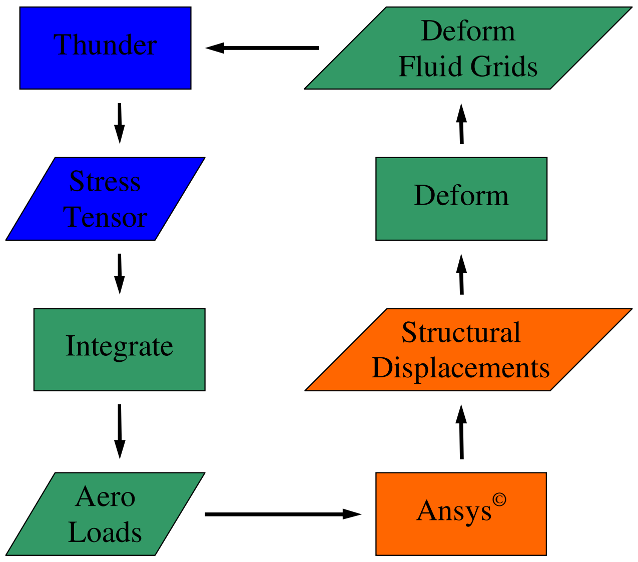

Figure 6-8. Flow of information in FSI module

The FSI module manages the flow of information between Thunder and Ansys® through the use of an internet domain, connection-oriented, server/client socket as shown in Figure 6-9. For the implementation in Thunder, a separate processor (green) is used to establish this socket with the master processor running Ansys®. This separate processor serves as a common point for collecting the stress tensors from the numerous processors used by Thunder. Additionally, this processor handles the conversion of the deformed sheared H-grid into O- and clearance grids and distributes them to the appropriate processors used by Thunder. In Figure 6-9, Ansys® is shown running on multiple processors and although Ansys® does have this capability, it will not be utilized for this research due to the limit of computational resources. In addition, since the fluid grids used by Thunder are much finer than the structural grids used by Ansys®, the vast majority of computational time is spent by Thunder and thus extra available processors are better utilized by Thunder than Ansys®.

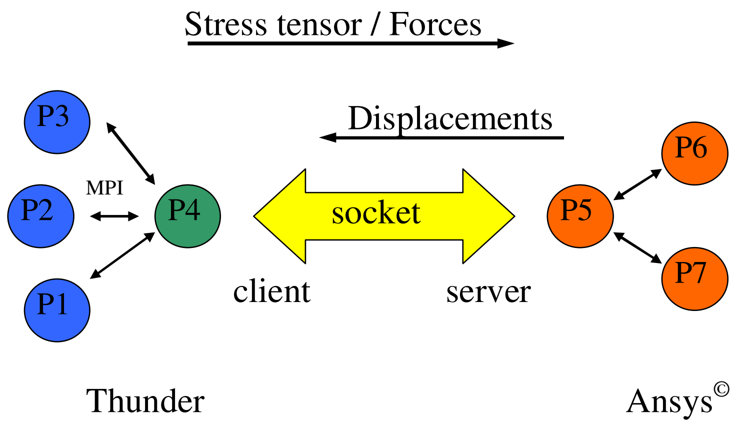

Figure 6-9. Socket communication

6.5 Conversion of O-grids to Sheared H-grids

The FSI module was specifically designed to work with the CFD solver Turbo [81]. There are several differences between the grid topography used by Thunder and that used Turbo (see Figure 6-10). For starters, Turbo uses sheared H-grids while Thunder uses an overlaid O- and H-grid topography. Second, the grids in Thunder are centered about the blades while in Turbo, they are centered about the passage between blades. In order to use the FSI module, an algorithm was developed to morph the blade centered O-grids from Thunder into passage based sheared H-grids and vice versa. This algorithm also takes into account the associated deformation of the clearance grid, if present, based on the inner O-grid deformation. The major issue in handling the clearance grid is that for a sheared H-grid, the number of points in the circumferential direction is the same regardless of a tip clearance. However in Thunder, the clearance grid adds a substantial number of points or rings in the circumferential direction. In addition, the FSI module also makes extensive use of GU files from Turbo, which contain information about the grids and their decomposition. Thus a utility was developed to create these GU files, along with files to help in generation of the structural grid via gmesh and weighted distances to handle recreation of the clearance grid. Lastly, Turbo uses a somewhat different grid index, where *j* and *k* have been flipped when compared with Thunder. This too is handled by the utility program, called thunder_FSI_prep.

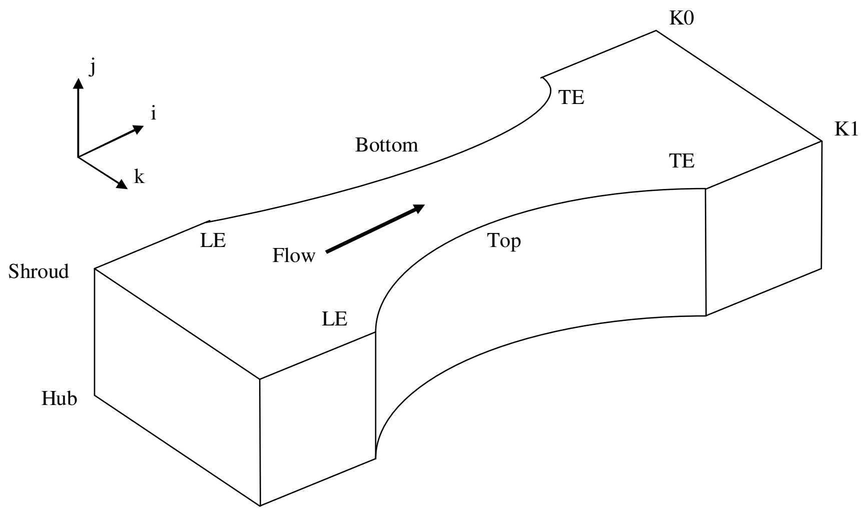

Figure 6-10. Turbo sheared H-grid topography

Conversion of the O-grids begins with grid generation. To ensure that the O-grid can be split into an upper and lower passage section, each with an equal number of grid points, the O-grid must initially be generated with an odd number of circumferential points. The reason for this is because the first and last grid points in the circumferential direction (around the blade surface) overlap. Since the clearance grid, if present, is generated using this same number of circumferential points, no special attention to its size is required at this stage. Next, thunder_FSI_prep is used to transform the O-grids into primitive sheared passage H-grids by splitting them about their leading and trailing edge points. The leading edge of the blade is first calculated based on the minimum axial value. If desired though, the index of the leading edge point can be entered in the input deck to thunder_FSI_prep, otherwise it is calculated automatically as just described. The trailing edge is then calculated to be half the circumferential points away from the leading edge. While this trailing edge point is often somewhat off from the real trailing edge due to differences in the number of points on the top and bottom of the airfoil surface as a result of clustering, it does meet the requirement for splitting the O-grid up evenly. Finally, the last upper half is rotated down by the period of blade passages being modeled, as illustrated in Figure 6-11.

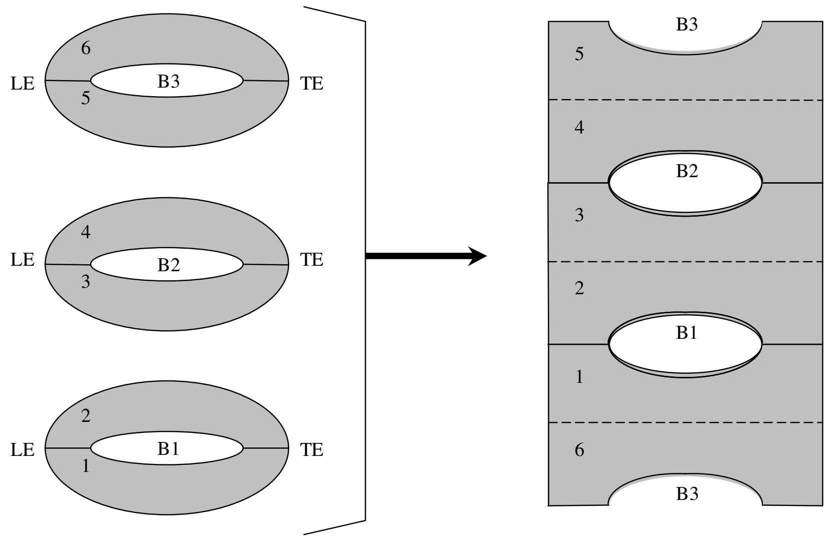

Figure 6-11. Conversion from O- to sheared H-grids

When a clearance grid is present, a simple modification is required to the previous method. The inner most O-grid "ring" is replaced with the points from the collapsed centerline of the clearance grid for radial slices where the tip clearance exists. In addition, an auxiliary file is created with the weighted distances from the collapsed centerline of the clearance grid to the next to inner most O-grid ring. This is used during the simulation to recreate the clearance grid from the deformed sheared H-grid.

In Thunder, the sheared H-grids are read from file at the start of an FSI run and held in memory after each call to and from the FSI module, while the O-grids, and clearance grids if present, are regenerated from the sheared H-grids. A check to make sure the grids are not being folded on top of one another is also made after each "re-generation" of the O- and clearance grids is performed. This is done by checking the Jacobians, which must be recalculated anyway, to see if any are negative. A negative Jacobian indicates the grid has become folded on top of itself and the execution of Thunder is thus aborted after dumping appropriate debugging information to the output decks. The subroutines in Thunder for conversion to sheared H-grids is called mutate, while conversion back to O- and clearance grids is called purify.

In this chapter, the Fluid Structure Interaction (FSI) module used in the developed of the aeroelastic solver was discussed. Details on the generation of the structural model, mapping between the fluid and structural grids, transfer of displacements and loads between fluid and structural models, flow of information, and time stepping were covered. In addition, differences of indexing and grid topology between the FSI module and Thunder/Corsair were given, including conversion utilities to handle these issues.

7. RESULTS

To test the aeroelastic solver developed in this research, two simplified geometries are used. The well understood case of a flexible cylinder is cross flow is studied. However, before performing the full FSI simulation of the flexible cylinder, a rigid cylinder is first simulated to ensure the flow solver Thunder is capable of accurately predicting the periodic shedding of wakes, also known as Von Karman streets, which are known to exist for such a configuration [51]. Once the correct wake shedding frequency for the rigid cylinder has been achieved, the FSI module is turned on with the resonate frequency of the cylinder set to the alternating wake shedding frequency. This results in the self excited aeroelastic behavior of a flexible cylinder in cross flow being obtained. By achieving a self excited and stable oscillation, the exchange of energy between the fluid and structure is demonstrated and thus the validity of the aeroelastic solver. Another test case studied in this chapter involves the response of a fourth standard configuration turbine blade to a step function impulse from zero loading to the converged flow solution loading. This results in the excitation of the major vibrational modes of the turbine blade, which are then compared to those obtained from an in vacuo solution using Ansys®.

7.1 Rigid Cylinder

The simulation of a circular cylinder in cross flow is fundamental in the study of both CFD and aeroelasticity [51]. In cross flow of the appropriate Reynolds number, a circular cylinder will shed alternating swirling vortexes in a periodic fashion. This phenomenon is known as the Von Karman vortex streets and is responsible for such things as the singing of suspended power cables (know as galloping flutter) and even the failure of the Tacoma Narrows Bridge [82]. The periodic shedding of swirling vortexes induces alternating forces on the cylinder, resulting in Vortex Induced Vibration (VIV). For a flexible cylinder, VIV will cause the cylinder to oscillate in a harmonic motion. This is one of the primary reasons it has become a fundamental test case for aeroelastic solvers. Such a test case is also applicable to turbomachinery, where vortex shedding can lead to flutter and other aeroelastic behavior [83,84].

For testing the FSI model developed in this research, a rigid cylinder with no FSI will first be simulated to verify the CFD model can reproduce the Von Karman vortex streets at the proper frequency for the associated Reynolds number. Once this is accomplished, the simulation is continued using FSI for a flexible cylinder with a natural frequency equal to the shedding frequency of the Von Karman vortex streets. This case is ideal for testing the FSI model, not only due to the well know nature of the Von Karman streets, but because the oscillation of the cylinder is self exciting, thus visually proving the interaction between the fluid and structural dynamics.

The alternating vortex shedding frequency associated with Von Karman vortex streets obeys the following formulae [51]:

$$\frac{fd}{V} = 0.198\left(1 - \frac{19.7}{\mathrm{Re}}\right) \tag{7-1}$$

where f is the frequency in Hz of alternating vortices shed, d is the diameter of the cylinder, V is the steady velocity upstream of the cylinder, and Re is the Reynolds number relative to the cylinder:

$$\mathrm{Re} = \frac{\rho V d}{\mu} \tag{7-2}$$

with ρ and μ being the density and dynamic viscosity of the fluid respectively. Equation 7-1 generally holds true for $150 < \mathrm{Re} < 10^5$. The dimensionless parameter which makes up the left half of Equation 7-1 is known as the Strouhal number, abbreviated as *St*, and is used to describe oscillating flow mechanisms [85]. While the Von Karman streets exist in flow with a cylinder Reynolds number of up to 10^7, the shedding becomes less periodic after a cylinder Reynolds number of ~200 due to turbulent flow [86].

To model the Von Karman streets, a cylinder 1/8 inch in diameter with a length of 18 inches was simulated in a channel. Since thunder is designed for turbomachinery, a somewhat large radius annular section from 234.5 inches at the hub to 252.5 inches at the shroud, with 720 periodic sections was used to model the channel. This resulted in a channel with relatively flat hub and shroud sections. Figure 7-1 shows the grid at midspan for the channel modeled. The boundary condition at the hub and shroud were set to Euler slip conditions and the left and right boundaries were left as periodic. The H-grid is 165x120x51 points, while the O-grid is 301x121x51 points in the i, j, and k directions respectively. To initiate shedding, the O-grid around the cylinder was deliberately unbalanced using clustering, with roughly 20% more grid points on the upper surface than the lower surface. Since the numerical method in Thunder can be somewhat dissipative, a very fine grid was created around the cylinder, as shown in Figure 7-2. While most computational simulations of the Von Karman streets around cylinders extend the high grid density for several cylinder diameters downstream [83,86], it was not done here for two primary reasons. First, extending the passage behind the cylinder with a high density grid would dramatically increase the simulation runtime, since as discussed in chapter 5, the runtime is proportional to the total number of grid points used in the simulation. Second, only the forces on the cylinder are of interest for this test.

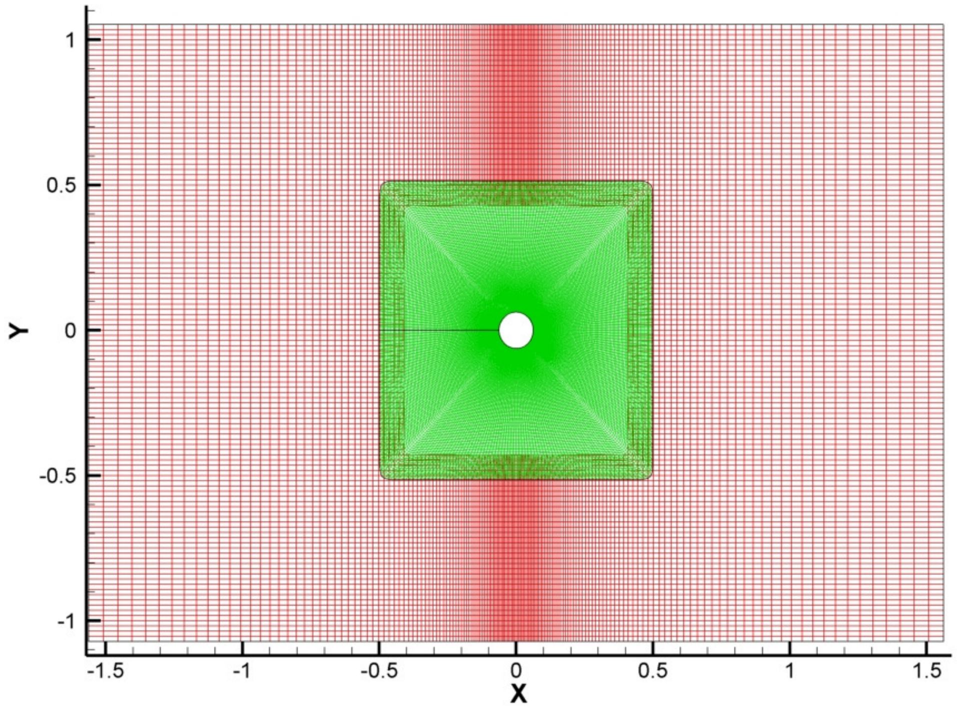

Figure 7-1. 2D midspan slice of channel and cylinder grids

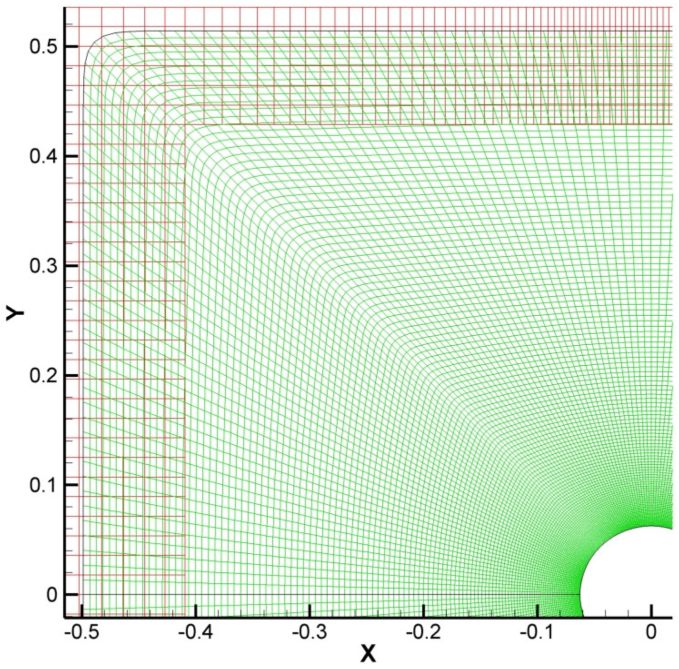

Figure 7-2. Close-up of O-grid around the cylinder

A target Reynolds number for the cylinder of 180 was used, resulting in a free-stream velocity of ~2.73 ft/s. The remaining free-stream variables were taken as standard day conditions. Using Equations 7-1 and 7-2, the predicted frequency of alternating vortices for this case is 46.21 Hz. Figure 7-3 is a plot of the RMS residuals, which show the convergence of the simulation.

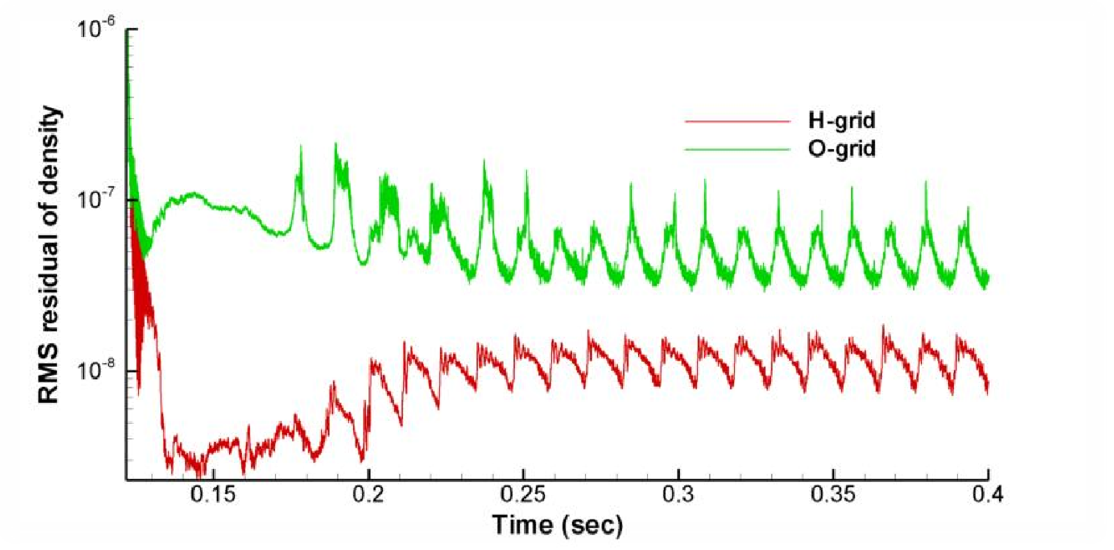

Figure 7-3. Convergence history for rigid cylinder simulation

Note that the periodic shedding of wakes is evident in the plot and thus demonstrates a periodic converged solution has been achieved. Figure 7-4 shows a time trace of the alternating transverse forces on the cylinder at midspan. To determine the frequency of these alternating vortices and the associated Strouhal number, this time trace was run through an FFT, the result of which are shown in Figure 7-5. Closer examination of the FFT results shows a frequency spike at 46.17 Hz, which is within the FFT resolution of 2.88 Hz to the predicted 46.21 Hz. The associated Strouhal number, calculated using Equation 7-1, is 0.176.

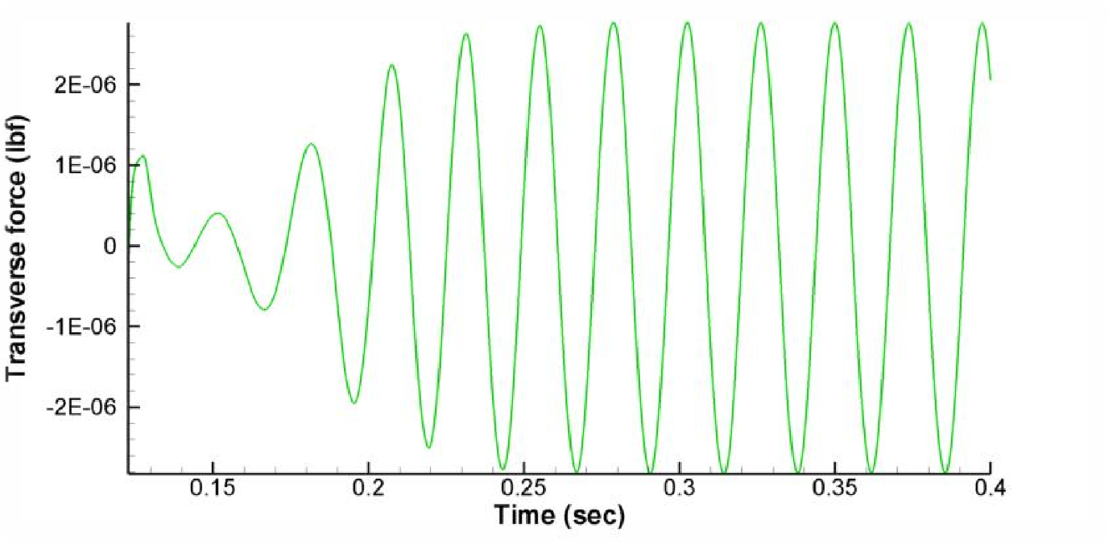

Figure 7-4. Time trace of transverse forces on cylinder at midspan

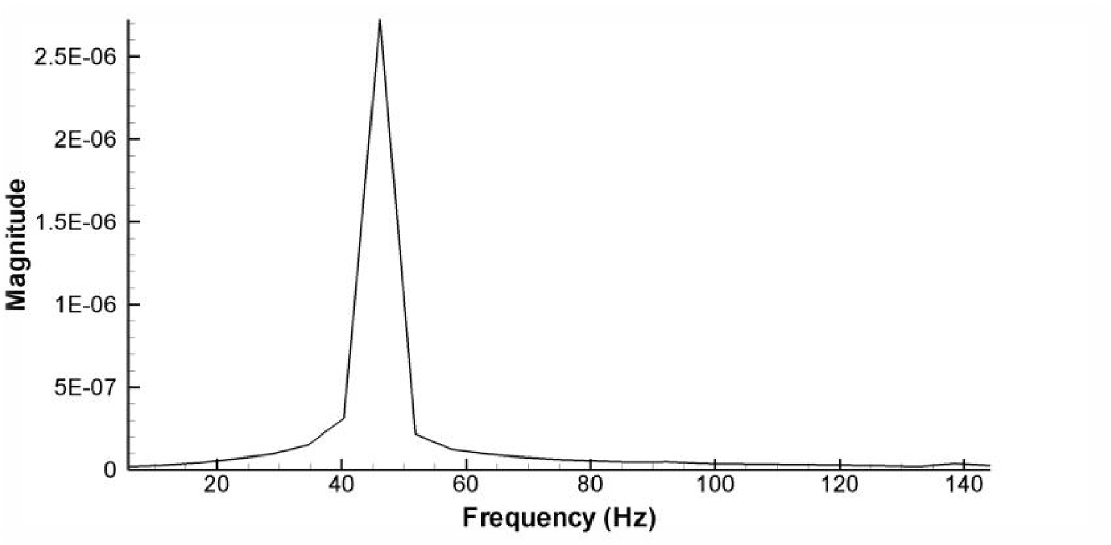

Figure 7-5. FFT of transverse forces on cylinder at midspan

7.2 Flexible Cylinder with FSI

To test the aeroelastic solver developed in this research, the previous cylinder case is continued from a restart files, but with FSI active and the structural properties of the cylinder set such that the natural (or resonant) frequency of the cylinder is the same as the alternating vortex shedding frequency of the Von Karman streets. Two additional important steps were taken with respect to this restart. First, the unbalanced clustering of grid points around the cylinder was removed to eliminate any error or lopped sidedness in the forces and displacement. Second, the simulation was restarted from a time in the solution where the forces on the cylinder were as close to zero as possible, to help reduce any impulse effects in the structural model which might result from an instant loading.

The natural frequency of a slender beam in transverse vibration clamped at both ends is given by [87]:

$$2\pi f_n = \beta_n^2 \sqrt{\frac{EI}{\rho A}} \tag{7-3}$$

where *n* is the mode shape index, *E* is the young's modulus of elasticity, *I* is the mass moment of inertia, ρ is the density, *A* is the cross sectional area, and β_n is the weighted natural frequency per mode shape defined as:

$$\begin{aligned} \beta_1 l &= 4.73004074 \\ \beta_2 l &= 7.85320462 \\ \beta_3 l &= 10.9956079 \\ \beta_4 l &= 14.1371655 \\ \beta_5 l &= 17.2787597 \\ \beta_n l &= \frac{(2n+1)\pi}{2} \quad \text{for} \quad n > 5 \end{aligned} \tag{7-4}$$

with *l* being the length of the beam. The mode shapes of vibration for the slender beam clamped at both ends are given by:

$$y(x) = A_\lambda \left[\cosh \beta_n x - \cos \beta_n x - \sigma_n (\sinh \beta_n x - \sin \beta_n x)\right] \tag{7-5}$$

In Equation 7-5, A_λ is the arbitrary magnitude of the eigenvalues, *x* is the distance from the clamped end, and σ_n is the mode shape coefficient defined as:

$$\sigma_n = \frac{\cosh \beta_n l - \cos \beta_n l}{\sinh \beta_n l - \sin \beta_n l} \tag{7-6}$$

Figure 7-6 shows the first three mode shapes for the cylinder used in this research with both ends clamped.

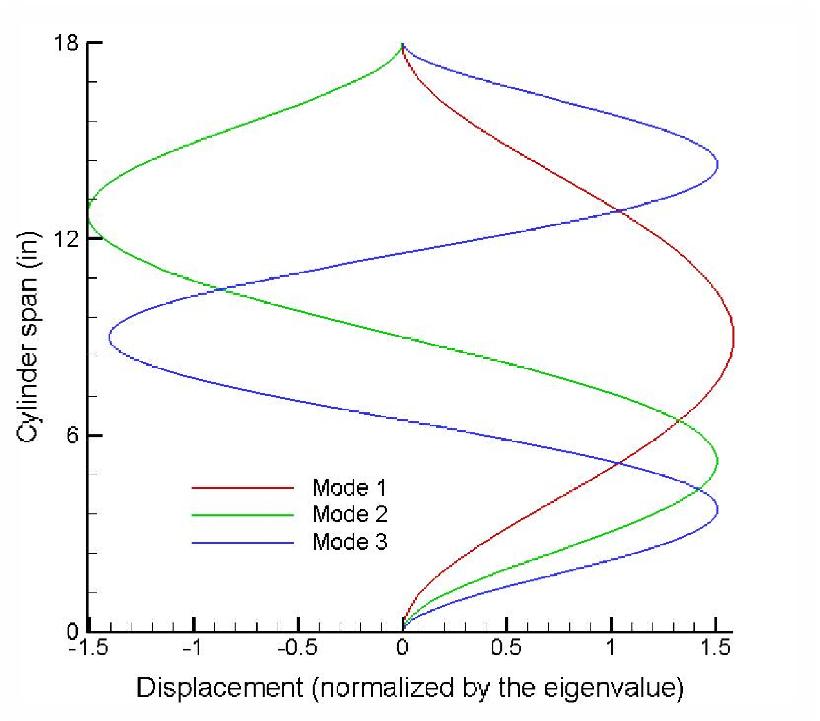

Figure 7-6. First three mode shapes for the clamped-clamped cylinder

For a circular cylinder, the cross sectional area and mass moment of inertia are:

$$A = \pi r^2 \qquad I = \frac{\pi r^4}{4} \tag{7-7}$$

Substitution these into Equation 7-3 and rearranging:

$$2\pi f_n = \beta_n^2\sqrt{\frac{EI}{\rho A}} = \beta_n^2\sqrt{\frac{E\pi r^4}{4\rho\left(\pi r^2\right)}} \tag{7-8}$$

$$\Rightarrow \frac{2\pi f_n}{\beta_n^2} = \sqrt{\frac{Er^2}{4\rho}}$$

$$\Rightarrow \frac{4\pi^2 f_n^2}{\beta_n^4} = \frac{Er^2}{4\rho}$$

$$\Rightarrow \frac{E}{\rho} = \frac{16\pi^2 f_n^2}{r^2\beta_n^4}$$

Note that Equation 7-8 results in a ratio between the Young's elastic modulus and density of the cylinder. This is fortuitous, as these are two of the three structural property parameters required for the CSD model, the third parameter being Poisson's ratio.

To obtain a structural model of the cylinder with the desired resonance, the Young's modulus was taken as 30.0E6 psi (roughly that of steel [88]) and Equation 7-8 was used to calculate the required density, which for the current case is 1.658E-3 lbf-s^2/in^4. From experience with the rigid cylinder, a time step of 4.684E-6 seconds was used to ensure both the vortex shedding frequency of the cylinder was accurately captured and the flow solver remained stable. It is important to note that while the rigid cylinder simulation from the previous section was entirely two dimensional in nature, this simulation becomes three dimensional upon deformation of the cylinder, as indicated by the mode shapes in Figure 7-6.

A time trace of the cylinder displacement at midspan in both axial and transverse directions is shown in Figure 7-7. From this figure, the self excited oscillating nature of the cylinder is clearly seen, visually demonstrating the exchange of energy between the fluid and structural models.

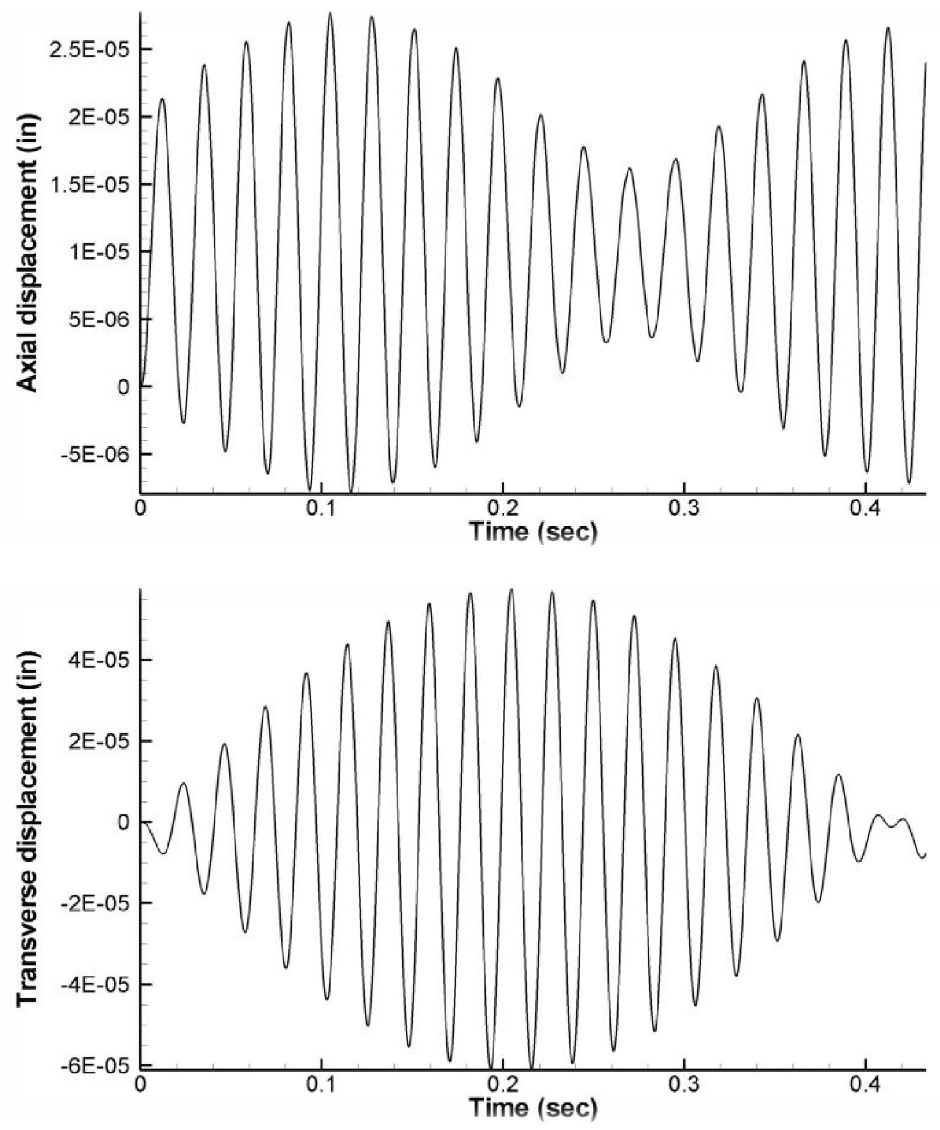

Figure 7-7. Cylinder displacement at midspan

However instead of the Von Karman street frequency, Figure 7-7 shows a beat frequency. Further interrogation of the displacement time traces through an FFT (Figure 7-8) revealed even more peculiarities. First, the high frequencies in the axial and transverse displacements show a peak at 43.85 Hz with a resolution of 2.3 Hz.

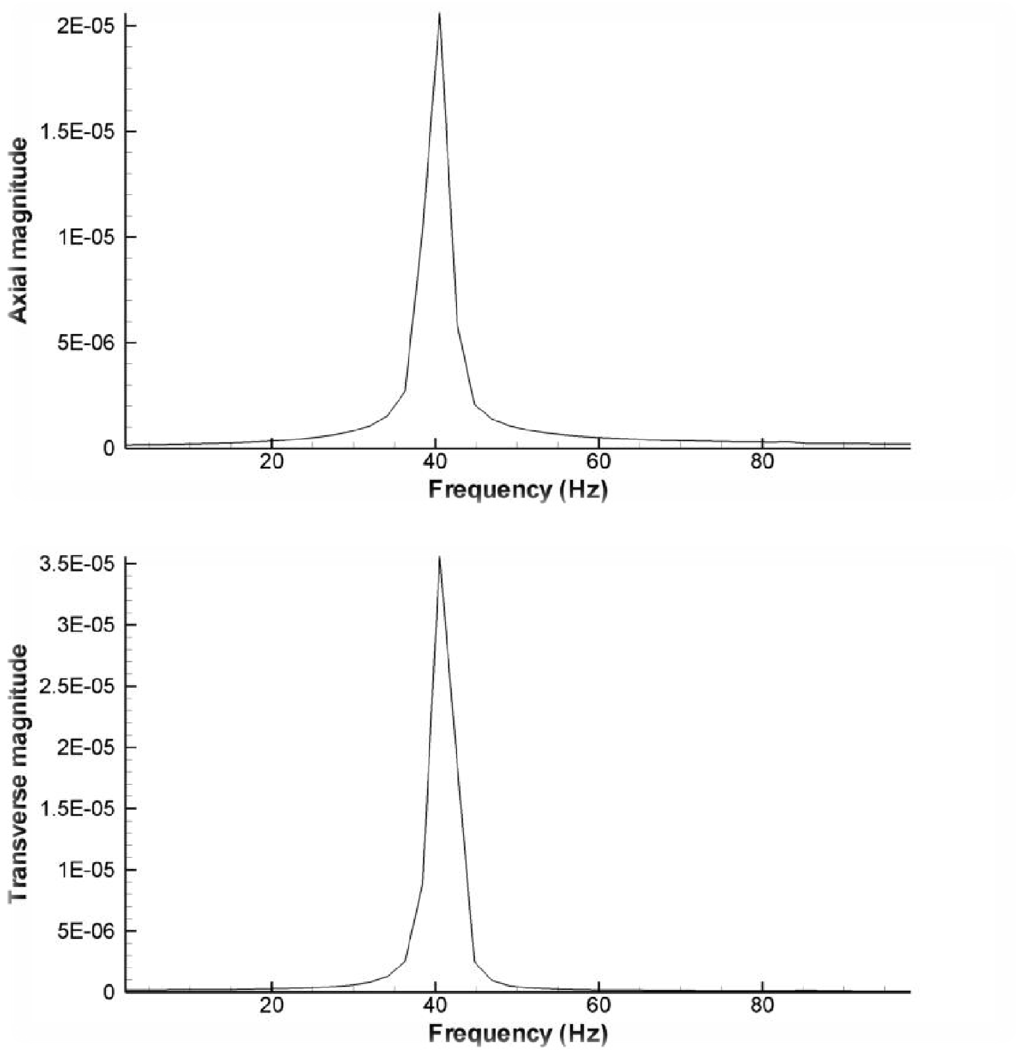

Figure 7-8. FFT of transverse and axial displacements at midspan

These problems were traced back to the structural model after an in vacuo modal analysis of the structural model was performed in Ansys®. First, the calculated vibrational modes for the axial and transverse directions were discovered to be different, specifically 42.6 Hz and 43.74 Hz respectively. This was further traced to an issue with pivot points used in the gmsh script to generate the original structural mesh. After a slight change in the grid index points used for pivots in the gmsh script, the vibrational modes for the axial and transverse directions calculated using Ansys® were 43.15 Hz and

43.21 Hz respectively. Further changes in the grid index points used for the pivots did not yield any improvement over this.

Secondly, it was realized that Equation 7-8, derived for a circular cross section, could not be used to calculate the require density for the structural model. The reason for this is because the structural model, due to the brick elements used in the mesh, has an octagonal cross section as shown in Figure 7-9. Thus the mass moment of inertia and cross section area are different from those used to simplify Equation 7-8. Using linear interpolation and a bit of trial and error, the correct density for the structural model to achieve a resonance frequency of 46.2 Hz is 1.86E-3 lbf-s^2/in^4.

Using this insight, the beat frequencies observed in Figure 7-7 is the result of the resonance frequency being very close to the driving frequency of Von Karman streets [87]. In fact a quick calculation of one half the sum of the resonance and driving frequency, 44.4 Hz for the axial and 44.97 Hz for the transverse, shows good agreement respectively with the high frequencies detected by the FFT. Similarly, the low frequencies evident in the Figure 7-7 can be calculated as one half the difference between the driving and resonance frequency, or 1.8 Hz for the axial and 1.23 Hz for the transverse. While a longer time trace is required to verify these frequencies accurately using an FFT, visual approximation of Figure 7-7 is in agreement with the general range of these values.

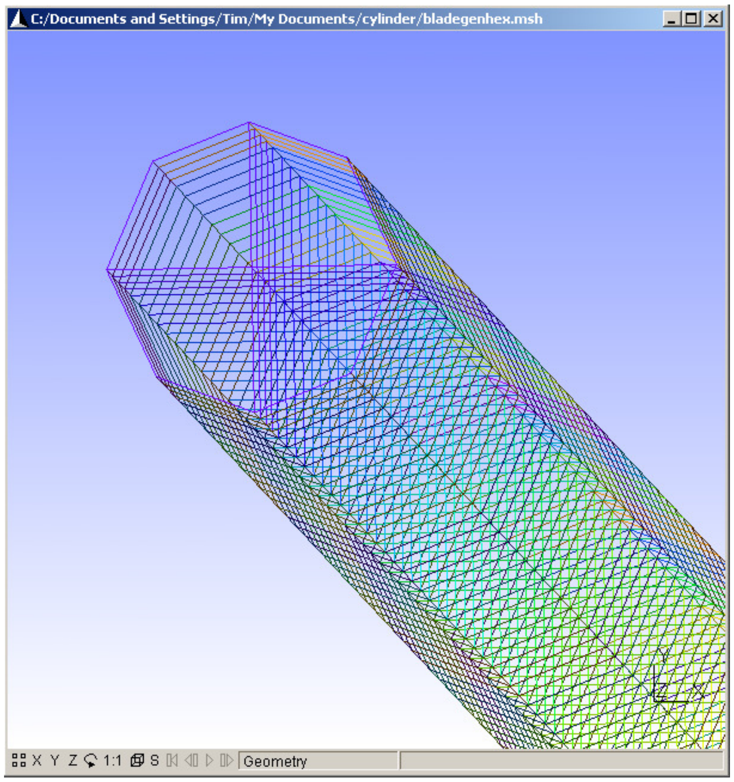
C:/Documents and Settings/Tim/My Documents/cylinder/bladegenhex.msh
X Y Z 1:1 S
Geometry

Figure 7-9. Structural mesh for the flexible cylinder

7.3 Fourth Standard Modal Analysis

The second test case used is based on the fourth standard configuration and demonstrates the ability of the aeroelastic solver to predict the dominant vibrational modes of an aeroelastic turbomachinery blade. For this case, a single blade from the fourth standard configuration is subjected to a step function from zero loading to the converged flow solution loading in order to excite the structural modes of the blade. For the structural model, a Young's modulus of 29.0E-6 psi, density of 7.25 lbf-s^2/in^4, and Poisson's ratio of 0.3 were used. Although the blade tested at the Ecole Polytechnique Federale de Lausanne was mounted on a spring hub [64], the structural blade modeled here is clamped at the hub. Figure 7-10 shows the structural mesh used for this simulation.

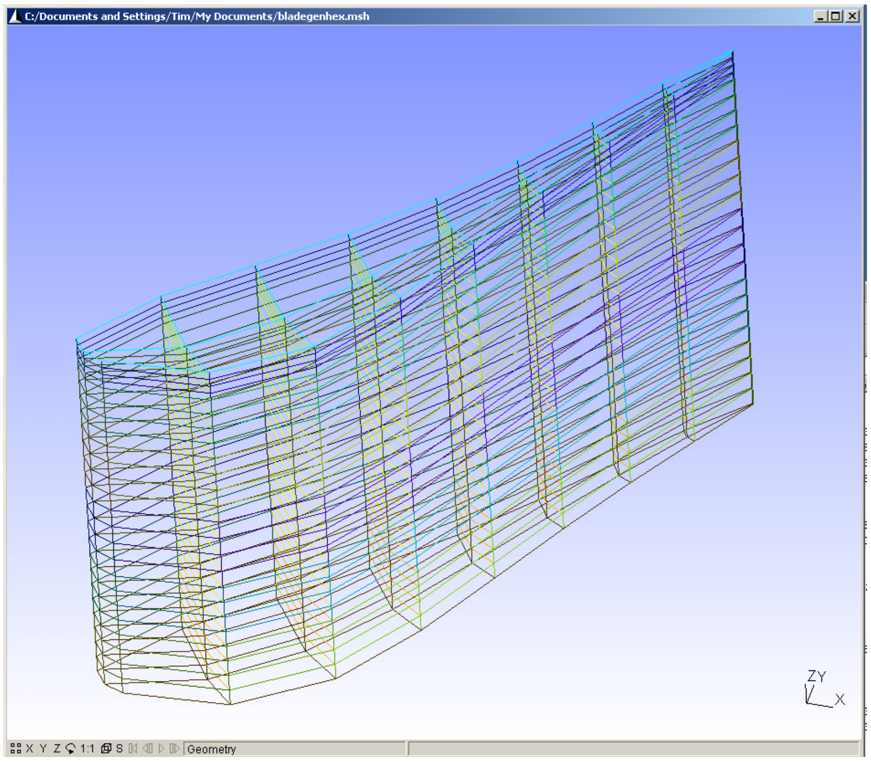

Figure 7-10. Structural mesh for STCF4

To extract the vibrational frequencies from the simulation, a time trace of the displacements at the trailing edge tip of the blade were fed through an FFT. This location was chosen since the displacements were higher at this location than any other location on the blade during the simulation. Figure 7-11 shows a time trace of the axial displacements at this location. Though the axial or circumferential directions could have been used for this, the axial direction showed slightly higher displacements; hence it was used for the FFT which is shown in Figure 7-12. Due to the time step size used in the simulation and the rather short time trace obtained, the resolution (or increments in the scale) of the FFT is 273.6 Hz.

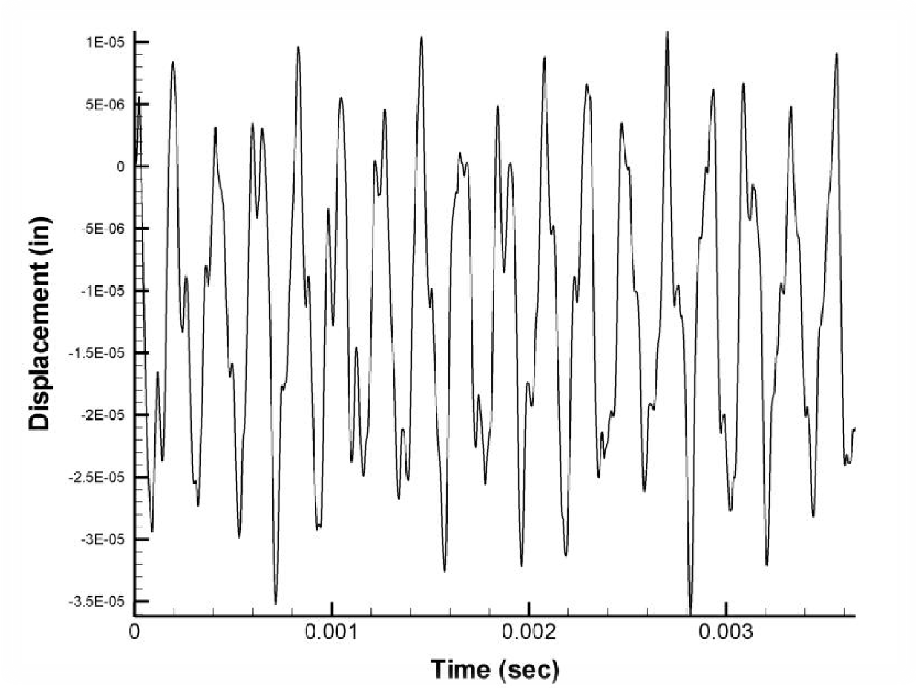

Figure 7-11. Time trace of axial displacement at TE tip

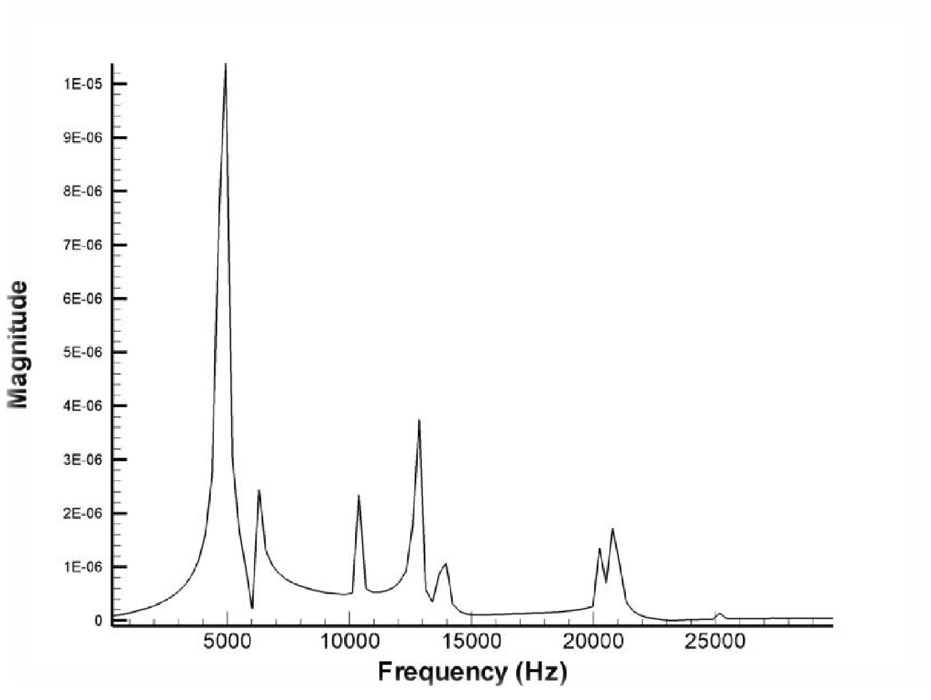

Figure 7-12. FFT of axial displacement at TE tip

Table 7-13 gives the first 8 vibrational mode frequencies for the fourth standard configuration turbine blade. The Ansys® results are from an in vacuo analysis using the Block Lauczos method, while the Thunder/FSI results are from the displacement time trace at the trailing edge tip of the blade.

Mode	Frequency (Ansys®)	Frequency (Thunder/FSI)
1	4796.2 Hz	4924.25 Hz
2	6145.4 Hz	6292.10 Hz
3	10,373 Hz	10,395.64 Hz
4	12,669 Hz	12,857.77 Hz
5	13,871 Hz	13,952.04 Hz
6	20,317 Hz	20,244.14 Hz
7	20,756 Hz	20,791.27 Hz
8	24,942 Hz	25,168.39 Hz

Table 7-1. STCF4 frequency spectrum

Table 7-1 shows very good agreement between the modal frequencies predicted by Ansys® and those by the unsteady aeroelastic solver, especially considering the resolution of the FFT. By accurately capturing the modal frequencies in the displacement of the fluid grid, it is reasoned that the aeroelastic solver is properly orchestrating the interaction of the coupled fluid and structure domains, providing a time accurate simulation of the aeroelastic system modeled.

In this chapter, the developed unsteady aerelastic solver was tested using two simplified configurations. The first configuration, that of a flexible cylinder in cross flow, demonstrated the exchange of energy between the fluid and structural models. Although the intended resonance of the cylinder was not achieved do to subtle errors in creation of the structural model, the cylinder was self excited and reached a periodic beat frequency. The second configuration involved capturing the vibrational modes of a fourth standard configuration turbine blade, through use of a step function from zero loading to the converged flow field loading. The results of this test illustrated the ability of the aerelastic solver to accurately predict the vibrational modes of the turbine blade. By doing so, the aeroelastic solver has demonstrated it is properly orchestrating the interaction between the fluid and structural domains and capable of providing a time accurate simulation of a modeled aeroelastic system.

8. SUMMARY AND CONCLUSIONS

In this research, an unsteady aeroelastic solver design tool for turbomachinery applications was created by loosely coupling an improved version of the turbomachinery CFD solver Corsair, called Thunder, to the structural solver Ansys® through use the of a general FSI module. Several modifications to Corsair were made during this research, resulting in the improved flow solver called Thunder.

In order to perform the necessary modifications to Corsair required for this research, a detailed understanding of the numerical methods used in Corsair was required. Since such detailed documentation of Corsair did not exist, the source code was painstakingly examined and documented in chapter 2.

To properly handle grid deformations, an investigation into different numerical methods for evaluation of both spatial and temporal coordinate transformation terms known as metrics was performed in chapter 3. From this investigation, it was determined that the Finite Volume method with Long Diagonals produced the least amount of numerical error on a three dimensional deforming grid while requiring a reasonable number of floating point operations. Thus the Finite Volume method with Long Diagonals was integrated into Corsair/Thunder and used for the remainder of this research.

Another area of improvement required for use in the targeted, time limited, design environment was a reduction in simulation runtime. This was achieved through three main efforts. The first involved replacement of the gridding-to-wall feature in Corsair with a wall function, as detailed in chapter 4. To test the implementation of the wall function, the high subsonic flow around a fourth standard configuration turbine blade was simulated and compared to results from use of the gridding-to-wall method. In addition to a dramatic reduction of the runtime, a noticeable increase in stability and convergence was also observed through reduction in the time step required.

Still a further reduction in simulation runtime was achieved through the use of parallel computing and domain decomposition in the radial direction as outlined in chapter 5. To simplify the use of the domain decomposition, a utility called thsplit was created to both automate and optimize the decomposition procedure based on only the number of the divisions to make for each grid. This effort also resulted in a major change of Corsair's data structure and a rewrite of the source code, resulting in Thunder. Changes to the data structure were made to reduce the nodal memory footprint and allow larger problem domains to be solved. Runtime improvements from these changes in data structure and rewrite of the code alone were demonstrated to be roughly 23%! Parallel efficiency of the added radial decomposition was shown to be effective for modest numbers of domain divisions, but beyond a ratio of additional ghost points to original domain size of ~20%, efficiency dramatically decreased. For the single fourth standard configuration turbine blade used to evaluate these changes, this translated to a fivefold reduction in runtime and a 33% reduction in the nodal memory footprint when six processors were used, while obtaining a parallel efficiency of greater than 85%!

Chapter 6 covered the FSI module and it's integration with Thunder. Differences in grid indexing between the FSI module and Thunder were overcome through the creation of conversion utilities and algorithms. The resulting unsteady aerelastic solver was tested against two simplified geometries in chapter 7.

First in section 7.2, the well understood case of a flexible cylinder in cross flow was studied with the natural frequency of the cylinder set to the shedding frequency of the Von Karman streets. The cylinder was self excited and thus demonstrates the exchange of energy between fluid and structural models. However, the intended resonance frequency was not achieved due to a poor assumption regarding the cross sectional properties of the structural model. This resulted in the displacement of the cylinder exhibiting a beat frequency, indicating that the driving force frequency of the Von Karman streets is very close to the resonance frequency of the structure.

In section 7.3, a second test case based on the fourth standard configuration was used to demonstrate the ability of the solver to predict the dominant vibrational modes of an aeroelastic turbomachinery blade. For this case, a single blade from the fourth standard configuration was subjected to a step function from zero loading to the converged flow solution loading in order to excite the structural modes of the blade. To extract these vibrational frequencies, a time trace from the trailing edge tip point of the blade was passed through an FFT. The resulting frequencies were then compared to those obtained from an in vacuo analysis using Ansys®, with good agreement between the two.

8.1 Suggested Additional Tests & Case Studies

There is always a need to further test computational tools through additional case studies and the unsteady aerelastic solver developed in this research is no exception. The test cases used in this research were chosen for their simplicity and ability to demonstrate the fundamental requirements of this tool.

An obvious area of suggested additional cases is experimental studies performed on aerelastic phenomena in turbomachinery. Such experimental studies are desperately needed in the public domain to test aeroelastic solvers for turbomachinery application. While a small number of such experimental studies have been conducted, the results have been deemed proprietary by the investigators and thus are not within the public domain. The fourth standard configuration turbine blade used in this research comes close to the requirement of experimental data. Unfortunately, this study relied on mechanical forcing of the blades to simulate aeroelastic behavior of the turbine, resulting in nonrealistic data for testing of modern computational aerelastic solvers.

A second area of suggested test cases and study with this aeroelastic solver is the NASA compressor rotor geometry 67 [89]. This geometry has become a popular test case for three dimensional viscous flow predictions because of the available detailed experimental data obtained using a laser anemometer [90]. Although the structural properties for this configuration are not available, the blade is considered to be flexible enough for flutter to occur under some flow conditions and a handful of researchers have used it to certify the validity of aeroelastic turbomachinery applications [91,92,93].

Finally, additional test cases using simplified but well understood, closed form solution models such as the flexible cylinder case used in this research is also recommended. One such configuration is the Onera M6 Wing, for which experimental wind tunnel results exist over a range of flow conditions [94].

8.2 Further development & improvements

While efforts outlined in this research were taken to enhance the resulting unsteady aeroelastic solver (specifically the reduction of simulation runtime), many opportunities exist to improve upon the model developed. Such improvements include incorporating additional turbulence models such as k-ε [95,96], k-ω [97], Spalart Allmaras [98], or even Detached Eddy Simulation (DES) [99], and capabilities such as film cooling and phase lagged boundary conditions.

However another area of possible development and improvement is greater reduction in simulation runtime through additional parallelism. This might take several forms, from simply adding more domain decomposition to adapting portions of the solver for use with General Purpose Graphics Processing Units (GPGPU) [100,101], or even a hybrid method using both of these. In fact, use of such a hybrid system may allow such an aeroelastic solver to be more easily used in the design phase of turbomachinery, by allowing it to effectively make use of the GPGPU and multi-core technology which is becoming prevalent in computer workstations.

9. REFERENCES

1. Lord, W. K., MacMartin, D. G., and Tillman, T. G., "Flow Control Opportunities in Gas Turbin Engines," *AIAA paper no. 2000-2234*, Fluids 2000 Conference and Exhibit, June 19-22, 2000, Denver, CO.

2. Sharma, O. P., Pickett, G. F., and Ni, R. H., "Assessment of Unsteady Flows in a Compressor Rotor," *ASME Journal of Turbomachinery*, Vol. 114, No. 1, January 1992, pp. 79-90.

3. Boyce, P. M., *Gas Turbine Engineering Handbook*, 3rd ed., Gulf Professional Publishing. Boston, MA, 2006.

4. Marshall, J. G., and Imregun, M. , "A Review of Aeroelasticity Methods with Emphasis on Turbomachinery Applications," *Journal of Fluids and Structures*, Vol. 10, No. 3, April 1996, pp. 237-267.

5. Petrov, E. P., Mare, L. D., Hennings, H. , and Elliott, R. , "Forced Response of Mistuned Balded Disks in Gas Flow: A Comparitive Study of Predictions and Full-Scale Experimental Results," *Journal of Engineering for Gas Turbines and Power*, Vol. 132, No. 5, May 2010, pp. 52504-52514.

6. Giacommo, P. , *Unsteady Aerodynamic Stator-Rotor Interaction in High Pressure Turbines*, Von Karman Institute for Fluid Dynamics. Rhode-Saint-Gense, Belgium, 2007.

7. Bendikson, O. O., "Aeroelastic Problems in Turbomachines ," *Flight-Vehicle Materials, Structures, and Dynamics - Asseement and Future Directions*, Vol. 5, 1993, pp. 241-297.

8. Rao, J. S., "Turbomachinery Blade Vibration," *The Shock and Vibration Digest*, Vol. 19, 1987, pp. 3-10.

9. Lim, S. H., Castanier, M. P., and Pierre, C. , "Vibration Modeling of Bladed Disks Subject to Geometric Mistuning and Design Changes," *AIAA Paper 2004-1686*, 45th AIAA/ASME/ASCE/AHS/ASC Structures, Structural Dynamics and Materials Conference, April 19-22, 2004, Palm Springs, CA.

10. Rothermel, J. , Dorney, S. M., and Dorney, D. J., "CFD-based Design of Turbopump Inlet Duct for Reduced Dynamic Loads," 14th Annual Thermal and Fluids Analysis Workshop, August 18-23, 2003, Hampton, VA.

11. Lane, F. , "System Mode Shapes in the Flutter of Compressor Blade Rows," *Journal of Aeronautical Sciences*, Vol. 23, 1956, pp. 54-66.

12. Bartels, R. E., and Sayma, A. I., "Computational Aeroelastic Modeling of Airframes and Turbomachinery: Progress and Challenges," *Philosophical Transactions of the Royal Society A*, Vol. 36, No. 1859, October 2007, pp. 2469-2499.

13. Baik, S. , Castanier, M. P., and Pierre, C. , "Mistuning Sensitivity Prediction of Bladed Disks Using Eigenvalue Curve Veerings," *Proceedings of the 9th National Turbine Engine High Cycle Fatigue Conference*, March 2004.

14. Whitehead, D. S., "Classical Two-Dimensional Methods ," *Manual on Aeroelasticity in Axial-Flow Turbomachinery: Unsteady Turbomachinery Aerodynmamics*, Vol. 1, No. 298, January 1987, pp. 1-30.

15. Gerolymos, G. A., "Numerical Integration of the 3D Unsteady Euler Equations for Flutter Analysis of Axial Flow Compressors," *ASME paper no. 88-GT-255*, 1988.

16. Wolff, J. M., and Fleeter, S. , "Euler Analysis of Oscillating Cascade Unsteady Aerodynamics Using Embedded Composite Grids," *AIAA paper no. 94-0077*, 1994.

17. Ji, S. , and Liu, F. , "Computation of Unsteady Flows Around Oscillating Blades and Aeroelasticity Behavior," *AIAA paper no. 97-0161*, 35th AIAA Aerospace Sciences Meeting and Exhibit, January 6-9, 1997, Reno, NV.

18. Weber, S. , Gallus, H. E., and Peitsch, D. , "A Numerical Approach to Unstalled and Stalled Flutter Phenomena in Turbomachinery," *ASME paper no. 97-GT-102*, 1997.

19. Bendiksen, O. O., and Kousen, K. A., "Transonic Flutter Analysis using the Euler Equations," *AIAA paper no. 87-0911*, AIAA Dynamics Specialists Conference, April 9-10, 1987, Moterey, CA.

20. Huff, D. L., and Reddy, T. S. R., "Numerical Analysis of Supersonic Flow Through Oscillating Cascade Sections by Using a Deforming Grid," *AIAA Paper no. 89-2805*, 1989.

21. Eick, C. D., and Liu, J. S., "Comparisons of Aeroelastic Computer Code Predictions Against Measured Rotor Vibratory Response Data," *AIAA paper no. 97-2750*, 1997.

22. Gao., C. , Luo, S. , and Liu, F. , "Calculation of Airfoil Flutter by an Euler Method with Approximate Boundary Conditions," *AIAA paper no. 2003-3830*, 16th AIAA Computational Fluid Dynamics Conference, June 23-26, 2003, Orlando, FL.

23. Gottfried, D. A., and Fleeter, S. , "Prediction of Unsteady Cascade Aerodynamics by an Arbitrary Lagrangian-Eulerian Finite Element Method," *AIAA paper no. 98-0374*, 1998.

24. Bendiksen, O. O., "A New Approach to Computational Aeroelasticity," *AIAA paper no. 91-0939*, 1991.

25. Masud, A. , "A Space-Time Finite Element Formulation for Fluid-Structure Interaction," *AIAA paper no. 96-4049*, 6th AIAA Symposium on Multidisiplinary Analysis and Optimization, September 4-6, 1996, Bellevue, WA.

26. Gottfried, D. A., and Fleeter, S. , "Turbomachinery Blade Row Interaction Predictions with a Three-Dimensional Finite Element Method," *AIAA paper no. 2000-3226*, 2000.

27. Sadeghi, M. , and Liu, F. , "Investigation of Mistuned Effects on Cascade Flutter Using a Coupled Method," *AIAA paper no. 2002-0952*, 40th AIAA Aerospace Sciences Meeting and Exhibit, January 14-17, 2002, Reno, NV.

28. Meira Josete, B. C. et al., "The Suitability of Different FEA Models for Studying Root Fractures Caused by Wedge Effect," *Journal of Biomedical Materials Research*, Vol. 84, No. 2, 2008, pp. 442-446.

29. Srivastava, R. , Sankar, L. N., Reddy, T. S., and Huff, D. L., "Application of an Efficient Hybrid Scheme for Aeroelastic Analysis of Advanced Propellers," *AIAA Journal of Propulsion and Power*, Vol. 7, No. 8, September 1991, pp. 767-775.

30. Yamamoto, O. , and August, R. , "Structural and Aerodynamic Analysis of a Large-Scale Advanced Propeller Blade," *AIAA Journal of Propulsion and Power*, Vol. 8, No. 2, March 1992, pp. 367-373.

31. Sayma, A. I., Vahdati, M. , and Imregun, M. , "Forced Response Analysis of an Intermediate Pressure Turbine Blade using a Nonlinear Aeroelasticity Model," *AIAA paper no. 98-3718*, 34th Joint Propulsion Conference and Exhibit, July 13-15, 1998, Cleveland, OH.

32. Vahdati, M. , Sayma, A. , and Imregun, M. , "Prediction of High and Low Engine Order Forced Responses for a Low Pressure Turbine Blade," *AIAA paper no. 98-3719*, 34th Joint Propulsion Conference and Exhibit, July 13-15, 1998, Cleveland, OH.

33. Breard, C. , Imregun, M. , Sayma, A. , and Vahdati, M. , "Flutter Stability Analysis of a Complete Fan Assembly," *AIAA paper no. 99-0238*, 37th AIAA Aerospace Sciences Meeting and Exhibit, January 11-14, 1999, Reno, NV.

34. Servera, G. , Beaumier, P. , and Costes, M. , "A Weak Coupling Method Between the Dynamic Code HOST and the 3D Unsteady Euler Code WAVES," *Journal of Aerospace Science and Technologies*, Vol. 5, No. 6, September 2001, pp. 397-408.

35. Carstens, V. , Kemme, R. , and Schmitt, S. , "Coupled Simulation of Flow-Structure Interaction in Turbomachinery," *Journal of Aerospace Science and Technology*, Vol. 7, No. 4, June 2003, pp. 298-306.

36. Johnston, D. A., Cross, C. J., and Wolff, J. M., "An Architecture for Fluid/Structure Interaction Analysis of Turbomachinery Blading," *AIAA paper no. 2005-4013*, 41st Joint Propulsion Conference and Exhibit, July 10-13, 2005, Tuscon, AZ.

37. Buyya, R. , *High Performance Cluster Computing: Volume 2, Programming and Applications*, Prentice Hall PTR. Upper Sandle River, NJ, 1999.

38. Sorenson, R. L., "A Computer Progam to Generate Two-Dimensional Grids about Airfoils and Other Shapes by use of Poisson's Equations," *NASA TM-81198*, May 1980.

39. Sondak, D. L., and Dorney, D. J., "General Equation Set Solver for Compressible and Incompressible Turbomachinery Flows," *AIAA paper no. 2003-4420*, 39th Joint Propulsion Conference and Exhibit, July 20-23, 2003, Huntsville, AL.

40. Pulliam, T. H., and Steger, J. L., "Implicit Finite-Difference Simulation of Three-Dimensional Compressible Flow," *AIAA Journal*, Vol. 18, No. 2, February 1980, pp. 159-167.

41. Rai, M. M., "Three-Dimensional Navier-Stokes Simulations of Turbine Rotor-Stator Interaction: Part I - Methodology," *AIAA Journal of Propulsion and Power*, Vol. 5, No. 3, May-June 1989, pp. 305-311.

42. Visbal, M. , and Gaitonde, D. , "High-Order Accurate Methods for Complex Unsteady Subsonic Flows," *AIAA Journal*, Vol. 37, No. 10, October 1999, pp. 1222-1230.

43. Visbal, M. , and Gaitonde, D. , "Very High Order Spatially Implicit Schemes for Computational Acoustics on Curvilinear Meshes," *Journal of Computational Acoustics*, Vol. 9, No. 4, December 2001, pp. 1259-1286.

44. Thomas, P. D., and Lombard, C. K., "Geometric Conservation Law and its Application to Flow Computations on Moving Grids," *AIAA Journal*, Vol. 17, No. 10, October 1979, pp. 1030-1037.

45. Gaitonde, D. , and Visbal, M. , "Further Development of a Navier-Stokes Solution Procedure based on Higher Order Formulas," *AIAA Paper 99-0557*, 1999.

46. Visbal, M. , and Gordnier, R. , "A High Order Flow Solver for Deforming and Moving Meshes," *AIAA Paper 2000-2619*, June 2000.

47. Vinokur, M. , "An Analysis of Finite Difference and Finite Volume Formulations of Conservation Laws," *Journal of Computational Physics*, Vol. 81, No. 1, March 1989, pp. 1-52.

48. Obayashi, S. , "Free-Stream Capturing in Fluid Conservation Law for Moving Coordinates in Three Dimensions," *NASA-CR-177572*, January 1991.

49. Grandy, J. , "Efficient Computation of Volume of Hexahedral Cells," *Lawrence Livermore National Laboratory UCRL-ID-128886*, October 1997.

50. Visbal, M. , and Gaitonde, D. , "On the Use of Higher Order Finite Difference Schemes on Curvilinear and Deforming Meshes," *Journal of Computational Physics*, Vol. 181, No. 1, September 2002, pp. 155-185.

51. White, F. M., *Viscous Fluid Flow*, 2nd ed., McGraw-Hill. New York, NY, 1991.

52. Hoffmann, K. A., and Chiang, S. T., *Computational Fluid Dynamics*, Engineering Education System. Wichita, KS, 1998.

53. Baldwin, B. S., and Lomax, H. , "Thin Layer Approximation and Algebraic Model for Seperated Turbulent Flow," *AIAA paper no. 78-0257*, 1978.

54. Ganville, P. S., "A Modified Van Driest Formula for the Mixing Length of Turbulent Boundary Layers in Pressure Gradients," *ASME Journal of Fluids Engineering*, Vol. 111, No. 1, March 1989, pp. 94-97.

55. Granville, P. S., "Baldwin-Lomax Factors for Turbulent Boundary Layers in Pressure Gradiants," *AIAA Journal*, Vol. 25, No. 12, December 1987, pp. 1624-1627.

56. Dorney, D. J., Horia, C. F., Ashpis, D. E., and Solomon, W. J., "Effects of Blade Count on Boundary Layer Development in a Low Pressure Turbine," *AIAA paper no. 2000-0742*, 38th Aerospace Sciences Meeting and Exhibit, January 10-13, 2000, Reno, NV.

57. Spalding, D. B., "A Single Formulae for the Law of the Wall," *Journal of Applied Mechanics*, Vol. 28, September 1961, pp. 455-457.

58. Boyle, R. J., and Senyitko, R. G., "Measurements and Predictions of Surface Roughness Effects on Turbine Vane Aerodynamics," *ASME paper no. GT-2003-38580*, ASME Turbo Expo, June 16-19, 2003, Atlanta, GA.

59. Bammert, K. , and Milsch, R. , "Boundary Layers on Rough Compressor Blades," *ASME paper no. 72-GT-48*, 1972.

60. Shabbir, A. , and Turner, M. G., "A Wall Function for Calculating the Skin Friction with Surface Roughness," *ASME paper no. GT-2004-53908*, ASME Turbo Expo, June 14-17, 2004, Vienna, Austria.

61. Schlicting, H. , *Boundary Layer Theory*, 7th ed., McGraw-Hill. New York, NY, 1979.

62. Mani, M. , and Ota, D. , "A Compressible Wall Function for Steady and Unsteady Flow Applications," *AIAA paper no. 99-3216*, 1999.

63. Shih, T. H., Povinelli, L. A., and Liu, N. S., "Application of Generalized Wall Function for Complex Turbulent Flows," *Journal of Turbulence*, Vol. 4, April 2003, pp. 15-15.

64. Bolcs, A. , and Fransson, T. H., "Aeroelasticity in Turbomachines Comparision of Theoretical and Experimental Cascade Results," *Communication de Laboratoire de Thermique Appliquee et de Turbomachines*, No. 13, 1986, Ecole Polytechnique Federale de Lausanne, Switzerland.

65. *TORQUE Admin Manual Version 2.1.6*, Adaptive Computing Enterprises, Inc., 2006.

66. Hwang, K. , and Xu, Z. , *Scalable Parallel Computing: Technology, Architecture, Programming*, McGraw-Hill. Boston, MA, 1998.

67. Winkelmann, R. , Hauser, J. , and Williams, R. D., "Strategies for Parallel and Numerical Scalability of CFD Codes," *Journal of Computer Methods in Applied Mechanics and Engineering*, Vol. 174, No. 3-4, May 1999, pp. 433-456.

68. Saghi, G. , Siegel, H. J., and Gray, G. L., "Predicting Performance and Selecting Modes of Parallelism: A Case Study Using Cyclic Reduction on Three Parallel Machines," *Journal of Parallel and Distributed Computing*, Vol. 19, No. 3, November 1993, pp. 219-233.

69. Lin, H. X., "A Unifying Graph Model for Designing Parallel Algorithms for Tridiagonal Systems," *Journal of Parallel Computing*, Vol. 27, No. 7, June 2001, pp. 925-939.

70. Rathe, U. W., Sanders, P. , and Knight, P. L., "A Case Study in Scalability: An ADI Method for the Two Dimensional Time Dependent Dirac Equation," *Journal of Parallel Computing*, Vol. 25, No. 5, May 1999, pp. 525-533.

71. Yaldin, Y. , and Caughey, D. A., "Parallel Computing Strategies for Block Multigrid Implicit Solution of the Euler equations," *AIAA Journal*, Vol. 30, No. 8, August 1992, pp. 2032-2038.

72. Paaterson, D. , "Computer Architecture is Back: Parallel Computing Lanscape," Stanford University Computer System Colloquium, Stanford University, January 31, 2007.

73. Kumar, V. , Grama, A. , Gupta, A. , and Karypis, G. , *Introduction to Parallel Computing Design and Analysis of Algorithms*, Benjamin/Cummings. Reddwood City, CA, 1994.

74. Geuzaine, Christophe , and Remacle, Jean-François , "Gmsh: A 3-D finite element mesh generator with built-in pre- and post-processing facilities," *International Journal for Numerical Methods in Engineering*, Vol. 79, No. 11, September 2009, pp. 1309–1331.

75. C., Farhat , Lesoinne, M. , and LeTallec, P. , "Load and Motion Transfer Algorithms for Fluid/Structure Interaction Problems with Non-matching Interfaces: Momentum and Energy Conservation, Optimal Discretization and Application to Aeroelasticity," *Journal of Computational Methods in Applied Mechanics and Engineering*, Vol. 157, 1998, pp. 95-114.

76. Bonet, Javier , and Peraire, Jamie , "An Alternating Digital Tree (ADT) Algorithm for 3D Geometric Searching and Intersection Problems," *International Journal of Numerical Methods in Engineering*, Vol. 31, 1991, pp. 1-7.

77. Bathe, Klaus-Jurgen , *Finite Element Procedures*, Prentice Hall. Upper Sadle River, NJ, 1996.

78. Morton, Scott A., Melville, Reid B., and Visbal, Miguel R., "Accuracy and Coupling Issues of Aeroelastic Bavier-Stokes Solutions on Deforming Meshes," *Journal of Aircraft*, Vol. 35, No. 5, 1998, pp. 798-805.

79. Lesoinne, M , and Farhat, C. , "Geometric Conservation Law for Flow Problems with Moving Boundaries and Deforming Meshes, and Their Impact on Aeroelastic Computations," *Journal of Computational Methods in Applied Mechanics and Engineering*, Vol. 134, 1996, pp. 71-90.

80. Koobus, B. , and Farhat, C. , "Second-Order Time-Accurate and Geometric Conservative Implicit Schemes for Flow Computations on Unstructured Dynamic Meshes," *Journal of Computational Methods in Applied Mechanics and Engineering*, Vol. 170, 1999, pp. 103-129.

81. Chen, J. P., and Briley, W. R., "A Parallel Flow Solver for Unsteady Multiple Blade Row Turbomachinery Simulations," *ASME paper no. 2001-GT-0348*, ASME TURBO EXPO 2001, June 4-7, 2001, New Orleans, LA.

82. Serway, Raymond A., *Physics for Scientist & Engineers*, 3rd ed., Saunders College Publishing. Philadelphia, PA, 1992.

83. Silkowski, P. D., Rhie, C. M., Copeland, G. S., Eley, J. A., and Bleeg, J. M., "Computational Fluid Dynamics Investigation of Aeromechanics," *AIAA Journal of Propulsion and Power*, Vol. 18, No. 4, July-August 2002, pp. 788-796.

84. Sanders, A. J., "Nonsynchronous Vibration (NSV) due to Flow Induced Aerodynamic Instability in a Composite Fan Rotor," *ASME Journal of Turbomachinery*, Vol. 127, No. 2, April 2005, pp. 412-421.

85. Fox, Robert W., and McDonald, Alan T., *Introduction to Fluid Mechanics*, 4th ed., John Wiley & Sons Inc. New York, NY, 1992.

86. Ponta, F. L., and Aref, H. , "Numerical Experiments on Vortex Shedding from an Oscillating Cylinder," *Journal of Fluids and Structures*, Vol. 22, No. 3, April 2006, pp. 327-344.

87. Inman, Daniel J., *Engineering Vibration*, Prentice Hall. Upper Sadle River, NJ, 1996.

88. Avallone, Eugene A., and Baumeister III, Theodore , *Mark's Standard Handbook for Mechanical Engineers*, 9th ed., McGraw-Hill. New York, NY, 1987.

89. Urasek, D. C., Gorrell, W. T., and S., Cunnan W., "Performance of Two Stage Fan Having Low-Aspect-Ratio, First-Stage Rotor Blading," *NACA Technical Report no. NACA-TP-1493*, August 1979.

90. Strazisar, A. J., Wood, J. R., Hathaway, M. D., and Suder, K. L., "Laser Anemometer Measurements in a Transonic Axial-Flow Fan Rotor," *NASA Technical Report no. NACA-TP-2879*, 1989.

91. Chuang, H. A., and Verdon, J. M., "A Numerical Simulator for Three-Dimensional Flows Through Vibrating Blade Rows," *NASA Technical Report no. NASA-CR-1998-208511*, 1998.

92. He, L. , and Denton, J. D., "Three-Dimensional Time-Marching Inviscid and Viscous Solutions for Unsteady Flows Around Vibrating Blades," *Journal of Turbomachinery*, Vol. 116, No. 3, July 1994, pp. 469–476.

93. Vahdati, M. , and Imregun, M. , *Nonlinear Aeroelasticity Analysis Using Unstructured Dynamics Meshes*, Kluwer Academic Publishers, Torsten H. Fransson, Ed. Norwell, MA, 1995.

94. Schmitt, V. , and Charpin, F. , "Pressure Distributions on the ONERA-M6-Wing at Transonic Mach Numbers," *Experimental Data Base for Computer Program Assessment*, Report of the Fluid Dynamics Panel Working Group 04, AGARD AR 138, May, 1979.

95. Jones, W. P., and Launder, B. E., "The Prediction of Laminarization with a Two-Equation Model of Turbulence," *International Journal of Heat and Mass Transfer*, Vol. 15, 1972, pp. 301-314.

96. Launder, B. E., and Sharma, B. I., "Application of the Energy Dissipation Model of Turbulence to the Calculation of Flow Near a Spinning Disc," *Letters in Heat and Mass Transfer*, Vol. 1, No. 2, November-December 1974, pp. 131-138.

97. Menter, F. R., "Two-Equation Eddy-Viscosity Turbulence Models for Engineering Applications," *AIAA Journal*, Vol. 32, No. 8, August 1994, pp. 1598-1605.

98. Spalart, P. R., and Allmaras, S. R., "A One-Equation Turbulence Model for Aerodynamic Flows," *AIAA Paper no. 92-0439*, AIAA 30th Aerospace Sciences Meeting and Exhibit,January 6-9, 1992, Reno, NV.

99. Spalart, P. R., "Comments on the Feasibility of LES for Wing and on a Hybrid RANS/LES Approach," *1st ASOSR CONERFENCE on DNS/LES*, Arlington, TX, August, 1997.

100. Jespersen, Dennis C., "Acceleration of a CFD Code with a GPU," *NAS Technical Report NAS-09-003*, November 2009.

101. Cohen, Jonathan M., and Molemaker, M. Jeroen, "A Fast Double Precision CFD Code using CUDA," *21st International Conference on Parallel Computational Fluid Dynamics*, May 18-22, 2009, Moffett Field, CA.

Appendix A. Block Tridiagonal Systems

When a system of PDEs is approximated by an implicit formulation involving three grid points at each level, a block-tridiagonal system is produced. The resulting block-tridiagonal system may be expressed in a general form as:

$$S\Delta Q = R \tag{A-1}$$

where *ΔQ* and *R* are *m* component vectors. The coefficient *S* represents the block tridiagonal coefficient expressed by:

$$S = \begin{bmatrix} B_2 & C_2 & & & \\ A_3 & B_3 & C_3 & & \\ & \ddots & \ddots & \ddots & \\ & & A_{IM-2} & B_{IM-2} & C_{IM-2} \\ & & & A_{IM-1} & B_{IM-1} \end{bmatrix} \tag{A-2}$$

Where A_i, B_i, C_i are square matrices of order *m.*

To solve this system, an LU factorization is first applied to the *S* coefficient matrix:

$$S = LU = \begin{bmatrix} \alpha_2 & & & & \\ A_3 & \alpha_3 & & & \\ & \ddots & \ddots & & \\ & & A_{IM-2} & \alpha_{IM-2} & \\ & & & A_{IM-1} & \alpha_{IM-1} \end{bmatrix} \begin{bmatrix} I & \beta_2 & & & \\ & I & \beta_3 & & \\ & & \ddots & \ddots & \\ & & & I & \beta_{IM-2} \\ & & & & I \end{bmatrix} \tag{A-3}$$

where *I* is the identity matrix of order *m.* The square matrices α_i and β_i are determined as:

$$\alpha_2 = \beta_2 \quad \text{and} \quad \beta_2 = B_2^{-1}C_2 \tag{A-4}$$

$$\alpha_i = B_i - A_i\beta_{i-1} \quad \text{for } i = 3, 4, \ldots, \text{IM-1} \tag{A-5}$$

$$\beta_i = \alpha_i^{-1}C_i \quad \text{for } i = 3, 4, \ldots, \text{IM-2} \tag{A-6}$$

The system given in Equation A-1is now equivalent to

$$LY = R \tag{A-7}$$

where

$$Y = U\Delta Q \tag{A-8}$$

Rewritting Equation A-6:

$$\begin{bmatrix} \alpha_2 & & & & \\ A_3 & \alpha_3 & & & \\ & \ddots & \ddots & & \\ & & A_{IM-2} & \alpha_{IM-2} & \\ & & & A_{IM-1} & \alpha_{IM-1} \end{bmatrix} \begin{bmatrix} Y_2 \\ Y_3 \\ \vdots \\ Y_{IM-2} \\ Y_{IM-1} \end{bmatrix} = \begin{bmatrix} R_2 \\ R_3 \\ \vdots \\ R_{IM-2} \\ R_{IM-1} \end{bmatrix} \tag{A-9}$$

from which:

$$Y_2 = \alpha_2^{-1}R_2 \tag{A-10}$$

and

$$Y_i = \alpha_i^{-1}\left(R_i - A_iY_{i-1}\right) \quad \text{for } i = 3, 4, \ldots, \text{IM-1} \tag{A-11}$$

Next, Equation A-8 is expressed as:

$$\begin{bmatrix} I & \beta_2 & & & \\ & I & \beta_3 & & \\ & & \ddots & \ddots & \\ & & & I & \beta_{IM-2} \\ & & & & I \end{bmatrix} \begin{bmatrix} \Delta Q_2 \\ \Delta Q_3 \\ \vdots \\ \Delta Q_{IM-2} \\ \Delta Q_{IM-1} \end{bmatrix} = \begin{bmatrix} Y_2 \\ Y_3 \\ \vdots \\ Y_{IM-2} \\ Y_{IM-1} \end{bmatrix} \tag{A-12}$$

from which

$$\Delta Q_{IM-1} = Y_{IM-1} \tag{A-13}$$

and

$$\Delta Q_i = Y_i - \beta_i\Delta Q_{i+1} \quad \text{for } i = \text{IM-1, IM-2}, \ldots, 3, 2 \tag{A-14}$$

Appendix B. Quick Search using Shape Functions

Shape functions are simple weighting values which are used commonly in Finite Element Analysis for linear interpolation of values between nodes. In Corsair they are used to obtain a tri-linear interpolation of flow variables between overlaid grids. However to accomplish this, the three points from the donating grid which contain the recipient grid point must first be determined. In the distributed version of Corsair, this is done with an exhaustive search, but a much faster method was devised which makes use of a seldom used properties of shape functions.

Take the 1D linear element (or line segment) of length L, with two nodes as illustrated in Figure B-1:

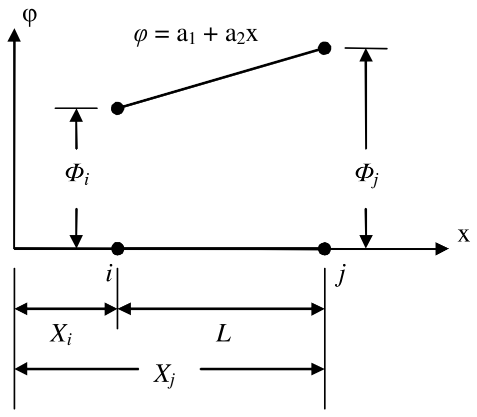

Figure B-1. One dimensional linear element

In figure B-1, the nodes are denoted by *i* and *j* while their associated nodal values are denoted by Φ_i and Φ_j. The origin of the coordinate system is to the left of node *i* and the value φ varies linear between the two nodes per the following relationship:

$$\varphi = a_1 + a_2 x \tag{B-1}$$

where the coefficients a_1 and a_2 can be determined using the nodal conditions:

$$\begin{aligned} \varphi &= \Phi_i \quad \text{at } \mathrm{x} = X_i \\ \varphi &= \Phi_j \quad \text{at } \mathrm{x} = X_j \end{aligned} \tag{B-2}$$

to develop the pair of equations:

$$\begin{aligned} \Phi_i &= a_1 + a_2 X_i \\ \Phi_j &= a_1 + a_2 X_j \end{aligned} \tag{B-3}$$

which yields a_1 and a_2 as:

$$\begin{aligned} a_1 &= \frac{\Phi_i X_j - \Phi_j X_i}{X_j - X_i} \\ a_2 &= \frac{\Phi_j - \Phi_i}{X_j - X_i} \end{aligned} \tag{B-4}$$

Substitution of Equation B-4 into Equation B-1 and rearranging gives:

$$\varphi = \left(\frac{X_j - x}{L}\right)\Phi_i + \left(\frac{x - X_i}{L}\right)\Phi_j \tag{B-5}$$

where X_j-X_i has been replaced by the element length *L*. Equation B-5 is in standard finite element form, where the nodal values are multiplied by linear functions of *x* called shape functions. Shape functions are commonly denoted by *N* with a subscript indicating the node with which it is associated with. The shape functions in Equation B-5 are:

$$N_i = \frac{X_j - x}{L} \quad \text{and} \quad N_j = \frac{x - X_i}{L} \tag{B-6}$$

which allows Equation B-5 to be rewritten as:

$$\varphi = N_i \Phi_i + N_j \Phi_j \tag{B-7}$$

Now for a few observations about shape functions from this simple example. First, the sum of the shape functions is always one. Second each shape function has a value of one at its own node and zero at the other node. Thus if the value of *x* falls between the nodes, then the value of the shape functions will be between zero and one. If however, the value of *x* falls to the left of node *i*, then N_i will be greater than one and N_j will be negative. If the value of *x* is to the right of node *j*, then N_i will be negative and N_j will be greater than one. Therefore, if the point to be interpolated at falls outside the range defined by the nodes, the shape functions when evaluated at the nodes indicates which direction the point to be interpolated at lies.

These properties exist for all shape functions, including the ones used for the tri-linear interpolation in Corsair. The property of indicating the direction for which an interpolating point lies outside the interpolating range was used to replace the exhaustive search of donating grid points containing the recipient grid point between overlaid grids for all but the first recipient grid point with a quick or smart search algorithm in Corsair. To illustrate the logic of this algorithm, take Figure B-2 which represents a portion of the overlaid grid region. For this example, the H-grid (nodes with by *i* and *j* notation) is the donating grid and the outer boundary of the O-grid (dashed line) contains the recipient points (denoted by *A* though *F*). To begin the algorithm, the four points from the H grid forming a box which contains point *A* must first be found using an exhaustive search via a do loop through indexes i and j. For each i and j, the shape functions for the two triangles in the box formed by points (i, j), (i+1, j), (i, j+1), (i+1, j+1) are evaluated for the recipient point *A*. If all three shape function for either of the two triangles are between zero and one, then the triangle of donating points has been found, if not, the exhaustive search continues. Once the triangle of donating points has been found, the quick search algorithm can take over. First the shape functions for the two triangles in the box containing the previous recipient point are evaluated using the coordinates of next recipient point. The results of calculating N_2 through N_5 can then be used to determine if this next recipient point lies in the current box of donating points or if it doesn't, which direction to move in to find the correct box of donating points. Applying the properties of shape functions just discussed to shape function N_3 in Figure B-2, the value will be negative if the point being interpolated for falls beyond the line formed by j+1. This simple principle is used in the quick search algorithm to determine which direction to move the search box in. So if N_2 is negative the search box is moved left, if N_3 is negative the search box is moved up, if N_4 is negative the search box is moved right, and if N_5 is negative the search box is moved down.

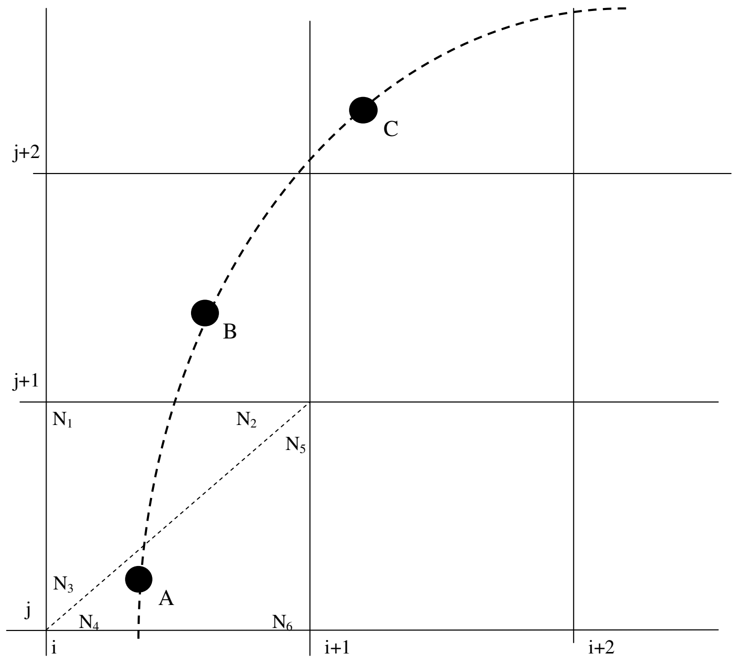

Figure B-2. Portion of overlaid O- and H-grid

For the example here, the shape functions for the upper and lower triangles of the box formed by points (i, j), (i+1, j), (i, j+1), (i+1, j+1) would be evaluated using the coordinates of point *B*. When these shape functions are evaluated, N_2 and N_4 will be between zero and one, N_5 will be greater than one, and N_3 will be negative. Thus, the search box would be moved up and the shape functions for the two triangles in the box formed by points (i, j+1), (i+1, j+1), (i, j+2), (i+1, j+2) would be evaluated.

In addition, combinations of these moves can be made in a single step, for example if N_3 and N_4 are both negative, then the box is moved diagonally up and to the right. During practice, the algorithm normally finds the correct box within 3 moves, even with very fine grids, and is much faster than the exhaustive search. When performing the search on successive radial slices (k index), the i and j box indexes for the associated point one slice previous are used as a started point for the search. Likewise, when the grids are moving relative to one another, the box indexes from the previous time step are used as an initial starting point.